



저작자표시-비영리-변경금지 2.0 대한민국

이용자는 아래의 조건을 따르는 경우에 한하여 자유롭게

- 이 저작물을 복제, 배포, 전송, 전시, 공연 및 방송할 수 있습니다.

다음과 같은 조건을 따라야 합니다:



저작자표시. 귀하는 원저작자를 표시하여야 합니다.



비영리. 귀하는 이 저작물을 영리 목적으로 이용할 수 없습니다.



변경금지. 귀하는 이 저작물을 개작, 변형 또는 가공할 수 없습니다.

- 귀하는, 이 저작물의 재이용이나 배포의 경우, 이 저작물에 적용된 이용허락조건을 명확하게 나타내어야 합니다.
- 저작권자로부터 별도의 허가를 받으면 이러한 조건들은 적용되지 않습니다.

저작권법에 따른 이용자의 권리는 위의 내용에 의하여 영향을 받지 않습니다.

이것은 [이용허락규약\(Legal Code\)](#)을 이해하기 쉽게 요약한 것입니다.

[Disclaimer](#)

이학박사 학위논문

황화아연 일차원 나노구조의 제조 및 응용

Fabrication and Applications of One-Dimensional
Zinc Sulfide Nanostructures

2015 년 8 월

서울대학교 대학원
화학부 물리화학 전공
김 연 호

A Ph. D. Dissertation

Fabrication and Applications of One-Dimensional
Zinc Sulfide Nanostructures

By Yeonho Kim

Supervisor: Professor Du-Jeon Jang

Major: Physical Chemistry

Department of Chemistry

Graduate School of Seoul National University

August 2015

Abstract of Dissertation

A facile wet-chemical hydrothermal synthetic method has been applied to fabricate single-crystalline ZnS nanobelts showing the intense and narrow ultraviolet luminescence at room temperature. The ternary mixed solvents of hydrazine, ethylenediamine, and water plays an important role to synthesize wurtzite ZnS nanobelts via one-step hydrothermal process. As-prepared ZnS nanobelts have also been found to chemically pure, structurally uniform, single-crystalline, and defect-free. These features bring about a highly narrow band-edge luminescence at room temperature. The one-dimensional ZnS nanobelts have also been applied to the visible-blindness ultraviolet photodetector and highly efficient photocatalysts with hybridization of the graphene.

Chapter 1 gives a brief overview of nanosized materials especially on II-VI semiconductors. Materials in the nanoscale range show markedly different both the chemical and physical properties from those observed in micro and bulk matter. The optical properties and crystallographic structures of one-dimensional ZnS as well as their synthetic methods of chemically and physically, have been explained.

In Chapter 2, the distinct properties of ZnS-ethylenediamine inorganic-organic hybrid nanobelts are discussed. A template-free and one-pot solvothermal process has been applied to synthesis of hybrid nanobelts and their aspect ratios have been controlled by adjusting solvent volume ratios of

hydrazine monohydrate to ethylenediamine. The observed data from the room-temperature photoluminescence spectra of hybrid nanobelts distinct three bands, which are assigned to band-edge emission, trap sites-related emission, and anion-vacancy emission, respectively.

Chapter 3 presents one-step hydrothermal synthesis of one-dimensional ZnS nanobelts having a narrow band-edge emission at room temperature. The preparation of this synthetic method has been reported for the first time. The obtained photoluminescence spectrum has been fitted well with multiple Lorentzian profiles, which was interpreted by comparison to previous theoretical studies. A growth mechanism of wurtzite ZnS nanostructures are also given. Diverse methods such as transmission electron microscopy, X-ray diffraction, thermal gravimetric analysis, X-ray photoelectron spectroscopy, and Fourier-transform infrared spectroscopy have been employed to understand the facile growth mechanism of wurtzite ZnS nanobelts showing intense ultraviolet luminescence. Wurtzite ZnS nanobelts have been found to form as ethylenediamine molecules escape via hydration from the lamellar structures of ZnS-ethylenediamine nanobelts, which are a reaction intermediate produced at the early stage of the reaction. The chemical composition, the morphology, and the optical properties of the produced ZnS nanobelts have been controlled well by systematically varying time, temperature, and solvents.

In Chapter 4, applications of graphene-ZnS nanobelts hybrid nanostructures are discussed. High-performance ultraviolet photodetectors

have been fabricated based on the hybrid structure of solution-grown ZnS nanobelts and chemical vapor deposition-grown graphene. The increment of the effective-junction region between graphene and photoactive ZnS nanobelts by the sandwiched structure has been attributed to bring about a considerable enhanced photocurrent under light illumination to photodevices. The photoexcited electrons in the conduction band of ZnS spontaneously undergo a charge-transfer process to graphene channels, which is the ultraviolet-selective photo-detection mechanism of highly efficient photodetectors. Graphene quantum dots-embedded ZnS nanobelts have been synthesized via a facile hydrothermal method, application for the photocatalysis, especially in degradation of rhodamine B using similar sun light. As-prepared graphene-ZnS nanocomposites have been presented a significantly enhanced photocatalytic activity with recording apparent rate constant of $4.6 \times 10^{-2} \text{ min}^{-1}$ which is 14 and 1.9 times higher than that of the commercially available ZnS powder and pristine ZnS nanobelts, respectively. The enhanced performance of graphene-ZnS nanocomposites in comparison with individual constituents suggest the effective separation of photoinduced electron-hole pairs and narrowing the band gaps of nanocomposites.

Keywords: Semiconductors, Transistors, Photodetectots, Photocatalysts, Hybrid nanostructures

Student Number: 2010-20267

Table of Contents

Abstract of Dissertation	i
List of Figures and Tables	1
Chapter 1. General Introduction	8
1. 1. Nanosized and Nanostructured Materials	9
1. 1. 1. Quantum-Confinement Effects	10
1. 1. 2. Surface Effects	13
1. 1. 3. Applications of Nanosized Materials	15
1. 2. One-Dimensional Semiconductor Nanostructures	17
1. 3. ZnS Nanostructures	19
1. 3. 1. Crystallographic Structures of ZnS	19
1. 3. 2. Optical Properties of ZnS Nanostructures	21
1. 3. 3. Synthesis of One-Dimensional ZnS Nanostructures	26
1. 4. References	28
Chapter 2. One-Pot and Template-Free Fabrication of ZnS·(ethylenediamine)_{0.5} Hybrid Nanobelts	31
2. 1. Abstract	32
2. 2. Introduction	33
2. 3. Experimental Details	36
2. 4. Results and Discussion	38
2. 5. Conclusion	53
2. 6. Acknowledgements	54
2. 7. References	54

Chapter 3. Fabrication and Growth Mechanism of Single-Crystalline ZnS Nanobelts	58
Part 3A. Facile One-Step Hydrothermal Fabrication of Single-Crystalline ZnS Nanobelts with Narrow Band-Edge Luminescence	59
3A. 1. Abstract	59
3A. 2. Introduction	60
3A. 3. Experimental Details	62
3A. 4. Results and Discussion	63
3A. 5. Conclusion	73
3A. 6. Acknowledgements	73
3A. 7. References	73
Part 3B. Facile-Growth Mechanism of Wurtzite ZnS Nanostructures Showing Intense Ultraviolet Luminescence	76
3B. 1. Abstract	76
3B. 2. Introduction	77
3B. 3. Experimental Details	80
3B. 4. Results and Discussion	82
3B. 5. Conclusion	95
3B. 6. Acknowledgements	96
3B. 7. References	96
Chapter 4. Applications of Graphene/ZnS Nanobelts Hybrid Nanostructures	100
Part 4A. High-Performance Ultraviolet Photodetectors Based on Solution-Grown ZnS Nanobelts Sandwiched Between Graphene Layers	101

4A. 1. Abstract	101
4A. 2. Introduction	102
4A. 3. Experimental Details	104
4A. 4. Results and Discussion	106
4A. 5. Conclusion	118
4A. 6. Acknowledgements	119
4A. 7. References	119
Part 4B. Graphene Quantum Dots-Embedded ZnS Nanobelts with Highly Efficient Photocatalytic Performances	123
4B. 1. Abstract	123
4B. 2. Introduction	124
4B. 3. Experimental Details	126
4B. 4. Results and Discussion	128
4B. 5. Conclusion	138
4B. 6. Acknowledgements	138
4B. 7. References	139
Appendices	142
A. 1. List of Publications	142
A. 2. List of Presentations	143
A. 2. 1. International Presentations	143
A. 2. 2. Domestic Presentations	143
Abstract (Korean)	147

List of Figures and Tables

Figure 1-1. Schematic illustration of the density of states going from bulk (left) to nanocrystal (middle) to an isolated atom (right) for semiconducting (a) and metallic materials (b).

Figure 1-2. Schematic representation of the density of states of semiconductor structures depending on dimensionality.

Figure 1-3. Absorption (a) and photoluminescence (b) spectra for PbS nanocrystals with different sizes, obtained by changing the Pb/S molar ratio: 1) 1:0.3, 2) 1:0.4, 3) 1:0.5, 4) 1:0.7.

Figure 1-4. Evolution of the dispersion F as a function of n for cubic clusters up to $n = 100$ ($N = 10^6$). The structure of the first four clusters is displayed.

Figure 1-5. Example images (a) and switching behaviors of a stretchable device with three photodetectors connected in series (b). Cycling stability of the photodetectors at: 0% strain (c) and 80% strain (d) up to 50 cycles. Scotch tape testing of the photodetector array (e) and corresponding response curves before and after testing at 0% strain (f).

Figure 1-6. Band structure alignments of the CdS-ZnS core-shell structure and schematic of the photoexcited charge carrier distribution and related photocatalytic reactions.

Figure 1-7. The zinc blend (a) and wurtzite (b) crystal structures of ZnS.

Figure 1-8. Room-temperature PL spectra of ZnS nanowires via thermal evaporation method (a) and ZnS nanowires via solvothermal method (b).

Figure 1-9. CL spectra recorded at room temperature from (a) multiangular branched ZnS nanostructures (a) and single-crystalline ZnS nanobelts (b).

Figure 1-10. PL spectrum of ZnS nanobelts suspended in ethanol, taken at room temperature with excitation at 266 nm. Green curves, whose peak positions are indicated inside in the units of nanometers, are Lorentzian line shape analyses deconvoluted from the red experimental spectrum.

Figure 1-11. Schematic diagram of the thermal evaporation system used to synthesize the ZnS 1D nanostructures and a plot of temperature versus substrate temperature showing four different substrate temperature zones: zone 2 (~900 °C), zone 3 (~800 °C), zone 4 (~700 °C) and zone 5 (~600 °C).

Figure 1-12. Photograph of Teflon-lined stainless steel autoclaves with different volumes.

Figure 2-1. SEM (left) and TEM (right) images of ZnS·(en)_{0.5} nanostructures grown at 180 °C for 6 h with $V_{\text{hm}}/V_{\text{en}}$ of 3 (a), 1 (b), and 0.5 (c).

Figure 2-2. HRTEM images of ZnS·(en)_{0.5} nanostructures grown at 180 °C for 6 h with $V_{\text{hm}}/V_{\text{en}}$ of 3 (a), 1 (b), and 0.5 (c) show lattice plane distances in nm. The insets show FFT patterns obtained from the corresponding nanostructures.

Figure 2-3. HRXRD patterns of ZnS·(en)_{0.5} nanostructures grown at 180 °C with $V_{\text{hm}}/V_{\text{en}}$ of 3 during various reaction periods indicated inside (a), and for 6 h with various ratios of $V_{\text{hm}}/V_{\text{en}}$ indicated inside (b).

Figure 2-4. Raman spectra of ZnS·(en)_{0.5} nanostructures grown at 180 °C for 6 h with $V_{\text{hm}}/V_{\text{en}}$ of 3 (blue), 1 (green), and 0.5 (red).

Figure 2-5. Complete survey (a), Zn 2p (b), S 2p (c), and N 1s (d) XPS spectra of ZnS·(en)_{0.5} nanobelts grown at 180 °C for 6 h with $V_{\text{hm}}/V_{\text{en}}$ of 3.

Figure 2-6. Extinction spectrum of ZnS·(en)_{0.5} nanobelts grown at 180 °C for 6 h with $V_{\text{hm}}/V_{\text{en}}$ of 3. Nanobelts were suspended in water.

Figure 2-7. Photoluminescence spectra of ZnS·(en)_{0.5} nanostructures grown at 180 °C for 6 h with $V_{\text{hm}}/V_{\text{en}}$ of 3 (solid), 1 (dashed), and 0.5 (dotted). The nanostructures were suspended in water and excited with 266 nm laser pulses of 6 ns.

Figure 2-8. Gaussian functions (red) deconvoluted from the photoluminescence spectra (black) of ZnS·(en)_{0.5} nanostructures grown at 180 °C for 6 h with $V_{\text{hm}}/V_{\text{en}}$ of 1 (top) and 0.5 (bottom).

Figure 2-9. Maximum-normalized photoluminescence decay kinetic profiles of ZnS·(en)_{0.5} nanostructures grown at 180 °C for 6 h with $V_{\text{hm}}/V_{\text{en}}$ of 3 (squares), 1 (triangles), and 0.5 (circles) suspended in water. Photoluminescence was monitored at 450 nm after excitation with 266 nm pulses of 25 ps. Solid lines are the best-fitted curves to extract lifetimes given in Table 1.

Figure 2-10. Maximum-normalized photoluminescence spectra of ZnS·(en)_{0.5} nanobelts grown at 180 °C for 6 h with $V_{\text{hm}}/V_{\text{en}}$ of 3 (solid) and bare-ZnS nanobelts fabricated by removing organic molecules from the ZnS·(en)_{0.5} nanobelts (dotted). Nanostructures were suspended in water and excited at 266 nm.

Table 2-1. Photoluminescence Decay Kinetic Constants of ZnS·(en)_{0.5} Nanostructures Suspended in Water^a.

Figure 3A-1. SEM (a) and TEM (b) images of ZnS nanobelts and HRTEM image (c) and FFT pattern (d) of a ZnS nanobelt.

Figure 3A-2. EDX profile of ZnS nanobelts showing the atomic molar ratio of Zn:S to be 1:1.01, very close to the stoichiometric ratio of ZnS.

Figure 3A-3. HRTEM image of a ZnS nanobelt.

Figure 3A-4. EDX line-scanned profiles, measured along the indicated dashed line of the insetted HAADF-STEM image.

Figure 3A-5. HRXRD patterns of ZnS nanobelts. The bottom pattern is from the reference wurtzite ZnS (JCPDS Card No. 36-1450).

Figure 3A-6. Complete survey (a), Zn 2p (b), and S 2p (c) XPS spectra of ZnS nanobelts. Two green curves in c have been deconvoluted from the Gaussian fitting.

Figure 3A-7. Extinction spectrum of ZnS nanobelts suspended in ethanol. The inset shows the $(\alpha h\nu)^2$ plot against energy ($h\nu$) of the extinction spectrum after removing scattering, where α is the absorption coefficient and the solid line shows the best linear fit to estimate the band-gap energy.

Figure 3A-8. Photoluminescence spectrum of ZnS nanobelts suspended in ethanol, taken at room temperature with excitation at 266 nm. Green curves, whose peak positions are indicated inside in the units of nanometers, are Lorentzian line shape analyses deconvoluted from the red experimental spectrum.

Figure 3B-1. Schematic illustration for the growth of wurtzite ZnS nanobelts (NBs).

Figure 3B-2. HRXRD patterns of ZnS nanobelts grown with 7.5 mL of water at 180 °C for reaction times indicated in the units of h (a), grown with 7.5 mL of water for 6 h at reaction temperatures indicated in the units of °C (b), and grown for 6 h at 180 °C with water amounts indicated in the units of mL. Each bottom pattern is from the reference wurtzite ZnS (JCPDS Card No. 36-1450).

Figure 3B-3. TGA curves of ZnS nanobelts grown at 180 °C for reaction times indicated in the units of h.

Figure 3B-4. TGA curves of ZnS nanobelts grown for 6 h at reaction temperatures indicated in the units of °C.

Figure 3B-5. FTIR spectra of ZnS nanobelts grown at 180 °C for reaction times indicated in the units of h.

Figure 3B-6. FTIR spectra of ZnS nanobelts grown for 6 h at reaction temperatures indicated in the units of °C.

Figure 3B-7. Maximum-normalized Zn 2p_{3/2} (a) and S 2p (b) XPS spectra of ZnS nanobelts grown at 180 °C for reaction times indicated in the units of h.

Figure 3B-8. TEM images of ZnS nanobelts grown at 180 °C for 1.5 (a), 3 (b), 6 (c), and 18 h (d), where each scale bar indicates 200 nm.

Figure 3B-9. HAADF-STEM images of ZnS nanobelts grown at 180 °C for 6 (a) and 18 h (b), where each scale bar indicates 50 nm.

Figure 3B-10. TEM images of ZnS nanobelts grown for 6 h at 120 (a), 150 (b), and 180 °C (c), where each scale bar indicates 200 nm.

Figure 3B-11. Extinction spectra of ZnS nanobelts grown at 180 °C for reaction times indicated in the units of h. The nanobelts were suspended in ethanol.

Figure 3B-12. Photoluminescence spectra of ZnS nanobelts grown at 180 °C for reaction times indicated in the units of h. The nanobelts were suspended in ethanol and excited with 266 nm laser pulses of 6 ns.

Figure 3B-13. Photoluminescence spectra of ZnS nanobelts grown for 6 h at reaction temperatures indicated in the units of °C. The nanobelts were suspended in ethanol and excited with 266 nm laser pulses of 6 ns.

Figure 4A-1. Schematic for the fabrication of a G/ZnS device. (a) graphene transfer, (b) ZnS spin coating, (c) graphene stacking, (d) repeated b and c

steps for multiple coating and stacking, and (e) device fabrication with metal electrodes.

Figure 4A-2. (a) XRD pattern, (b) extinction spectrum (in ethanol), (c) TEM image, and (d) HRTEM image with an inserted FFT pattern of solution-grown ZnS nanobelts.

Figure 4A-3. (a) TEM and (b) HRTEM images of S-G/ZnS and SAED patterns of (c) graphene and (d) S-G/ZnS.

Figure 4A-4. Digital image of an as-fabricated device with a channel length of 80 μm .

Figure 4A-5. (a) Raman spectrum of a G/ZnS sandwich-structured device and mapping profiles (scale bar = 5 μm) of (b) the ZnS, (c) the G band, and (d) the 2D band.

Figure 4A-6. SEM images of (a) D-G/ZnS and (b) S-G/ZnS and response behaviors of photodetectors measured in air at a bias of 1.0 V based on (c) D-G/ZnS and (d) S-G/ZnS under 300 nm light illumination.

Figure 4A-7. AFM images (top) and their corresponding height profiles (bottom) of (a) D-G/ZnS and (b) composite S-G/ZnS. The height profiles were scanned along the red lines, and the green arrows indicate tent-like structures of graphene.

Figure 4A-8. Current-voltage characteristic curves of (black) graphene and (red) composite G/ZnS.

Figure 4A-9. Response behavior of a MS-G/ZnS photodetector measured in air at a bias of 1.0 V under 300 nm light illumination of 1.2 mW cm^{-2} .

Figure 4A-10. Response behaviors of a S-G/ZnS photodetector measured in air at a bias of 1.0 V under 400 (black), 500 (red), and 600 nm (blue) light illumination of 1.2 mW cm^{-2} .

Figure 4A-11. Response behaviors of as-prepared (blue) and six months-old (red) S-G/ZnS photodetectors under 300 nm light illumination.

Figure 4A-12. (a) Schematic diagram of a S-G/ZnS photodetector under light illumination and (b) energy level diagram of S-G/ZnS heterojunctions showing the charge-transfer process under UV-light illumination.

Figure 4B-1. Schematic for a plausible decomposition mechanism of an organic dye over a G/ZnS nanocomposite under light irradiation.

Figure 4B-2. XRD patterns of 0.8 G/ZnS nanocomposites (red) and ZnS nanobelts (blue).

Figure 4B-3. HRTEM images (A-C) and the elemental maps of Zn, S, and C (D-F) of 0.8 G/ZnS nanocomposites.

Figure 4B-4. Zn 2p (A), S 2p (B), C 1s (C), and O 1s (D) XPS spectra of 0.8 G/ZnS nanocomposites. The S 2p and C 1s spectra have been deconvoluted into two and three Gaussian curves, respectively.

Figure 4B-5. FTIR spectrum of 0.8 G/ZnS nanocomposites.

Figure 4B-6. Extinction spectra (A) and Kubelka-Munk plots (B) of 0.8 G/ZnS nanocomposites (red) and 0.0 G/ZnS nanobelts (blue) suspended in ethanol. The green solid lines in panel B show the best linear fits to estimate the band-gap energy.

Figure 4B-7. Concentration changes (A), first-order kinetic profiles (B), and decay rate constants (C) of RhB via indicated photocatalysts.

Table 4B-1. Catalytic degradation rate constant of 10^{-5} M RhB(aq) via nanocatalysts under irradiation of a 300 W Xe lamp

Chapter 1. General Introduction

1. 1. Nanosized and Nanostructured Materials

Nanoscience involves studying with matter on a nanoscale. Phenomena at the nanoscale are likely to be a completely new world, where properties may not be predictable from those observed at larger scales. The nanostructures' small size allows them to exhibit novel and significantly modified physical, chemical, and biological properties, which are different from those of materials in the micrometer scale. The latter mostly exhibit the same physical properties as the bulk forms. Nanoscience covers a range of techniques rather than a single discipline and stretch across the whole spectrum of science, physics, engineering, chemistry, and materials science. The ability to manipulate and process materials at the nanoscale with excellent reproducibility is vital to the advancement of manufacturing industry. "There's plenty of room at the bottom, I would like to describe a field, in which little has been done, but in which an enormous amount can be done in principle. What I want to talk about is the problem of manipulating and controlling things on a small scale...", this famous statement of legendary Richard Feynman made in 1959 at the annual meeting of the American Physical Society (APS) with immense foresight has been realized in less than half a century by consistent efforts and significant contributions from the scientific community across the world.¹ Nowadays, nanomaterials and nanostructures are not only in the forefront of the hottest fundamental materials research, but they are also gradually intruded into our daily life.

The term “nano” is derived from the Greek word for “dwarf”, “nanos” and is often used in the context of miniaturization. It is given the abbreviation n. In the international systems of units, nano is the prefix used when multiplying a unit, such as a given length, by 10^{-9} . The nano term is typically used to refer to objects with length scale approaching the order of 10^{-9} m. One nanometer is approximately the length equivalent to ten hydrogen or five silicon atoms aligned in a line. There are basically two types of size-dependent effects: quantum-confinement effects which show discontinuous behavior due to completion of shells in systems with delocalized electrons, and the fraction of atoms at the surface.

1. 1. 1. Quantum-Confinement Effects

Materials in the nanoscale range show markedly different both the chemical and physical properties from those observed in micro and bulk matter. In this intermediate size range between molecular and bulk matter, called the nanoscale, individual energy states of molecules and continuous energy bands of solids become discrete and their energy separations display an analytic dependence on the spatial dimension of the material. This is illustrated conceptually in Figure 1-1, which expresses the transformation of the electronic density of states (DOS) of valence and conduction bands in metals and semiconductors from continuous to discrete to individual in bulk, quantum-confined and molecular states of matter.² Especially, quantum-

confinement in semiconductors results from the geometric confinement of electrons and holes as independently acting ‘wave-particles’ or as bound pairs known as excitons, the representative scheme is shown in Figure 1-2.³ The normal size of an exciton in a bulk crystal, expressed as an exciton Bohr radius, provides an approximate dimension for the onset of quantum-confinement effects. When an electron-hole pair is squeezed into a nanocrystal with one or more dimensions approaching the bulk exciton Bohr radius, the effective bandgap of the semiconductor increases. The smaller the nanocrystal, the larger the effective bandgap, and the greater the energy of optical emission resulting from electron-hole recombination. Figure 1-3 shows the massive change in optical properties as a function of size in semiconductor nanocrystals. As size is reduced, the electronic excitations shift to higher energy, and the hypsochromic shift is observed both in absorption and emission spectra.⁴

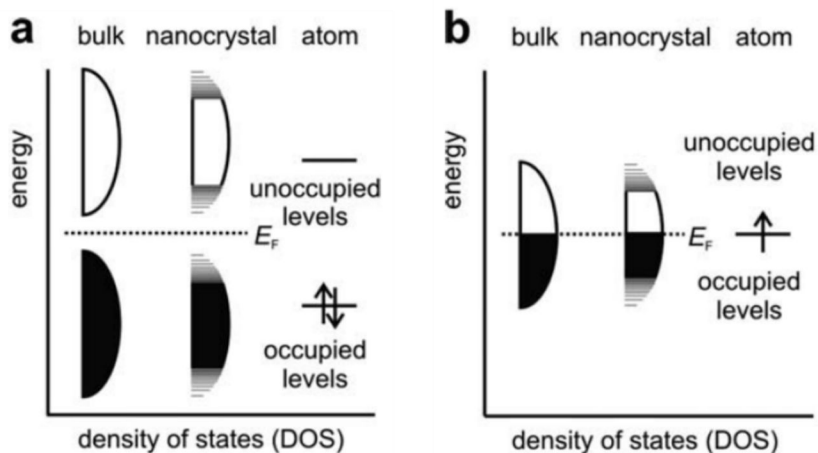


Figure 1-1. Schematic illustration of the density of states going from bulk (left) to nanocrystal (middle) to an isolated atom (right) for semiconducting (a) and metallic materials (b). Reproduced from ref. 2.

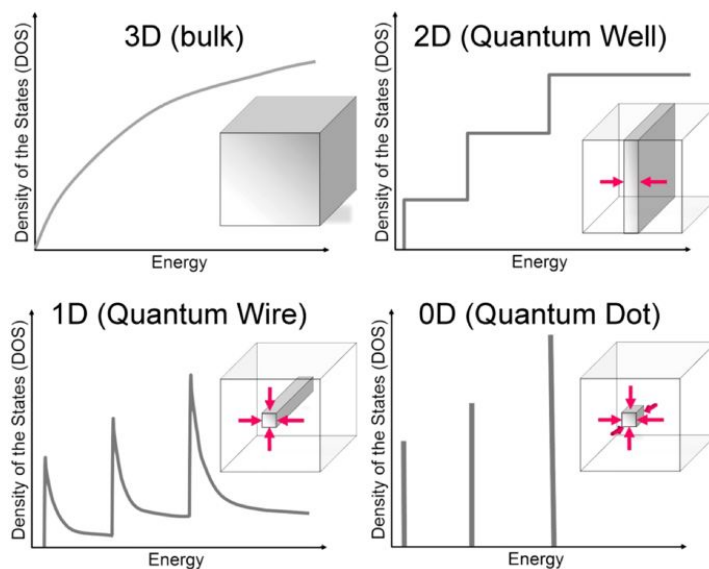


Figure 1-2. Electronic DOS for a bulk 3D crystalline material, a 2D QW, a 1D NW or NT, and a 0D QD. The insets report a cartoon showing the corresponding spatial confinement: confinement directions are defined by arrows. Reproduced from ref. 3.

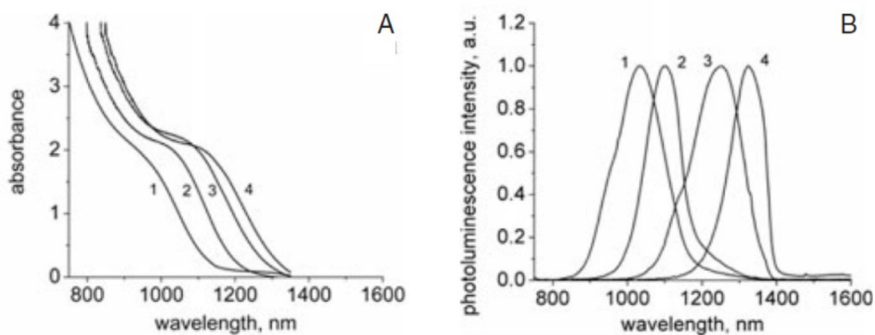


Figure 1-3. Absorption (a) and photoluminescence (b) spectra for PbS nanocrystals with different sizes, obtained by changing the Pb/S molar ratio: 1) 1:0.3, 2) 1:0.4, 3) 1:0.5, 4) 1:0.7. Reproduced from ref. 4.

1. 1. 2. Surface Effects

The surface of a sphere scales with the square of its radius r , but its volume scales with r^3 . The total number of atoms N in this sphere scales linearly with the volume. The fraction of atoms at the surface is called *dispersion* F , and it scales with surface area divided by volume, *i.e.* with the inverse radius or diameter, and thus also with $N^{-1/3}$. Basically the same relation holds for long cylinders of radius r and for thin plates of thickness d . The size dependence of dispersion is illustrated in Figure 1-4 for cubes of n atoms along an edge and a total of $N = n^3$ atoms, where the number of atoms at the surface is $6n$ corrected for double counts at the 12 edges and for reinstalling the 8 corners. For large N the edge and corner corrections become negligible, leading to the $N^{-1/3}$ scaling:⁵

$$F = \frac{6n^2 - 12n + 8}{n^3} = \frac{6}{N^{1/3}} \left(1 - \frac{2}{N^{1/3}} + \frac{8}{6N^{2/3}} \right) \approx \frac{6}{N^{1/3}}$$

Figure 1-4 shows that there are a significant number of atoms on the surface of cubic crystals, representing that properties of the surface atoms will significantly affect, and often dominate, the overall properties of the

nanomaterials. Especially, for cubic crystals as shown in Figure 1-4 the surface atoms are the least saturated ones or unoccupied coordination sites are weakly bound in comparison to the highly ordered crystalline solid of the inner atoms. For this reason, the surface atoms generally exhibit the highest affinity to form bonds to adsorbate molecules, followed by the edge and the in-plane surface atoms, a fact that is of utmost importance for the catalytic activity. Alternatively, due to their low stabilization as low coordination, edge and in particular surface atoms are often missing on single crystals even in thermodynamic equilibrium, consequently resulting in lower melting points for nanomaterials.⁶

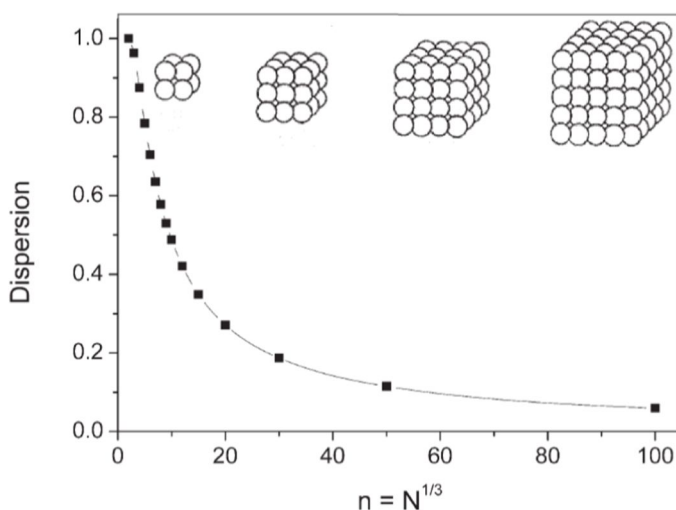


Figure 1-4. Evolution of the dispersion F as a function of n for cubic clusters up to $n = 100$ ($N = 10^6$). The structure of the first four clusters is displayed. Reproduced from ref. 5.

1. 1. 3. Applications of Nanosized Materials

Interest in the physics of condensed matter at size scales larger than those of atoms and smaller than those of bulk solids has grown rapidly since the 1970s, because of the growing understanding that the properties of these mesoscopic atomic ensembles are different from those of conventional solids, and their interesting properties as well as novel characteristics should originate from their

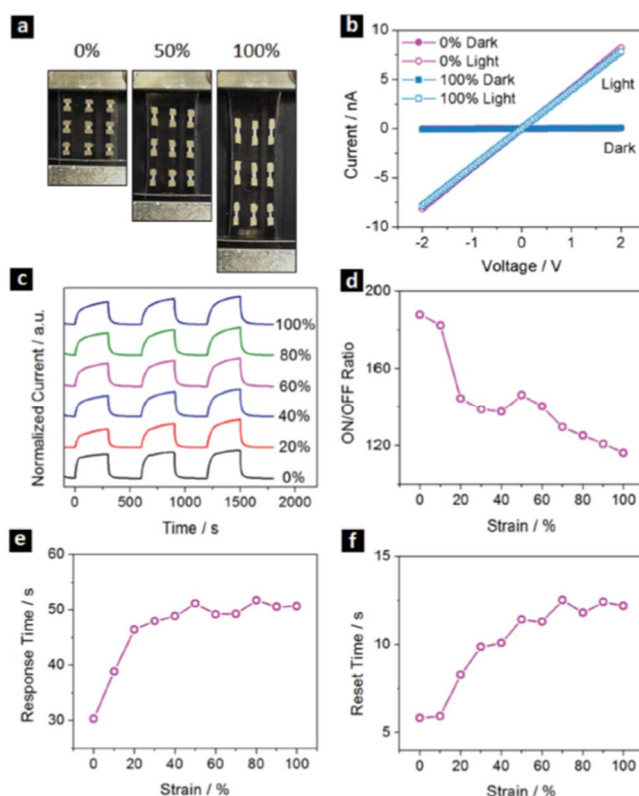


Figure 1-5. Example images (a) and switching behaviors of a stretchable device with three photodetectors connected in series (b). Cycling stability of the photodetectors at: 0% strain (c) and 80% strain (d) up to 50 cycles. Scotch

tape testing of the photodetector array (e) and corresponding response curves before and after testing at 0% strain (f). Reproduced from ref. 7.

morphologies.⁷ For example, nanosized semiconducting materials have the potential to revolutionize the fields of photodetectors⁷ and photocatalysts⁸ (shown in Figure 1-5 and 1-6) through the combined effects of quantum confinement and unique surface morphologies.⁸ As a consequence, interest in nanosized building blocks arose because their properties can be altered by controlling the size in the range of 1-100 nm and the assembly of such constituents. There is a large number of new properties and applications that could be microelectronics, where smaller has always meant a greater performance ever since the invention of transistors; e.g., higher density of integration, faster response, lower cost, and less realized by reducing the size of currently existing structures into the nanometer scale (< 100 nm) or by making new types of nanostructures. The most successful examples are seen in power consumption.⁸ Nanostructures are fundamental to nanoscience and nanotechnology and are expected to offer distinguished performance in future nanodevices.

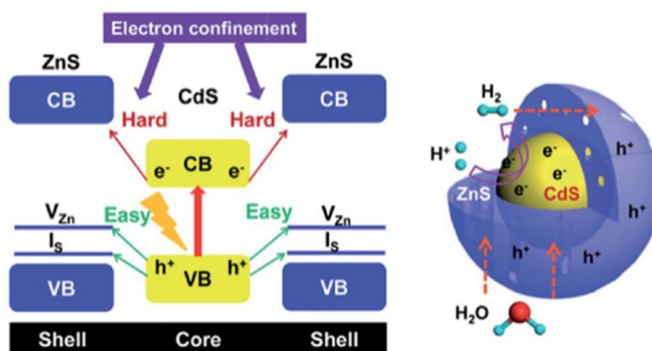


Figure 1-6. Band structure alignments of the CdS-ZnS core-shell structure and schematic of the photoexcited charge carrier distribution and related photocatalytic reactions. Reproduced from ref. 8.

1. 2. One-Dimensional Semiconductor Nanostructures

Nanostructures are modulated over nanometer length scales in zero to two dimensions. According to the number of dimensions less than 100 nm, nanostructures can be classified into two-dimensional (2D when they are planar), one-dimensional (1D when they are elongated), and zero-dimensional (0D when they are uniform) structures based on their shapes. In particular, 1D nanostructures have attracted much attention because of the confinement of the other two dimensions perpendicular to longitudinal direction. As the combination of quantum confinement in the nanoscaled dimensions and the bulk properties in another dimension, a host of interesting properties and applications can be expected based on a wide variety of 1D nanostructures. Although Feynman predicted there would be plenty of attractive properties for nanostructures as early as 1959, the great upsurge in the investigation of 1D nanostructures was triggered by the recent discovery of C₆₀, and carbon nanotubes. Recently, non-carbon based 1D nanostructures such as semiconductor based nanotubes, nanowires, nanorods, and nanobelts have been fabricated and studied intensively. Nanocircuits built using semiconductor nanowires were declared a “breakthrough in science” by *Science* magazine.⁹ *Nature* magazine published a report claiming that “Nanowire... it does not matter what you can call them, they are the hottest

property in nanotechnology.”¹⁰ Moreover, publications on 1D nanostructures have rapidly increased in the last few years and 1D nanostructures do “have the hottest property in nanotechnology”.¹⁰ There is no doubt that 1D nanostructures will be the new focal point of research in coming years. For instance, 1D semiconducting nanostructures have been demonstrated as ideal systems for exploring a large number of novel phenomena at the nanoscale and investigating the size and dimensionality dependence of their properties for potential applications. Field-effect transistors (FETs) based on individual 1D nanostructures are ultrasensitive nanosensors for detecting a wide range of gases, chemicals, and lights in both commercial and research applications. The high-performance characteristics are arisen from extremely large surface-to volume ratios and rationally designed surfaces.

1. 3. ZnS Nanostructures

With bandgaps of 3.72 and 3.77 eV for cubic zinc blende (ZB) and hexagonal wurtzite (WZ) forms at room temperature, ZnS has been extensively studied due to the intrinsic characteristics of a high index of refraction and a high transmittance in the visible range. Those mentioned characteristics have attracted great interest in the application fields of flat-panel display, light-emitting diodes, infrared windows, sensors, lasers, and photocatalysis. Recently, composited with other semiconductors or doped with transition metal ions, breakthrough progresses have been made on the potential applications of ZnS nanostructures in photoluminescence and photocatalysis. Moreover, the researches about the applications of 1D ZnS nanostructures are focused on FETs, field emission, and photodetectors.

1. 3. 1. Crystallographic Structures of ZnS

In its bulk form, ZnS is typically found to have the ZB crystal structure at room temperature. The ZB structure is cubic (Figure 1-7). At elevated temperatures, bulk ZnS can undergo a phase transformation from the cubic ZB structure to a hexagonal crystal structure known as the WZ structure (Figure 1-7). This transformation has been shown to occur at 1020 °C. The ZB and WZ structures are very similar. The stacking sequence of the close-packed planes of ZB (the (111) planes) is represented by the ABCABCABCABC

repeating pattern. However, if the close-packed planes stack themselves in the ABABABABAB repeating pattern, they would form the (0001) planes of the WZ structure. WZ has a hexagonal unit cell (space group $P63mc$). The structure of ZnS can be described as a number of alternating planes composed of tetrahedrally coordinated S^{2-} and Zn^{2+} ions, stacked alternately along the c-axis. The tetrahedral coordination in ZnS results in a non-centrosymmetric structure and piezoelectricity.

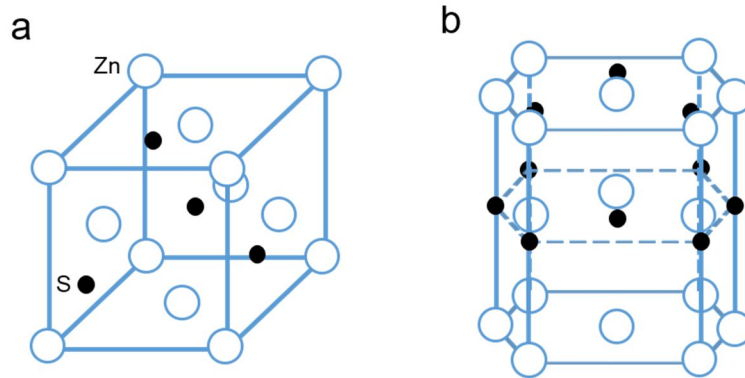


Figure 1-7. The zinc blend (a) and wurtzite (b) crystal structures of ZnS.

A common characteristic II–VI semiconductors share is a propensity to form into the WZ crystal structure when their sizes are small. WZ is the most stable structure for CdS and CdSe and the other II–VI semiconductors have previously been observed to exhibit the WZ crystal structure. Another important characteristic of ZnS is the polar surfaces. The most common polar surface is the basal plane. The oppositely charged ions produce positively

charged Zn-(0001) and negatively charged S-(000-1) polar surfaces, resulting in a normal dipole moment and spontaneous polarization along the c-axis as well as a divergence in surface energy. WZ ZnS produces anisotropic growth for two reasons. One is merely that different crystallographic planes have different surface energy. Another reason is the surface polarity and chemical activities. Together with the polar surfaces due to cation/anion termination, ZnS exhibits a wide range of novel structures by tuning the growth rates along these directions. The non-centrosymmetry in WZ gives rise to piezoelectricity, which has been used for fabricating cantilevers for scanning probe microscopy. Nanocantilevers could be used in mass, biological, force, thermal, pressure, and chemical sensing applications. Through the successful synthesis of II–VI semiconductors in a nanobelt form, a wide range of mechanical and optoelectronic application may be possible for these materials. This is why II–VI semiconductors and ZnS remain a fast developing area of research.

1. 3. 2. Optical Properties of ZnS Nanostructures

The exciton binding energy of ZnS is 40 meV, which makes it an excellent candidate for exploring the intrinsic recombination processes in dense exciton systems. Although much research has been devoted to the photoluminescence (PL) and the cathodoluminescence (CL) of 1D ZnS nanostructures, very few studies have been reported on their possible ultraviolet bandgap emission at

room temperature. Optical properties of ZnS nanostructures are very sensitive to the synthetic conditions, its crystal size and shape, and intrinsic defects such as vacancies and interstitials.

As the literature documents, for a large number of 1D ZnS nanostructures with various shapes synthesized using different synthetic methods, in general, visible-emission peaks are observed. For example, Wang et al. reported the preparation of single-crystalline high-purity ZnS nanowires via a simple thermal evaporation method in the presence of an Au catalysts. Figure 1-8 shows that two emission bands (450 and 520 nm) have been detected in the PL spectra. The authors attributed these emission peaks to the surface states of ZnS nanowires and the presence of Au ions.¹² An alternative method using hydrazine hydrate as a solvent, bundles of wurtzite ZnS nanowires with diameters of 10-25 nm and lengths of 5-8 μ m have been synthesized via a solvothermal route. As shown in Figure 1-8, PL measurements revealed one weak peak at 465 nm and two strong peaks at 413 and 438 nm. The authors suggested that the S vacancies and interstitial S atoms and surface states could be responsible for the strong emission bands at 413 and 428 nm and a weak peak at 465 nm, respectively.¹³ However, those the mentioned works do not show ultraviolet (UV) bandgap emission originating in excitonic transition from the conduction band to the valence band of ZnS nanostructures.

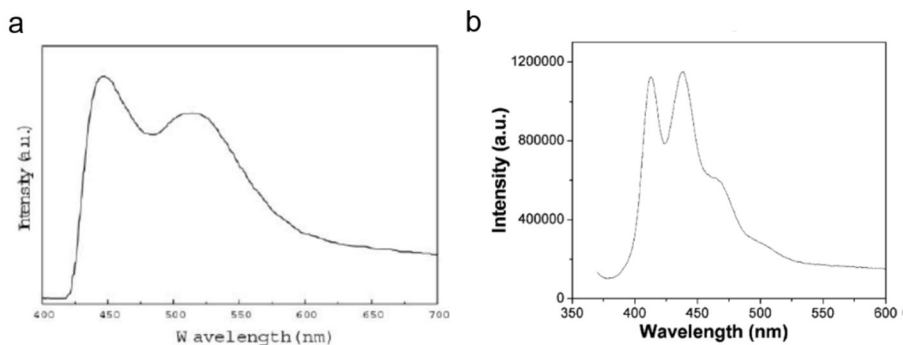


Figure 1-8. Room-temperature PL spectra of ZnS nanowires via thermal evaporation method (a) and ZnS nanowires via solvothermal method (b). Reproduced from refs. 12 and 13.

ZnS nanostructures showing sharp band-edge luminescence at room temperature have been hardly reported, because of its difficulty to control the surface and crystal quality of ZnS nanostructures. Some of representative works related in UV bandgap emitting ZnS nanostructures are introduced below. Multiangular branched ZnS nanostructures with needle-shaped tips was synthesized via conventional thermal evaporation in a horizontal tube furnace. High-spatial-resolution CL from individual ZnS multiangular branched nanostructures was investigated with the nanometer resolution. The size-dependent optical spectra exhibited sharp UV bandgap emission and broad visible emission at room temperature. Figure 1-9a shows CL spectrum of multiangular branched ZnS nanostructures, which consists of a sharp UV emission band at 334 nm and a broad visible emission band centered at 404 nm. The intensity ratio between the UV emission and visible emission is 1/10.

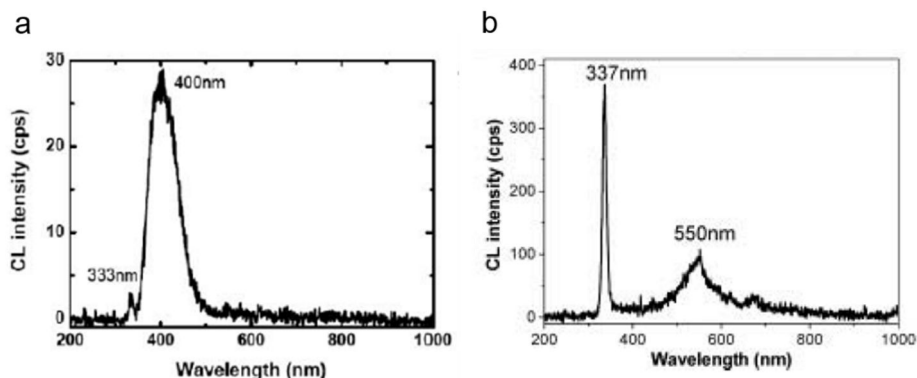


Figure 1-9. CL spectra recorded at room temperature from (a) multiangular branched ZnS nanostructures (a) and single-crystalline ZnS nanobelts (b). Reproduced from refs. 14 and 15.

Fang et al. reported another important works in bandgap luminescent single-crystalline ZnS nanobelts synthesized by a CVD method. It was conclusively found that the right selection of source materials and controlling their evaporation and agglomeration rates are the key parameters for the achievement of single-crystalline ZnS nanobelts possessing sharp UV emission at room temperature. Detailed CL properties from individual ZnS nanobelts were investigated with a nanometer-scale resolution. Figure 1-9b shows two emission bands composed of a narrow and strong UV peak centered at 337 nm and broad low-intensity luminescence in the visible region of ~550 nm. Wet-chemically synthesized ZnS nanostructures have often found to have a sphere-like morphology capped with long carbon-chain ligands, showing no band-edge emission and hardly reported with 1D morphology with single-crystalline structure. Wurtzite ZnS nanobelts with narrow band-edge luminescence at room temperature have been synthesized via mild

hydrothermal process involving ternary solvents of hydrazine, ethylenediamine, and water. As-synthesized nanobelts have uniform cross sections along their lengths, with a mean width of 80 nm, a typical thickness of 16 nm, and an average length of 990 nm. The room-temperature PL spectrum of ZnS nanobelts (shown in Figure 1-10) under an average excitation fluence of 80 mW/cm^2 consists of a strong UV emission band at 326.4 nm (3.799 eV) with a half width at the half maximum (HWHM) of 6.4 nm and a weak visible emission band at 414.7 nm. The UV emission originated from band-edge transitions of excitons and the visible emission arisen from sulfur vacancies to the valence band and surface states. The measured peak-intensity ratio of the UV emission band to the visible emission band is 21.5, indicating that the band-edge transition of free excitons is the major radiational pathway of ZnS nanobelts.

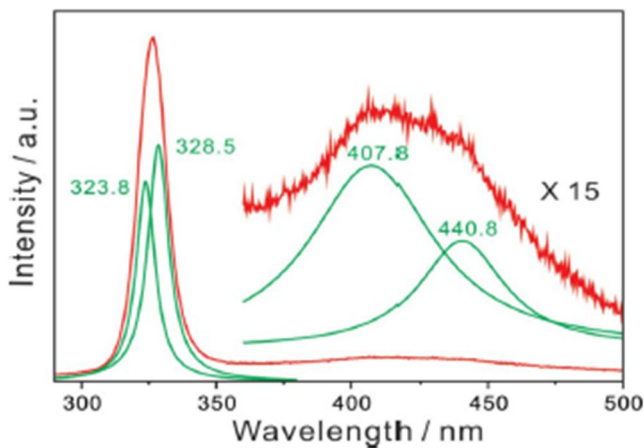


Figure 1-10. PL spectrum of ZnS nanobelts suspended in ethanol, taken at room temperature with excitation at 266 nm. Green curves, whose peak positions are indicated inside in the units of nanometers, are Lorentzian line

shape analyses deconvoluted from the red experimental spectrum. Reproduced from ref. 16.

1. 3. 3. Synthesis of 1D ZnS Nanostructures

Several methods have been developed to synthesize 1D ZnS nanostructures. Among these are thermal evaporation, laser ablation, arc discharge, chemical synthesis methods, and self-assembly methods. Physical and chemical vapor deposition (PVD and CVD) methods are the most common deposition-based synthetic routes, which is schematically illustrated in Figure 1-11.¹⁷⁻¹⁹ Both methods consist of the physical transport of the vapor species to the deposition site. In the case of PVD, the vapor species is typically created through the thermal evaporation of a source that is a bulk version of the desired nanomaterial. Most of these materials are commercially available in powder or chunk form. The main benefit of PVD is that it can provide for easy control over the chemistry of the synthesized material, with relatively little control of the system parameters. In the case of CVD, the vapor species is created through a chemical reaction. For example, a Zn source may be evaporated and reacted with a H₂S flow gas to form a ZnS vapor species.²⁰ However, because of the chemical reaction involved, controlling the atmosphere is extremely important with CVD and achieving the correct setup can be very difficult. The benefit of CVD is that it typically can be synthesized with much lower initial temperatures than with PVD.²¹

Those vapor-phase techniques usually suffer from high cost owing to the usage of expensive instruments and complicated processes. As an alternative, the fabrication of 1D ZnS nanostructures through a low-temperature solution route may have advantages of mild synthetic conditions and economic methods as well as large scale production. The hydrothermal and solvothermal (using non-water as solvents) method has been demonstrated to be one of the most important technologies for producing 1D nanostructures at low temperature.

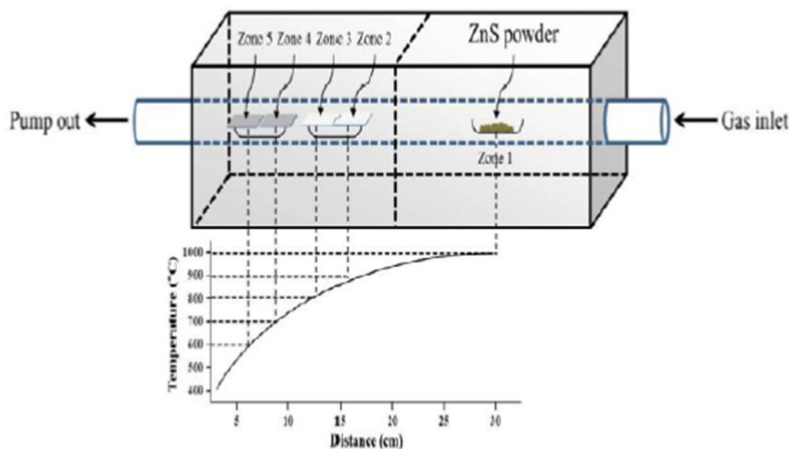


Figure 1-11. Schematic diagram of the thermal evaporation system used to synthesize the ZnS 1D nanostructures and a plot of temperature versus substrate temperature showing four different substrate temperature zones: zone 2 (~900 °C), zone 3 (~800 °C), zone 4 (~700 °C) and zone 5 (~600 °C). Reproduced from ref. 17.

Hydrothermal technique can be defined as a synthetic method of single crystals that depends on the solubility of minerals in hot water under high

pressure. The crystal growth is performed in an apparatus consisting of a steel pressure vessel called a Teflon-lined stainless-steel autoclave (Figure 1-12). These wet-chemical based hydrothermal and solvothermal synthetic routes have been found to be advantageous particularly from viewpoints of environmental friendliness, easy upward scaling, and low production cost. In 2006, Cai and co-workers reported the synthesis of large-scale and well-aligned ZnS nanobelts arrays via a simple hydrothermal method and subsequent heat at 250 °C. Subsequently, Shi and Huo reported a mild one-step solvothermal method for growing uniform well-aligned 1D nanostructures.



Figure 1-12. Photograph of Teflon-lined stainless steel autoclaves with different volumes. Reproduced from ref. 22.

1. 4. References

(1) R. Feynman, *Eng. Sci.*, **1960**, 23, 22.

- (2) T. Laaksonen, V. Ruiz, P. Lilijeroth and B. M. Quinn, *Chem. Soc. Rev.*, **2008**, *37*, 1836.
- (3) L. Mino, G. Agostini, E. Borfecchia, D. Gianolio, A. Piovano, E. Gallo and C. Lamberti, *J. Phys. D: Appl. Phys.*, **2013**, *46*, 423001.
- (4) L. Bakueva, I. Gorelikov, S. Musikhin, X. S. Zhao and E. H. Sargent, *Adv. Mater.*, **2004**, *16*, 926.
- (5) E. Roduner, *Nanoscopic Materials: Size-Dependent Phenomena*. *The Royal Society of Chemistry*, Cambridge, **2006**.
- (6) A. P. Alivisatos, *Science*, **1996**, *271*, 933.
- (7) C. Yan, J. Wang, X. Wang, W. Kang, M. Cui, C. Y. Foo and P. S. Lee, *Adv. Mater.*, **2014**, *26*, 943.
- (8) Y. P. Xie, Z. B. Yu, G. Liu, X. L. Ma and H.-M. Cheng, *Energy Environ. Sci.*, **2014**, *7*, 1895.
- (9) R.F. Service, *Science*, **2001**, *293*, 782.
- (10) D. Appell, *Nature*, **2002**, *419*, 553.
- (11) D. Moore and Z. L. Wang, *J. Mater. Chem.*, **2006**, *16*, 3898.
- (12) Y. W. Wang, L. D. Zhang, C. H. Liang, G. Z. Wang and X. S. Peng, *Chem. Phys. Lett.*, **2002**, *357*, 314.
- (13) L.W. Yin, Y. Bando, J. H. Zhan, M. S. Li and D. Golberg, *Adv. Mater.*, **2005**, *17*, 1972.
- (14) X.S. Fang, U.K. Gautam, Y. Bando, B. Dierre, T. Sekiguchi and D. Golberg, *J. Phys. Chem. C*, **2008**, *112*, 4735.

- (15) X.S. Fang, Y. Bando, M.Y. Liao, U.K. Gautam, C.Y. Zhi, B. Dierre, B.D. Liu, T. Y. Zhai, T. Sekiguchi, Y. Koide and D. Golberg, *Adv. Mater.*, **2009**, *21*, 2034.
- (16) Y. Kim and D.-J. Jang, *RSC Adv.*, **2013**, *3*, 16945.
- (17) C. Jin, H. Kim, S. Park, S. Ann and C. Lee, *Phys. Scr.*, **2013**, 014043.
- (18) R. Chen, D. Li, B. Liu, Z. Peng, G. G. Gurzadyan, Q. Xiong and H. Sun, *Nano Lett.*, **2010**, *10*, 4956.
- (19) S. Chen, L. Li, X. Wang, W. Tian, X. Wang, D.-M. Tang, Y. Bando and D. Golberg, *Nanoscale*, **2012**, *4*, 2658–2662.
- (20) Y. Jiang, X. Meng, J. Liu, Z. Xie, C. S. Lee and S.-T. Lee, *Adv. Mater.*, **2003**, *15*, 323.
- (21) Z. X. Zhang, J. X. Wang, H. J. Yuan, Y. Gao, D. F. Liu, L. Song, Y. J. Xiang, X. W. Zhao, L. F. Liu, S. D. Luo, X. Y. Dou, S. C. Mou, W. Y. Zhou and S. S. Xie, *J. Phys. Chem. B*, **2005**, *109*, 18352.
- (22) M.-R. Gao, Y.-F. Xu, J. Jiang and S.-H. Yu, *Chem. Soc. Rev.*, **2013**, *42*, 2986.

**Chapter 2. One-Pot and Template-Free Fabrication of
ZnS·(ethylenediamine)_{0.5} Hybrid Nanobelts[†]**

[†]This is reproduced from Yeonho Kim, Jong-Yeob Kim, and Du-Jeon Jang, *J. Phys. Chem. C* **2012**, *116*, 10296. © 2012 American Chemical Society.

2. 1. Abstract

A template-free and one-pot solvothermal process has been developed for the facile synthesis of $\text{ZnS}\cdot(\text{en})_{0.5}$ (en =ethylenediamine) hybrid nanobelts having diverse length-to-width (aspect) ratios. While typical hybrid nanobelts synthesized at 180 °C for 6 h have an average width of 130 nm, a mean thickness of 55 nm, and an average length of 16 μm , their aspect ratios have been varied by adjusting solvent volume ratios of hydrazine monohydrate (hm) to en. A sufficient amount of sulfide from the reduction of sulfur by hm has been found to be essential for the efficient anisotropic one-dimensional growth of highly crystalline $\text{ZnS}\cdot(\text{en})_{0.5}$ hybrid nanobelts. The photoluminescence spectra of $\text{ZnS}\cdot(\text{en})_{0.5}$ hybrid nanostructures exhibit three bands located at 327, 415–430, and 587–654 nm, which are assigned to band-edge emission, trap sites-related emission, and anion-vacancy emission, respectively. The mean lifetime of photoluminescence having three decay components of 30, 170, and 2700 ps decreases with the volume ratio of hm to en due to the decrease of defect sites with the increase of the aspect ratios of $\text{ZnS}\cdot(\text{en})_{0.5}$ hybrid nanobelts. Compared with bare-ZnS nanobelts prepared by the hydrothermal treatment of $\text{ZnS}\cdot(\text{en})_{0.5}$ hybrid nanobelts, hybrid ones have shown enhanced optical properties that would give them potential for optoelectronic devices.

2. 2. Introduction

The controlled fabrication, characterization, and application of nanometer-sized metals and semiconductors with functional properties have been studied widely.¹⁻⁴ In particular, one-dimensional nanoscale building blocks such as nanowires, nanorods, nanotubes, and nanobelts have been investigated extensively because of their potential applications in various fields. Compared with common one-dimensional nanostructures, nanobelts as representative quasi-one-dimensional nanostructures with improved electrical contact have attracted considerable attention due to their proven use as both interconnects and functional units in electronic, optoelectronic, electrochemical, and electromechanical devices.⁵⁻⁹ ZnS is an important II-VI semiconductor compound with a wide band-gap energy of 3.66 eV at room temperature, and it attracts intense interest due to its excellent properties of luminescence which enable ZnS to have applications in the fields of UV-light emitting diodes, efficient phosphors, sensors, and catalysts.¹⁰⁻¹⁴ From the viewpoint of applications, one-dimensional ZnS nanostructures with highly aligned and ordered patterns are greatly demanded to become the current focus of research, and used as building blocks for nanoelectronic and nanophotonic systems because of their enhanced properties significantly different from those of their bulk counterparts.¹⁵ Up to now, different methods such as metal-organic chemical vapor deposition, electrochemical deposition, template assistance, and thermal evaporation have been developed for the synthesis of one-

dimensional ZnS nanostructures.¹⁶⁻¹⁸ Commonly, these synthetic strategies need relatively rigid experimental conditions and sophisticated equipments. On the contrary to these, a solution-based approach such as a solvothermal process has advantages of mild synthetic conditions and economical methods for the fabrication of one-dimensional ZnS nanostructures, especially because this approach does not require toxic gases or high-temperature processing steps.¹⁹ However, there are few reports on the synthesis of ZnS nanobelts *via* a solvothermal process.²⁰ This may be due to the fact that it is generally difficult to control the nucleation and growth of ZnS for the fabrication of well-defined one-dimensional nanostructures.

Inorganic-organic hybrid materials with one-dimensional structures have received much attention because of their tremendous potential in providing enhanced materials properties that are not easily achievable with either organic or inorganic materials alone.²¹ For example, II–VI-based one-dimensional hybrid semiconductors, MQ-(L)_n (M = Zn, Cd, Mn; Q = S, Se, Te; L = hydrazine, ethylenediamine (en), cyclohexylamine; *n* = 0.5 or 1) have been demonstrated to be a new family of multifunctional hybrid materials.²¹⁻²⁴ These hybrid materials normally exhibit tunable physical properties and significantly enhanced electronic and optical properties including a giant band-gap tunability as a result of strong quantum confinement effect and high band-edge absorption. The hybrid materials have additional advantage of possessing perfectly ordered crystal structures and thus allowing high carrier mobility. Furthermore, the hybrid materials are much lighter and more

flexible compared with their inorganic counterparts, and thus are most desirable for low-weight and flexible electronic devices. Because hybrid materials with one-dimensional structures are remarkably advantageous, there have been many corresponding works on the ZnS-based hybrid nanostructures.²⁵⁻²⁹ Although the preparation of ZnS·(en)_{0.5} hybrid nanosheets was already reported, the synthesis and characterization of ZnS·(en)_{0.5} hybrid nanobelts have been reported hardly.²⁵ Many researchers have used ethylenediamine (en) as organic spacer molecules or template molecules for the synthesis of II–VI-based one-dimensional hybrid semiconductors. And, en molecules, which serve as bridged ligands between two metal atoms in neighboring inorganic layers, also prevent these inorganic slabs from collapsing and condensing into the bulk phase. A solvent coordination molecular template mechanism was already proposed with an emphasis on the role of the en molecule in assisting the anisotropic crystal growth.³⁰

In the present study report a template-free and one-pot solvothermal process for the synthesis of ZnS·(en)_{0.5} hybrid nanobelts having diverse length-to-width (aspect) ratios. Hybrid nanobelts with distinct three emission bands have been prepared by a facile solvothermal route in a mixed solvent system containing a variable volume ratio of hydrazine monohydrate (hm) to en. The reaction medium consisting of mixed solvents has played an important role in the morphology and crystallinity of the nanostructures. As-synthesized hybrid nanobelts show different optical properties compared with bare-ZnS nanobelts fabricated by a hydrothermal treatment of ZnS·(en)_{0.5}

hybrid nanobelts. The photoluminescence properties, as well as the crystallinity and size, of $\text{ZnS}\cdot(\text{en})_{0.5}$ hybrid nanostructures can be varied by adjusting volume ratios of hm to en without changing precursor molecules and without doping impurities. Thus, the simple and mild solution approach to synthesize inorganic-organic hybrid nanobelts with obvious advantages over the traditional high-temperature approach could be applicable to other II–VI semiconductor nanomaterials. Furthermore, our fabrication method of $\text{ZnS}\cdot(\text{en})_{0.5}$ hybrid nanobelts with controlled structures and improved optical properties is considered to enhance their potential application as nanoscale optoelectronic devices and catalysts in pollutant treatment.

2. 3. Experimental Details

Synthesis. The analytical grade chemicals of $\text{ZnCl}_2(\text{s})$, $\text{S}(\text{s})$, $\text{N}_2\text{H}_4\cdot\text{H}_2\text{O}(\text{l}, \text{hm})$, and $\text{C}_2\text{H}_4(\text{NH}_2)_2(\text{l}, \text{en})$ were used as purchased from Sigma-Aldrich. Deionized water with a resistivity of greater than $18 \text{ M}\Omega \text{ cm}$, from a Millipore Milli-Q system, was used throughout the experiments. For the typical preparation of $\text{ZnS}\cdot(\text{en})_{0.5}$ hybrid nanostructures, 0.5 mmol of ZnCl_2 , 0.5 mmol of S , and a volume (7.5 , 15.0 , or 20.0 mL) of en (V_{en}) were added to a volume of hm ($V_{\text{hm}} = 30.0 \text{ mL} - V_{\text{en}}$) and stirred vigorously for 1 h . The mixture solution was then loaded into a Teflon-lined stainless-steel autoclave of 50 mL capacity, placed in a preheated oven at $180 \text{ }^\circ\text{C}$ for 6 h , and cooled to

room temperature naturally. A white precipitate produced in the reaction mixture was washed twice with deionized water and ethanol to remove residual impurities. Bare-ZnS nanobelts were then fabricated by treating ZnS·(en)_{0.5} hybrid nanobelts hydrothermally for 10 h at 120 °C in a Teflon-lined stainless-steel autoclave. Colloidal samples were prepared by re-dispersing the prepared hybrid nanostructures in deionized water immediately prior to use in order to avoid the precipitation and the decomposition of nanostructures in water.

Characterization. While transmission electron microscopy (TEM) images were obtained with a Hitachi H-7600 microscope, high-resolution transmission electron microscopy (HRTEM) images and fast Fourier transformation (FFT) patterns were measured using a JEOL JEM-3000F microscope. Scanning electron microscopy (SEM) images were obtained with a JEOL-6700F microscope, and high-resolution X-ray diffraction (HRXRD) patterns were obtained with a Bruker D8 DISCOVER diffractometer using Cu K_α radiation (0.15418 nm). X-ray photoelectron spectroscopy (XPS) spectra were monitored using a AXIS-His system with an excitation source of Mg K_α (1253.60 eV), and Raman spectra were measured with a HORIBA Jobin Yvon T64000 spectrometer with excitation using 514 nm light from an Ar⁺ laser. While extinction spectra were obtained with a Scinco S3100 UV/vis spectrophotometer, photoluminescence spectra were measured employing a Princeton Instruments ICCD576G CCD detector with excitation using 266 nm pulses having a duration time of 6 ns from a Q-switched Quantel Brilliant

Nd:YAG laser. Photoluminescence kinetic profiles were measured using a Hamamatsu C2830 streak camera of 10 ps attached with a Princeton Instruments RTE128H CCD detector after exciting samples with 266 nm pulses from a mode-locked Quantel YG501 Nd:YAG laser of 25 ps. Photoluminescence kinetic constants were extracted by fitting measured kinetic profiles to computer-simulated exponential curves convoluted with instrument response functions.

2. 4. Results and Discussion

The SEM and TEM images of Figure 2-1a show that syntheses performed with $V_{\text{hm}}/V_{\text{en}}$ of 3 give nanobelts having well-defined uniform widths over their entire lengths, with an average width of 130 nm, a mean thickness of 55 nm, and a typical length of 16 μm . It will be shown later that these products are $\text{ZnS}\cdot(\text{en})_{0.5}$ hybrid nanobelts. The comparison of the SEM and TEM images in Figure 2-1 reveals that the lengths of the nanostructures have increased whereas their widths have decreased with the increment of $V_{\text{hm}}/V_{\text{en}}$. Thus, the aspect ratios of $\text{ZnS}\cdot(\text{en})_{0.5}$ hybrid nanostructures increase with the increment of $V_{\text{hm}}/V_{\text{en}}$. These results suggest that the mixed solvent system containing hm and en has played an important role in the morphology of the nanostructures. Based on experimental data, large value of $V_{\text{hm}}/V_{\text{en}}$ has been found to be essential for the growth of flexible and well-defined $\text{ZnS}\cdot(\text{en})_{0.5}$

hybrid nanobelts. Therefore, an excess amount of en and an insufficient amount of sulfide ions (see below)

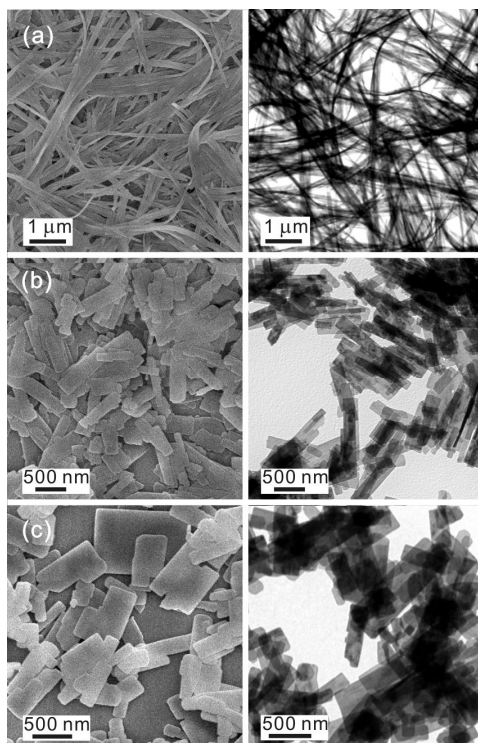


Figure 2-1. SEM (left) and TEM (right) images of $ZnS \cdot (en)_{0.5}$ nanostructures grown at 180 °C for 6 h with V_{hm}/V_{en} of 3 (a), 1 (b), and 0.5 (c).

induce nanostructures to grow with small aspect ratios. The microstructural details of $ZnS \cdot (en)_{0.5}$ hybrid nanostructures have been further provided by measuring the HRTEM images and the FFT patterns of Figure 2-2. The HRTEM images of Figure 2-2 show that the hybrid nanobelt synthesized with V_{hm}/V_{en} of 3 has a single-domain crystallite whereas hybrid nanostructures synthesized with V_{hm}/V_{en} of 1 and 0.5 have multi-domain crystallites. These are also clearly seen from the FFT patterns of Figure 2-2. Comparing the inset

of Figure 2-2a with those of Figure 2-2b and 2c, the number of discrete spots increases with the increment of $V_{\text{hm}}/V_{\text{en}}$. In other words, ring FFT patterns due

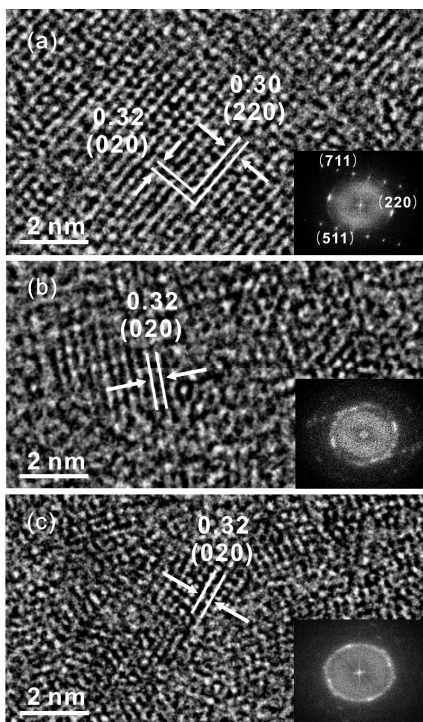


Figure 2-2. HRTEM images of $\text{ZnS}\cdot(\text{en})_{0.5}$ nanostructures grown at $180\text{ }^\circ\text{C}$ for 6 h with $V_{\text{hm}}/V_{\text{en}}$ of 3 (a), 1 (b), and 0.5 (c) show lattice plane distances in nm. The insets show FFT patterns obtained from the corresponding nanostructures.

to polycrystalline structures have appeared when nanosheets were grown with $V_{\text{hm}}/V_{\text{en}}$ of 1 and 0.5, and discrete spots have evolved to exist when hybrid nanobelts were grown with $V_{\text{hm}}/V_{\text{en}}$ of 3. The lattice-fringe distances of 0.30 and 0.32 nm calculated from the HRTEM images of Figure 2-2 have been assigned to the spacing lengths of the (220) and the (020) planes, respectively, of the orthorhombic $\text{ZnS}\cdot(\text{en})_{0.5}$ structure. The typical FFT pattern of Figure 2-

2a also suggests that the nanobelt has the crystalline structure of the orthorhombic $\text{ZnS} \cdot (\text{en})_{0.5}$. Consequently, both the HRTEM image and the FFT pattern of Figure 2-2a indicate that a $\text{ZnS} \cdot (\text{en})_{0.5}$ hybrid nanobelt fabricated with $V_{\text{hm}}/V_{\text{en}}$ of 3 shows a well-defined and single-crystalline structure.

Figure 2-3 shows the HRXRD patterns of $\text{ZnS} \cdot (\text{en})_{0.5}$ hybrid nanostructures as-prepared *via* a solvothermal process with different reaction conditions of time and $V_{\text{hm}}/V_{\text{en}}$. The 2θ positions and the relative intensities of as-observed reflection peaks are in good agreement with the respective ones of $\text{ZnS} \cdot (\text{en})_{0.5}$ nanostructures reported in the literature,^{31,33-35} indicating that $\text{ZnS} \cdot (\text{en})_{0.5}$ hybrid nanostructures have been successfully synthesized under current experimental conditions.

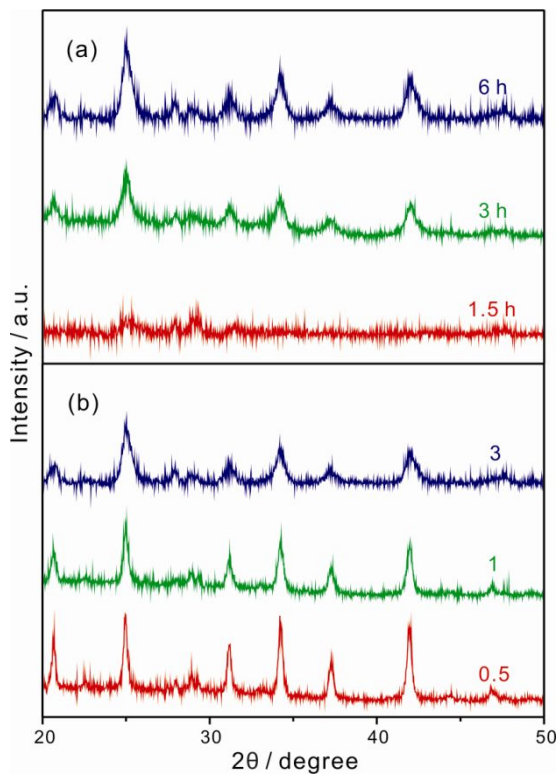


Figure 2-3. HRXRD patterns of ZnS·(en)_{0.5} nanostructures grown at 180 °C with $V_{\text{hm}}/V_{\text{en}}$ of 3 during various reaction periods indicated inside (a), and for 6 h with various ratios of $V_{\text{hm}}/V_{\text{en}}$ indicated inside (b).

It is suggested that our en-intercalated ZnS hybrid nanostructures of ZnS·(en)_{0.5} have lamella-like structures with ZnS nanolayers ordered *via* bridging en spacers.³¹ The HRXRD patterns of Figure 2-3a designate that the crystallinity of ZnS·(en)_{0.5} hybrid nanobelts has enhanced highly with the increment of the reaction time. This suggests that a sufficient reaction time as long as 6 h is essential for the growth of well-defined and high-crystalline ZnS·(en)_{0.5} hybrid nanobelts. The mean crystallite diameter, d , can be determined from the line width of a HRXRD spectrum by the Scherrer's formula $\langle d \rangle = (0.94 \lambda) / (B \cos \theta_B)$, where λ is the X-ray wavelength, B is the full width at the half maximum of the diffraction peak (radian), and θ_B is the half angle of the diffraction peak on the 2θ scale.³⁶ The mean crystallite diameters of ZnS·(en)_{0.5} hybrid nanobelts grown for 3 and 6 h, estimated by using the peak at 2θ of 42°, are 26 and 28 nm, respectively. The peak at 42° has been assigned to the (711) or (620) direction,^{31,33} thus suggesting that ZnS·(en)_{0.5} hybrid nanobelts grow preferentially in the direction of (711) or (620) to induce an anisotropic one-dimensional growth of nanobelts. Figure 2-3b shows that broad HRXRD peaks have been induced by the increment of $V_{\text{hm}}/V_{\text{en}}$. The relatively broad HRXRD peaks reveal that the average crystallite size of the ZnS·(en)_{0.5} hybrid nanostructures has decreased with the increment of $V_{\text{hm}}/V_{\text{en}}$. The mean crystallite diameters of ZnS·(en)_{0.5} hybrid

nanostructures have been estimated to be 28, 49, and 55 nm at $V_{\text{hm}}/V_{\text{en}}$ values of 3, 1, and 0.5, respectively. The HRXRD patterns of nanostructures in Figure 2-3b are nearly independent of the $V_{\text{hm}}/V_{\text{en}}$ ratio. This indicates that both the compositions and the microscopic structures of as-prepared $\text{ZnS}\cdot(\text{en})_{0.5}$ are the same regardless of $V_{\text{hm}}/V_{\text{en}}$, which, however, has changed the aspect ratios of $\text{ZnS}\cdot(\text{en})_{0.5}$ nanocomposites significantly (Figures 2-1 and 2-2).

The Raman peaks of Figure 2-4 at 216 and 284 cm^{-1} are attributed to a longitudinal acoustic mode and a transverse optic mode of $\text{ZnS}\cdot(\text{en})_{0.5}$ hybrid nanostructures, respectively.³⁷ The positions and relative intensities of both peaks do not change with $V_{\text{hm}}/V_{\text{en}}$. Thus, together with Figure 2-3b, Figure 2-4 suggests that the microscopic structures of $\text{ZnS}\cdot(\text{en})_{0.5}$ nanocomposites are almost identical regardless of $V_{\text{hm}}/V_{\text{en}}$. The sharp and strong diffraction peaks appearing in the HRXRD patterns of Figure 2-3 indicate clearly that well-crystallized $\text{ZnS}\cdot(\text{en})_{0.5}$ hybrid nanostructures have been successfully synthesized *via* one-pot and template-free solvothermal process.

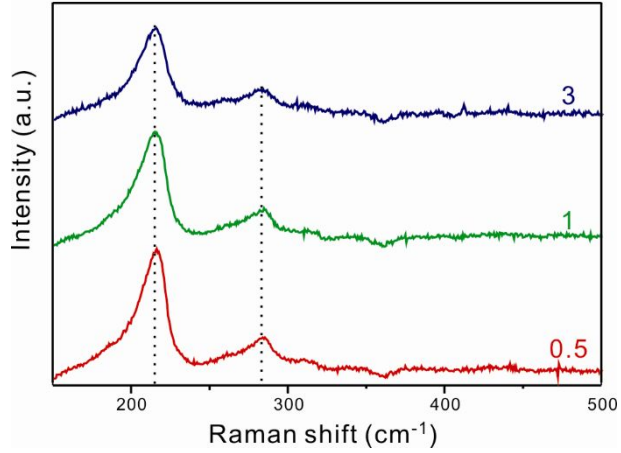


Figure 2-4. Raman spectra of $\text{ZnS}\cdot(\text{en})_{0.5}$ nanostructures grown at $180\text{ }^\circ\text{C}$ for 6 h with $V_{\text{hm}}/V_{\text{en}}$ of 3 (blue), 1 (green), and 0.5 (red).

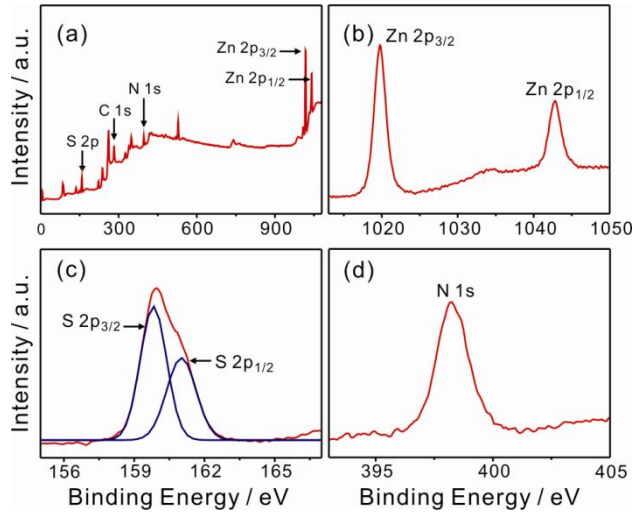


Figure 2-5. Complete survey (a), Zn 2p (b), S 2p (c), and N 1s (d) XPS spectra of $\text{ZnS}\cdot(\text{en})_{0.5}$ nanobelts grown at $180\text{ }^\circ\text{C}$ for 6 h with $V_{\text{hm}}/V_{\text{en}}$ of 3.

The XPS data of Figure 2-5 can provide further significant information about the surface composition of the $\text{ZnS}\cdot(\text{en})_{0.5}$ hybrid nanobelts. The binding energies obtained in the XPS analysis were corrected for specimen charging, through referencing the C 1s to 283.5 eV. The survey spectrum of Figure 2-5a shows that N and C, as well as Zn and S, are present in the hybrid nanobelts. The presence of N and C in the survey spectrum is due to the coordinated organic spacer molecule of en. As shown in Figure 2-5b, the binding energies of Zn $2p_{3/2}$ and Zn $2p_{1/2}$ were identified at 1019.8 and 1042.8 eV, respectively. The XPS data of Figure 2-5c yield two distinct bands by the Gaussian fitting of the S 2p, and the deconvoluted binding energies of 159.8 and 161.0 eV could be assigned to the S $2p_{3/2}$ and S $2p_{1/2}$ of a Zn–S bond, respectively. The binding energy of N 1s located at 398.4 eV in Figure 2-5d could be attributed to a Zn–N bond. These XPS results are in good agreement with those in previous reports.³⁸⁻⁴⁰ The binding energy of the Zn–N bond is considered to derive from a derivative of Zn and en such as $\text{Zn}\cdot(\text{en})_{0.5}^{2+}$. This Zn–N bond in the XPS analysis clearly indicates the existence of organic spacer molecules that are intercalated inside the ZnS structure.

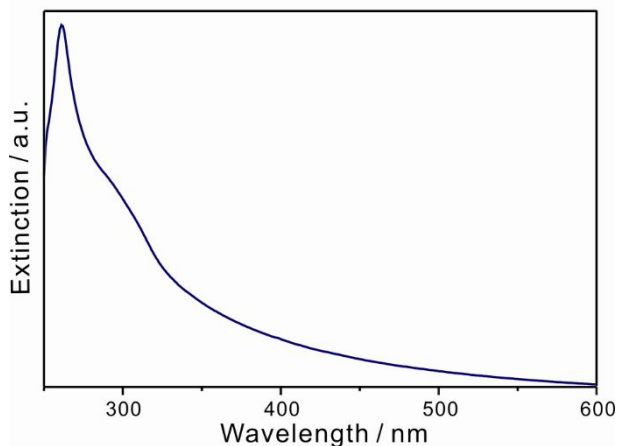
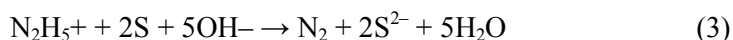
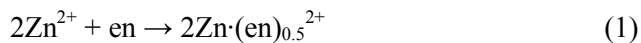


Figure 2-6. Extinction spectrum of ZnS·(en)_{0.5} nanobelts grown at 180 °C for 6 h with $V_{\text{hm}}/V_{\text{en}}$ of 3. Nanobelts were suspended in water.

In addition, the extinction spectrum of Figure 2-6 shows a sharp absorption peak at 262 nm, which corresponds to 4.73 eV. The peak is largely blue-shifted compared with the absorption peak of bulk ZnS at 335 nm.^{19,45} This drastically blue-shifted extinction peak of the ZnS·(en)_{0.5} hybrid nanobelts is due to the characteristics of inorganic-organic hybrid nanomaterials.^{26,41} Considering the HRXRD patterns of Figure 2-3, the XPS spectra of Figure 2-5, and the extinction spectrum of Figure 2-6, as-synthesized products have the inorganic-organic hybrid nanostructures of ZnS·(en)_{0.5}. The formation mechanism of ZnS·(en)_{0.5} hybrid nanobelts can be proposed as follows. An ethylenediamine (en) molecule provides a pair of binding sites for a Zn²⁺ ion to produce a chemically stable complex of Zn·(en)_{0.5}²⁺ (eq 1). Hydrazine monohydrate (hm) acts as a strong reducing agent of sulfur to form a sulfide ion (S²⁻); elemental sulfur powder is soluble

in hm and a hydrazinium (N_2H_5^+) ion can reduce sulfur to a sulfide ion (eqs 2 and 3). The reduced sulfide ion would react with $\text{Zn}\cdot(\text{en})_{0.5}^{2+}$ to form $\text{ZnS}\cdot(\text{en})_{0.5}$ (eq 4).^{26-28, 34,35} The overall reactions can be expressed as follows:



The complexing reagent of en, which contains a pair of chelating N atoms in each molecule, possibly combines with Zn^{2+} and S^{2-} in a line owing to its linear structure. On the other hand, a sufficient amount of hm, a large value of $V_{\text{hm}}/V_{\text{en}}$, facilitates the formation of active S^{2-} through an interfacial process, providing a large quantity of excess S^{2-} ions in the reaction mixture. This is believed to be the driving force for the efficient growth of one-dimensional $\text{ZnS}\cdot(\text{en})_{0.5}$ hybrid nanobelts. It has been reported that if a reaction with two precursors is employed to synthesize semiconductor nanostructures, an excess of the relatively less reactive precursor generates elongated nanostructures with higher aspect ratios.⁴² In this experiment, a large excess of S^{2-} provided from the reduction of S by hm at a large value of $V_{\text{hm}}/V_{\text{en}}$ is the kinetic driving force for the anisotropic one-dimensional growth of $\text{ZnS}\cdot(\text{en})_{0.5}$ hybrid nanostructures.

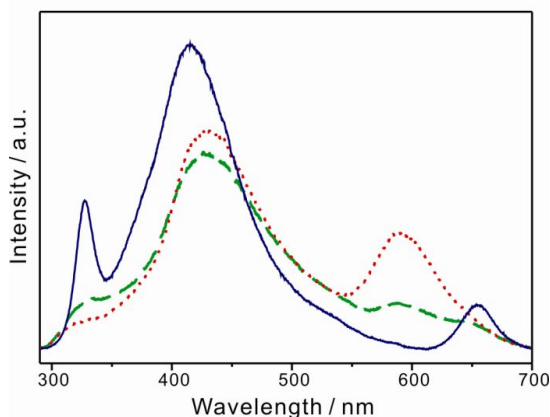


Figure 2-7. Photoluminescence spectra of $\text{ZnS}\cdot(\text{en})_{0.5}$ nanostructures grown at $180\text{ }^{\circ}\text{C}$ for 6 h with $V_{\text{hm}}/V_{\text{en}}$ of 3 (solid), 1 (dashed), and 0.5 (dotted). The nanostructures were suspended in water and excited with 266 nm laser pulses of 6 ns.

The comparative study of the optical properties of nanostructures is helpful to evaluate the quality of product materials and can shed light on their potential applications. The photoluminescence spectra of Figure 2-7, as well as the extinction spectrum of Figure 2-6, show that $\text{ZnS}\cdot(\text{en})_{0.5}$ hybrid nanostructures have different optical features compared with not only bulk ZnS but also bare-ZnS nanobelts, due to the characteristics of inorganic-organic hybrid nanomaterials.^{20,26,41,43} Room-temperature photoluminescence spectra of $\text{ZnS}\cdot(\text{en})_{0.5}$ hybrid nanostructures are shown in Figure 2-7. Each of the curves exhibits three bands located at 327, 415–430, and 587–654 nm, which can be assigned to UV, blue, and orange emission bands, respectively. The first UV emission band located at 327 nm should be attributed to the band-edge emission of $\text{ZnS}\cdot(\text{en})_{0.5}$ hybrid nanostructures. Although the large exciton-binding energy (40 meV) is much higher than thermal energy at room

temperature (about 25 meV), the band-edge emission can be observed only in very high-quality single nanocrystals at room temperature.⁴⁴ Thus, the observed band-edge emission indicates that ZnS·(en)_{0.5} hybrid nanobelts synthesized with $V_{\text{hm}}/V_{\text{en}}$ of 3 are highly crystalline. This is consistent with the results discussed with the HRTEM image and the FFT pattern of Figure 2-2a. This strong band-edge emission has been hardly reported for ZnS nanobelts synthesized *via* solution approaches.^{10,45} The second blue emission band centered at 415–430 nm, originating from trap sites or surface states,^{41,46,47} shifts gradually to the blue by 15 nm with the increase of $V_{\text{hm}}/V_{\text{en}}$. This blue shift has been attributed to enhanced quantum confinement due to the decreased average crystallite size²¹ of ZnS·(en)_{0.5} hybrid nanostructures with the increment of $V_{\text{hm}}/V_{\text{en}}$, as discussed with Figure 2-3b. The photoluminescence intensity of ZnS·(en)_{0.5} hybrid nanobelts synthesized with $V_{\text{hm}}/V_{\text{en}}$ of 3 is stronger by 50% than that of ZnS·(en)_{0.5} hybrid nanosheets synthesized with $V_{\text{hm}}/V_{\text{en}}$ of 0.5 or 1. This intensity increase has been ascribed to the decrease of defect sites owing to crystallinity increase as discussed with Figure 2-2, as well as the decrease of surface states due to aspect ratios increase as shown in Figure 2-1, with the increase of $V_{\text{hm}}/V_{\text{en}}$. The last orange emission band centered at 587–654 nm has been attributed to arise from two kinds of anion (sulfide) vacancies capturing two electron (F-centers) or one electron (F⁺-centers).⁴⁸ Figure 2-8 shows that the orange emission band can be deconvoluted into an emission band of F⁺-centers at 586–591 nm and an emission band of F-centers at 654–655 nm. The contribution of the orange

emission in total photoluminescence decreases significantly with the increase of $V_{\text{hm}}/V_{\text{en}}$. This has also been ascribed to the decrease of defect sites due to crystallinity increase with the increment of $V_{\text{hm}}/V_{\text{en}}$ as discussed with Figure 2-2. Because hm acts as a strong reducing agent of S to form S^{2-} (see above), the amount of defect sites, which are anion vacancies, decreases with the increment of $V_{\text{hm}}/V_{\text{en}}$.

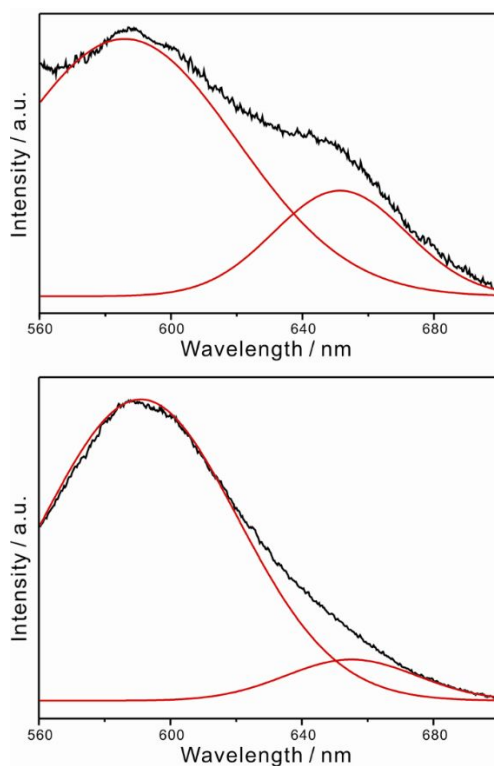


Figure 2-8. Gaussian functions (red) deconvoluted from the photoluminescence spectra (black) of $\text{ZnS}(\text{en})_{0.5}$ nanostructures grown at $180\text{ }^\circ\text{C}$ for 6 h with $V_{\text{hm}}/V_{\text{en}}$ of 1 (top) and 0.5 (bottom).

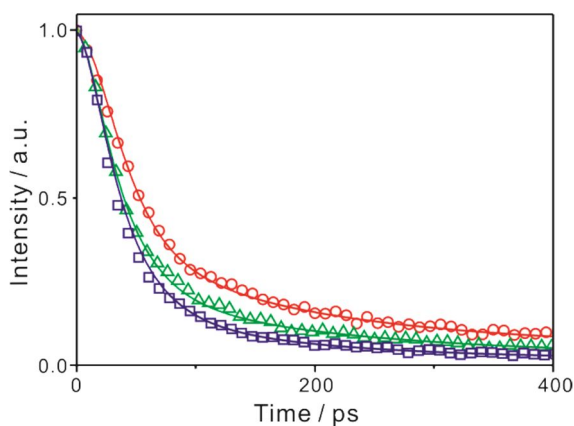


Figure 2-9. Maximum-normalized photoluminescence decay kinetic profiles of ZnS·(en)_{0.5} nanostructures grown at 180 °C for 6 h with V_{hm}/V_{en} of 3 (squares), 1 (triangles), and 0.5 (circles) suspended in water. Photoluminescence was monitored at 450 nm after excitation with 266 nm pulses of 25 ps. Solid lines are the best-fitted curves to extract lifetimes given in Table 1.

Table 2-1. Photoluminescence Decay Kinetic Constants of ZnS·(en)_{0.5} Nanostructures Suspended in Water^a

V_{hm}/V_{en}	lifetime / ps	mean lifetime / ps
3.0	30 (91.5%) + 170 (7.5%) + 2700 (1.0%) ^b	67
1.0	30 (87.0%) + 170 (11.0%) + 2700 (2.0%)	99
0.5	30 (82.7%) + 170 (14.5%) + 2700 (2.8%)	125

^a Deconvoluted from the kinetic profiles of Figure 2-9. ^b Initial intensity percentage of each component.

Figure 2-9 and Table 2-1 indicate that the photoluminescence kinetic profiles of ZnS·(en)_{0.5} hybrid nanostructures look similar to one another with having three decay components although their mean emission lifetime

decreases with the increase of $V_{\text{hm}}/V_{\text{en}}$. The decrease of the mean emission lifetime with the increment of $V_{\text{hm}}/V_{\text{en}}$ is considered to associate with the decrease of defect sites or surface states as described with Figure 2-7. The fast decay time of 30 ps is considered to be the trapping time of electrons in the conduction band of $\text{ZnS} \cdot (\text{en})_{0.5}$ hybrid nanostructures while the medium decay time of 170 ps is attributed to the relaxation time of electrons at trap sites *via* being trapped into surface states. The slow decay time of 2700 ps has been assigned to the hole recombination time of electrons at surface states. While the decreasing amplitude of the medium decay component with the increase of $V_{\text{hm}}/V_{\text{en}}$ can be attributed to the decrease of defect sites owing to crystallinity increase as discussed with Figure 2-2, the amplitude decrease of the slow component is ascribed to the decrease of surface states due to size increase with $V_{\text{hm}}/V_{\text{en}}$ as shown in Figure 2-1.

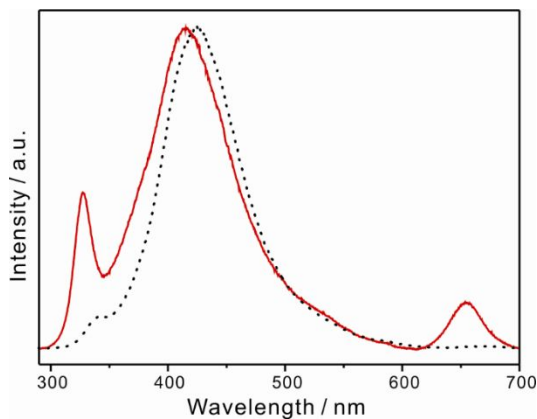


Figure 2-10. Maximum-normalized photoluminescence spectra of $\text{ZnS} \cdot (\text{en})_{0.5}$ nanobelts grown at 180 °C for 6 h with $V_{\text{hm}}/V_{\text{en}}$ of 3 (solid) and bare-ZnS nanobelts fabricated by removing organic molecules from the $\text{ZnS} \cdot (\text{en})_{0.5}$ nanobelts (dotted). Nanostructures were suspended in water and excited at 266 nm.

The decay profile of the orange emission band at 584–654 nm has been found to be too slow to be observed with our picosecond kinetic spectrometer because radiative transition from the relaxed excited state (2s) to the ground state (1s) of F-centers is not allowed by the spectroscopic selection rule of Laporte. Figure 2-10 suggests that the photoluminescence spectrum of removed bare-ZnS nanobelts is substantially different from that of $\text{ZnS}\cdot(\text{en})_{0.5}$ hybrid nanobelts. While hydrothermal treatment has reduced UV band-edge emission substantially, it has removed orange F-center emission drastically. Figure 2-10 also shows that hydrothermal treatment shifts both the UV and the blue emission bands of $\text{ZnS}\cdot(\text{en})_{0.5}$ hybrid nanobelts to the red by 8 nm. This suggests that the band gap of $\text{ZnS}\cdot(\text{en})_{0.5}$ hybrid nanobelts is higher than that of bare-ZnS nanobelts. Compared with bare-ZnS nanobelts, $\text{ZnS}\cdot(\text{en})_{0.5}$ hybrid nanobelts have shown enhanced optical properties that would give them potential for nanoscale optoelectronic devices.

2. 5. Conclusion

Flexible and well-defined $\text{ZnS}\cdot(\text{en})_{0.5}$ (en = ethylenediamine) hybrid nanobelts with high aspect ratios have been facilely synthesized by a template-free and one-pot solvothermal process. The appearance structures, crystallite sizes, and optical properties of $\text{ZnS}\cdot(\text{en})_{0.5}$ hybrid nanostructures can be tuned by modifying the volume ratio ($V_{\text{hm}}/V_{\text{en}}$) of hydrazine monohydrate (hm) to en. Hybrid nanobelts having single-domain crystallites have been synthesized with $V_{\text{hm}}/V_{\text{en}}$ of 3 while hybrid nanosheets having multi-domain crystallites have been synthesized with $V_{\text{hm}}/V_{\text{en}}$ of 0.5 or 1. A reaction time as long as 6 h has been found to be essential for the growth of highly crystalline $\text{ZnS}\cdot(\text{en})_{0.5}$ hybrid nanobelts. A sufficient amount of hm, i.e. a large value of $V_{\text{hm}}/V_{\text{en}}$, facilitates the abundant formation of active S^{2-} through an interfacial process, suggesting that a large quantity of excess S^{2-} ions in the reaction mixture is the driving force for the efficient growth of anisotropic one-dimensional $\text{ZnS}\cdot(\text{en})_{0.5}$ hybrid nanobelts. $\text{ZnS}\cdot(\text{en})_{0.5}$ hybrid nanostructures exhibit three emission bands: band-edge emission at 327 nm, trap sites-related emission at 415–430 nm, and anion (sulfide)-vacancy emission at 584–654 nm. The spectral properties of three bands are affected by the crystallinity and size of $\text{ZnS}\cdot(\text{en})_{0.5}$ hybrid nanostructures, which can be varied by adjusting $V_{\text{hm}}/V_{\text{en}}$. The mean lifetime of photoluminescence having three decay components of 30, 170, and 2700 ps decreases with $V_{\text{hm}}/V_{\text{en}}$ due to the decrease of defect sites with the increase of the aspect ratios

of ZnS·(en)_{0.5} hybrid nanobelts. The organic molecules of ZnS·(en)_{0.5} hybrid nanobelts can be removed *via* a relatively mild hydrothermal treatment process to fabricate bare-ZnS nanobelts.

2. 6. Acknowledgements

This work was supported by the National Research Foundation of Korea grant funded by the Korea government (MEST) (2011-0028981 and 2007–0056331).

2. 7. References

- (1) Z. W. Pan, Z. R. Dai and Z. L. Wang, *Science*, **2001**, *291*, 1947.
- (2) B. Liu, Y. Bando, X. Jiang, C. Li, X. Fang, H. Zeng, T. Terao, C. Tang, M. Mitome and D. Golberg, *Nanotechnology*, **2010**, *21*, 375601.
- (3) Y. Che, A. Datar, K. Balakrishnan and L. Zang, *J. Am. Chem. Soc.*, **2007**, *129*, 7234.
- (4) J.-Y. Kim, S. J. Kim and D.-J. Jang, *J. Phys. Chem. C*, **2011**, *115*, 672.
- (5) J. Joo, J. S. Son, S. G. Kwon, J. H. Yu and T. Hyeon, *J. Am. Chem. Soc.*, **2006**, *128*, 5632.
- (6) J.-Y. Kim, H. Jeong and D.-J. Jang, *J. Nanopart. Res.*, **2011**, *13*, 6699.
- (7) L. Yin and Y. Bando, *Nat. Mater.*, **2005**, *4*, 883.

- (8) J. Gong, S. Yang, J. Duan, R. Zhang and Y. Du, *Chem. Commun.*, **2005**, 351.
- (9) Y. Che, A. Datar, X. Yang, T. Naddo, J. Zhao and L. Zang, *J. Am. Chem. Soc.*, **2007**, *129*, 6354.
- (10) R. Chen, D. Li, B. Liu, Z. Peng, G. G. Gurzadyan, Q. Xiong and H. Sun, *Nano. Lett.*, **2010**, *10*, 4956.
- (11) U. K. Gautam, X. Fang, Y. Bando, J. Zhan and D. Golberg, *ACS Nano*, **2008**, *2*, 1015.
- (12) Y. F. Nicolau, M. Dupuy and M. Brunel, *J. Electrochem. Soc.*, **1990**, *137*, 2915.
- (13) H. Fujiwara, H. Hosokawa, K. Murakoshi, Y. Wada and S. Yanagida, *Langmuir*, **1998**, *14*, 5154.
- (14) H. Yin, Y. Wada, T. Kitamura and S. Yanagida, *Environ. Sci. Technol.*, **2001**, *35*, 227.
- (15) D. F. Moore, Y. Ding and Z. L. Wang, *J. Am. Chem. Soc.*, **2004**, *126*, 14372.
- (16) T. Zhai, Z. Gu, Y. Ma, W. Yang, L. Zhao and J. Yao, *Mater. Chem. Phys.*, **2006**, *100*, 281.
- (17) X.-J. Xu, G.-T. Fei, W.-H. Yu, X.-W. Wang, L. Chen and L.-D. Zhang, *Nanotechnology*, **2006**, *17*, 426.
- (18) C. Ma, D. Moore, J. Li and Z. L. Wang, *Adv. Mater.*, **2003**, *15*, 228.
- (19) L. Chai, J. Du, S. Xiong, H. Li, Y. Zhu and Y. Qian, *J. Phys. Chem. C*, **2007**, *111*, 12658.
- (20) W.-T. Yao, S.-H. Yu, L. Pan, J. Li, Q.-S. Wu, L. Zhang and J. Jiang, *Small*, **2005**, *1*, 320.

- (21) J.-Y. Kim, M. R. Kim, S.-Y. Park and D.-J. Jang, *CrystEngComm*, **2010**, *12*, 1803.
- (22) X. Huang and J. Li, *J. Am. Chem. Soc.*, **2000**, *122*, 8789.
- (23) W. Yao, S.-H. Yu, X. Huang, J. Jiang, L. Q. Zhao, L. Pan and J. Li, *Adv. Mater.*, **2005**, *17*, 2799.
- (24) Z.-X. Deng, L. Li and Y. Li, *Inorg. Chem.*, **2003**, *42*, 2331.
- (25) L. Zhang, H. Yang, L. Li, R. Zhang, R. Liu, J. Ma, X. Xie and F. Gao, *Inorg. Chem.*, **2008**, *47*, 11950.
- (26) S.-H. Yu and M. Yoshimura, *Adv. Mater.*, **2002**, *14*, 296.
- (27) G. Xi, C. Wang, X. Wang, Q. Zhang and H. Xiao, *J. Phys. Chem. C*, **2008**, *112*, 1946.
- (28) Y. Ni, X. Cao, G. Hu, Z. Yang, X. Wei, Y. Chen and J. Xu, *Cryst. Growth Des.*, **2007**, *7*, 280.
- (29) R. Mosca, P. Ferro, D. Calestani, L. Nasi, T. Besagni and F. Licci, *Cryst. Res. Technol.*, **2011**, *46*, 818.
- (30) Y. Li, H. Liao, Y. Ding, Y. Fan, Y. Zhang and Y. Qian, *Inorg. Chem.*, **1999**, *38*, 1382.
- (31) X. Ouyang, T.-Y. Tsai, D.-H. Chen, Q.-J. Huang, W.-H. Cheng and A. Clearfield, *Chem. Commun.*, **2003**, 886.
- (32) C. Dong, *J. Appl. Cryst.*, **1999**, *32*, 838.
- (33) G.-T. Zhao, X. Wang and J. C. Yu, *Cryst. Growth Des.*, **2005**, *5*, 1761.
- (34) Y. Li, Y. Ding and Z. Wang, *Adv. Mater.*, **1999**, *11*, 847.
- (35) L. Shi, Y. Xu and Q. Li, *Cryst. Growth Des.*, **2009**, *9*, 2214.

- (36) R. J. Bandaranayake,; G. W. Wen, L. Y. Lin, H. X. Jiang and C. M. Sorensen, *Appl. Phys. Lett.*, **1995**, *67*, 831.
- (37) Q. Xiong, J. Wang, O. Reese, L. C. L. Y. Voon and P. C. Eklund, *Nano Lett.*, **2004**, *4*, 1991.
- (38) M. Ahmad, X. Yan and J. Zhu, *J. Phys. Chem. C*, **2011**, *115*, 1831.
- (39) D.-P. Kim, C.-I. Kim and K.-H. Kwon, *Thin Solid Films*, **2004**, *459*, 131.
- (40) P. Cao, D. X. Zhao, J. Y. Zhang, D. Z. Shen, Y. M. Lu, B. Yao, B. H. Li, Y. Bai and X. W. Fan, *Appl. Surf. Sci.*, **2008**, *254*, 2900.
- (41) S.-H. Yu, J. Yang, Y.-T. Qian and M. Yoshimura, *Chem. Phys. Lett.*, **2002**, *361*, 362.
- (42) X. Peng, *Adv. Mater.*, **2003**, *15*, 459.
- (43) X. Huang, J. Li, Y. Zhang and A. Mascarenhas, *J. Am. Chem. Soc.*, **2003**, *125*, 7049.
- (44) T. K. Tran, W. Park, W. Tong, M. M. Kyi, B. K. Wagner, C. J. Summers, *J. Appl. Phys.*, **1997**, *81*, 2803.
- (45) X. Fang, Y. Bando, M. Liao, U. K. Gautam, C. Zhi, B. Dierre, B. Liu, T. Zhai, T. Sekiguchi, Y. Koide and D. Golberg, *Adv. Mater.*, **2009**, *21*, 2034.
- (46) Y.-C. Zhu, Y. Bando and D.-F. Xue, *Appl. Phys. Lett.*, **2003**, *82*, 1769.
- (47) D. Denzler, M. Olschewski and K. Sattler, *J. Appl. Phys.*, **1998**, *84*, 2841.
- (48) A. H. Harker, *J. Phys. C*, **1978**, *11*, 1059.

Chapter 3. Fabrication and Growth-Mechanism of Single-Crystalline ZnS Nanobelts

Part 3A. Facile one-step hydrothermal fabrication of single-crystalline ZnS nanobelts with narrow band-edge luminescence

3A. 1. Abstract

Single-crystalline wurtzite ZnS nanobelts exhibiting enhanced narrow band-edge luminescence at room temperature have been synthesized readily through a one-step mild hydrothermal process involving ternary solvents of hydrazine, ethylenediamine, and water.

[†]This is reproduced from Yeonho Kim and Du-Jeon Jang, *RSC Adv.* **2013**, *3*, 16945. © 2013 Royal Society of Chemistry.

3A. 2. Introduction

ZnS is a well-known direct band gap II-VI semiconductor, and it attracts intense interest due to its excellent properties of luminescence which enable ZnS to be promising materials for optical, photonic, and electronic devices.¹⁻³ Among the nanoscale structures of ZnS, in particular, one-dimensional (1-D) nanostructures are highly attractive building blocks for nanodevices due to their inherent anisotropies and efficient transport of electrons and excitons through their longitudinal direction.⁴⁻⁶ From the viewpoint of applications, synthetic protocols for 1-D ZnS nanostructures with controlled shapes and optical properties are greatly demanded and have been the current focus of research.

Despite recent achievements for the synthetic processes of one-dimensional ZnS nanostructures showing ultraviolet luminescence, mild solution synthetic methods via a facile one-step process are still challenging. Many researchers have focused on the development of synthetic protocols for nanoscaled 1-D wurtzite ZnS with controlled morphologies and optical properties. For instance, a molecular template of ethylenediamine (en) has been used generally for the synthesis of wurtzite ZnS nanocrystals. However, it often binds with Zn and S to form inorganic-organic hybrid nanostructures of $\text{ZnS}\cdot(\text{en})_{0.5}$. Wurtzite ZnS nanocrystals could be prepared via decomposing $\text{ZnS}\cdot(\text{en})_{0.5}$ nanostructures in a vacuum or solution at a relatively high temperature; the molecular precursor of en plays an important role as a

solvent-coordinating molecular template for the formation of wurtzite ZnS nanostructures.⁷⁻⁹ However, all of the reported works have involved a two-step synthetic route: the synthesis of ZnS·(en)_{0.5} nanostructures and their subsequent treatment to produce wurtzite ZnS nanocrystals. As to the one-step synthesis of semiconducting metal-sulfide nanocrystals in a solution, some important progresses have been made. In particular, the one-step solvothermal synthesis of wurtzite ZnS nanocrystals has been achieved in mixed solvents.^{10,11} However, nanostructured ZnS materials prepared via these kinds of wet chemical routes have often been found to have a sphere-like morphology capped with long carbon-chain ligands, showing the band-edge emission hardly.

In this study, we report a facile one-step hydrothermal process to fabricate single-crystalline wurtzite ZnS nanobelts showing narrow band-edge emission. Each of our fabricated ZnS nanobelts has been found to be chemically pure, structurally uniform, single-crystalline, and defect-free. These features suppress emission from trap or surface states to bring about a highly narrow band-edge luminescence at room temperature. Water, introduced as one of ternary mixed solvents, effectively eliminates en molecules intercalated in ZnS layers to make the entire synthetic route completed in one step without requiring any post treatment.

3A. 3. Experimental Details

Synthesis. The analytical grade chemicals of $\text{N}_2\text{H}_4\cdot\text{H}_2\text{O}(\text{l})$, $\text{C}_2\text{H}_4(\text{NH}_2)_2(\text{l})$, $\text{ZnCl}_2(\text{s})$, and $\text{S}(\text{s})$ were used as purchased from Sigma-Aldrich. Deionized (DI) water with a resistivity of greater than $18 \text{ M}\Omega \text{ cm}$, from a Millipore Milli-Q system, was used throughout the experiments. For the typical preparation of single-crystalline wurtzite ZnS nanobelts, 7.5 mL of $\text{C}_2\text{H}_4(\text{NH}_2)_2$, 7.5 mL of DI water, 15 mL of $\text{N}_2\text{H}_4\cdot\text{H}_2\text{O}$, 0.5 mmol of ZnCl_2 , and 0.5 mmol of S were stirred vigorously for 30 min. The mixture solution was then loaded into a Teflon-lined stainless-steel autoclave of 50 mL capacity, placed in a preheated oven at 180°C for 6 h, and cooled to room temperature. A white precipitate produced in the reaction mixture was washed several times using DI water and ethanol separately, vacuum-dried, and kept for further characterization.

Characterization. While transmission electron microscopy (TEM) images were obtained with a JEOL JEM-2100 microscope, high-resolution TEM (HRTEM) images and fast Fourier transformation (FFT) patterns were measured using a JEOL JEM-3010 microscope. While scanning electron microscopy (SEM) images were recorded with a JEOL JSM-6700F microscope, high-angle annular dark-field scanning TEM (HAADF-STEM) images and energy-dispersive X-ray (EDX) line-scanned elemental intensity profiles were measured using an FEI Tecnai F20 microscope. High-resolution

X-ray diffraction (HRXRD) patterns were obtained with a Bruker D8 DISCOVER diffractometer using Cu K α radiation (0.15418 nm), and X-ray photoelectron spectroscopy (XPS) spectra were monitored using a Kratos AXIS-HSi spectrometer with an excitation source of Mg K α (1253.60 eV). Extinction spectra were obtained with a Scinco S3100 UV/vis spectrophotometer, and photoluminescence spectra were measured employing a Princeton Instruments ICCD576G CCD detector with excitation using 266 nm pulses from a Q-switched Quantel Brilliant Nd:YAG laser of 6 ns.

3A. 4. Results and Discussion

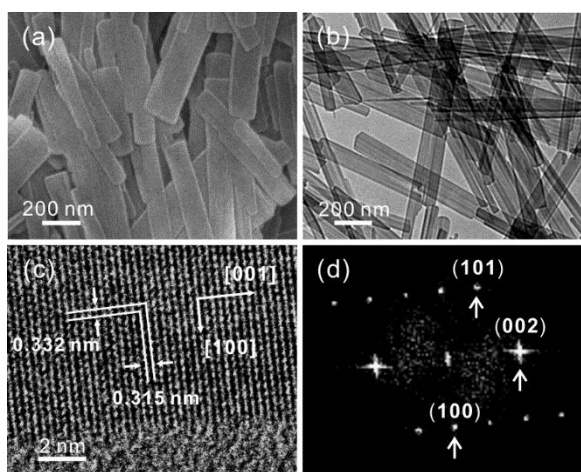


Figure 3A-1. SEM (a) and TEM (b) images of ZnS nanobelts and HRTEM image (c) and FFT pattern (d) of a ZnS nanobelt.

Both the scanning electron microscopy (SEM) image of Figure 3A-1a and the transmission electron microscopy (TEM) image of Figure 3A-1b indicate that as-synthesized nanobelts have uniform cross sections along

their lengths, with a mean width of 80 ± 9 nm and a typical thickness of 16 ± 3 nm, and an average length of 990 ± 50 nm have been readily synthesized in large quantities via a one-step mild hydrothermal process. The nanobelts of long rectangular prisms have flat and smooth surfaces and well-defined edges. The energy-dispersive X-ray (EDX) profile of Figure 3A-2 reveals that the elemental components of the nanobelts are Zn and S indeed and that the atomic molar ratio of Zn:S is 1:1.01, which agrees very well with the stoichiometric composition of ZnS. The latter implies that the surfaces of the nanobelts are free of dangling bonds, probably giving birth to both the perfect-crystalline structure and the narrow band-edge emission of ZnS (see below).

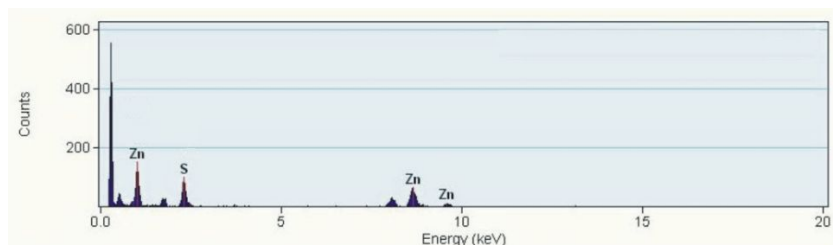


Figure 3A-2. EDX profile of ZnS nanobelts showing the atomic molar ratio of Zn:S to be 1:1.01, very close to the stoichiometric ratio of ZnS.

In general, high-resolution TEM (HRTEM) images and fast Fourier transformation (FFT) patterns can provide deep insights into the structural properties of nanomaterials at the atomic level. The representative HRTEM images of Figure 3A-1c and Figure 3A-3 show that a ZnS nanobelt is structurally uniform without having any obvious defects such

as dislocations or stacking faults. Moreover, the clearly discernible lattice fringes of Figure 3A-1c verify that the as-synthesized nanobelt is highly single-crystalline. The marked lattice fringe distances of 0.315 nm and 0.332 nm agree reasonably well with the standard spacings of 0.313 nm between the (002) lattice planes and 0.331 nm between the (100) lattice planes, respectively, of the wurtzite ZnS, indicating that the ZnS nanobelt grows along the directions of [001] and [100].

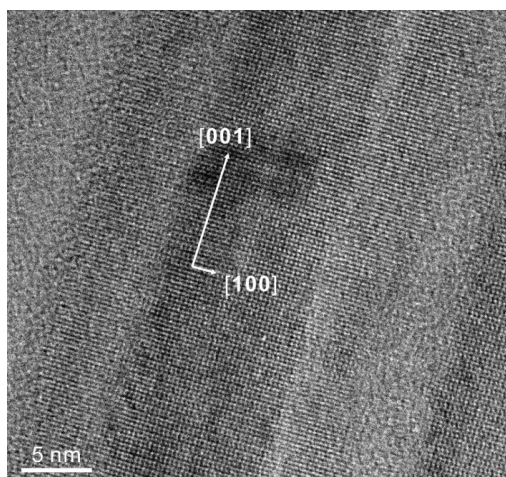


Figure 3A-3. HRTEM image of a ZnS nanobelt.

The final shape of a nanocrystal could be determined by the relative surface energies of crystallographic planes and the relative rates of growth directions. The surface energies (γ) of different crystallographic planes hold a general sequence as $\gamma_{(110)} < \gamma_{(100)} < \gamma_{(002)}$ in the wurtzite ZnS.¹² Figure 3A-1d shows that the diffraction intensity of (002) surpasses those of any other planes, illustrating that the wurtzite ZnS nanobelt has a

significantly preferred orientation to the direction of [001]. Figure 3A-3 also indicates that our ZnS nanobelt has grown preferentially along the [001] direction rather than the [100] direction. The average spacing values calculated from the FFT diffraction spots in Figure 3A-1d can be readily indexed to the standard values of the wurtzite ZnS, also supporting that the ZnS nanobelt is a well-defined single crystal. The EDX line-scanned elemental intensity profiles of a ZnS nanobelt in Figure 3A-4 reveal that the elements of Zn and S are evenly distributed and that the relative intensities of Zn and S match very well with their relative compositions of the reference ZnS. The elemental intensity profiles of Figure 3A-4 also support that the cross section of the ZnS nanobelt is rectangular.

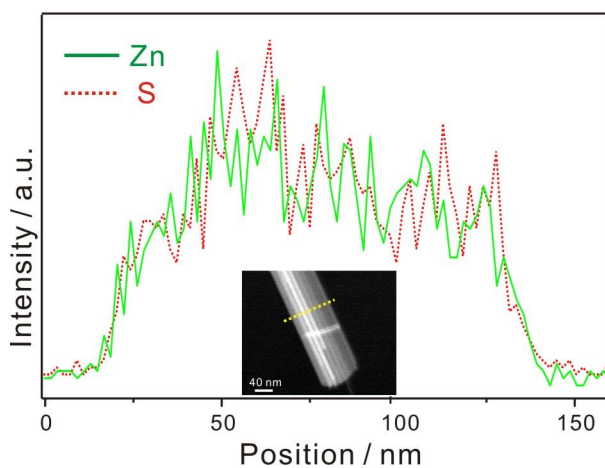


Figure 3A-4. EDX line-scanned profiles, measured along the indicated dashed line of the insetted HAADF-STEM image.

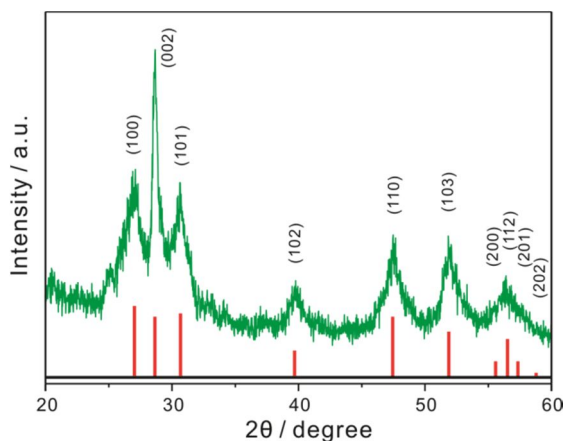


Figure 3A-5. HRXRD patterns of ZnS nanobelts. The bottom pattern is from the reference wurtzite ZnS (JCPDS Card No. 36-1450).

Figure 3A-5 shows that the high-resolution X-ray diffraction (HRXRD) pattern of the ZnS nanobelts agrees well with the standard pattern of the reference wurtzite ZnS. However, the diffraction peak at 2θ of 28.5° , indexed as the (002) plane, surpasses diffraction peaks arising from any other planes, supporting that the ZnS nanobelts have grown preferentially to the direction of [001] as discussed with Figure 3A-1. The mean crystallite diameter of wurtzite ZnS nanobelts, estimated with the peak at 2θ of 28.5° using the Scherrer's formula,¹³ is 21 nm, which is comparable to the typical thickness of 15 nm. Figure 3A-5 also shows that the diffraction intensity of the (002) plane is predominant among the HRXRD peaks of ZnS nanobelts, illustrating their *c*-axis oriented crystal growth nature. The degree of orientation can be illustrated by the relative texture coefficient of TC_{002} , which is the relative intensity of the (002) diffraction

peak over that of the (100) diffraction peak.¹⁴ Although the TC_{002} of ZnS materials with random crystallographic orientation is 0.5, the TC_{002} of our ZnS nanobelts has been measured to be 0.67. The large TC_{002} value, together with the results described with Figure 3A-1d and 3A-3, makes clear that our fabricated wurtzite ZnS nanobelts have a preferred growth orientation to the [001] direction.

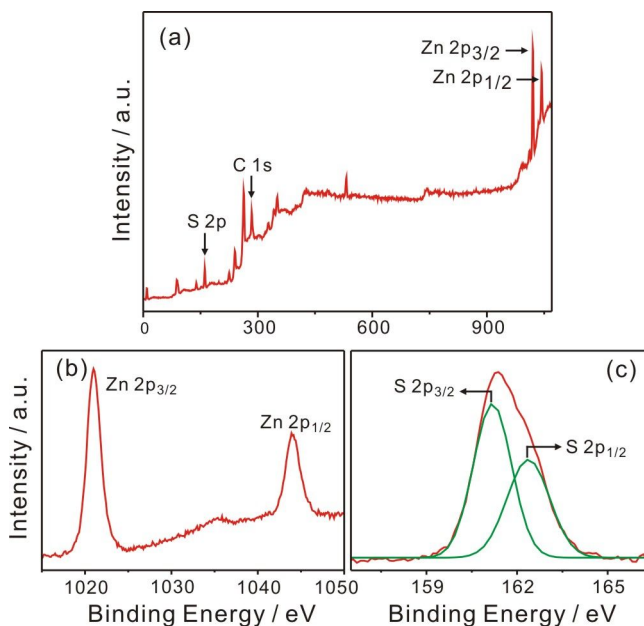


Figure 3A-6. Complete survey (a), Zn 2p (b), and S 2p (c) XPS spectra of ZnS nanobelts. Two green curves in c have been deconvoluted from the Gaussian fitting.

The X-ray photoelectron spectroscopy (XPS) data of Figure 3A-6 can provide further significant information about the surface composition of the ZnS nanobelts. The binding energies obtained in the XPS analysis were corrected for specimen charging, through referencing the C 1s to 284.6 eV.

The survey spectrum of Figure 3A-6a shows that Zn and S are present in the nanobelts. The peak energies of 1020.9 and 1044.1 eV in Figure 3A-6b have been identified as the binding energies of the Zn 2p_{3/2} and the Zn 2p_{1/2} of ZnS, respectively. The XPS spectrum of Figure 3A-6c can be deconvoluted into two Gaussian bands, whose energies of 161.1 and 162.4 eV have been assigned to the binding energies of the S 2p_{3/2} and the S 2p_{1/2} of ZnS, respectively.^{15,16}

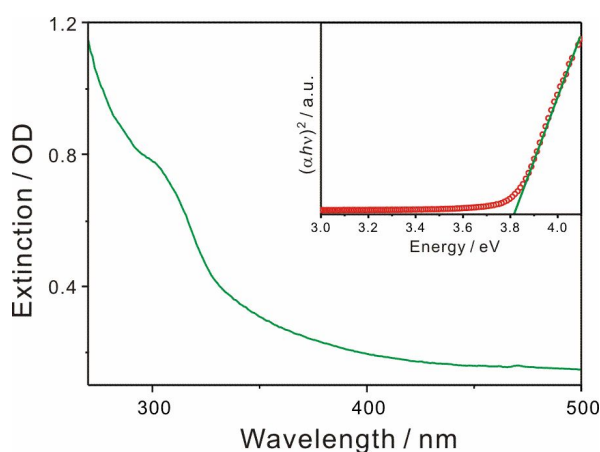


Figure 3A-7. Extinction spectrum of ZnS nanobelts suspended in ethanol. The inset shows the $(\alpha h\nu)^2$ plot against $(h\nu)$ of the extinction spectrum after removing scattering, where α is the absorption coefficient and the solid line shows the best linear fit to estimate the band-gap energy.

The extinction spectrum of Figure 3A-7 shows a discernible absorption band around 310 nm, which is one of the typical intrinsic optical features of ZnS nanomaterials.¹⁷ The extinction spectrum can be used to estimate the band gap of semiconductors as shown in the inset of Figure 3A-7. Using the modified Kubelka-Munk function,¹⁸ we have calculated the

band-gap energy of our ZnS nanobelts as 3.82 eV, which is slightly blue-shifted by 0.05 eV from that of bulk wurtzite ZnS (3.77 eV).⁴ This can be explained as the quantum size effect originated from the electron-hole confinement in a small volume; the mean crystallite diameter of our ZnS nanobelts calculated using the Brus equation¹⁹ with the absorption band-gap energy of 3.82 eV has been found to be 8.3 nm.

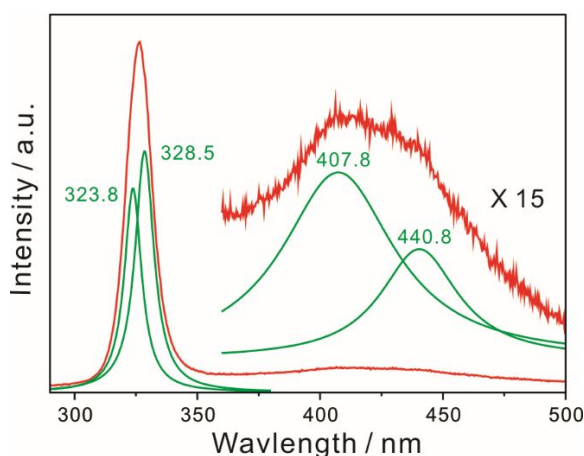


Figure 3A-8. Photoluminescence spectrum of ZnS nanobelts suspended in ethanol, taken at room temperature with excitation at 266 nm. Green curves, whose peak positions are indicated inside in the units of nanometers, are Lorentzian line shape analyses deconvoluted from the red experimental spectrum.

The room-temperature photoluminescence spectrum of ZnS nanobelts (Figure 3A-8) under an average excitation fluence of 80 mW/cm² consists of a strong ultraviolet (UV) emission band at 326.4 nm (3.799 eV) with a half width at the half maximum (HWHM) of 6.4 nm and a weak visible emission

band at 414.7 nm. These kinds of intense and narrow UV band-edge emission has not been reported yet for wurtzite ZnS nanostructures fabricated in solutions.^{17,20-22} Each band of the experimental spectrum can be fitted well with multiple Lorentzian profiles, as shown by the green curves in Figure 3A-8, which give rise to accurate peak-position values. In wurtzite ZnS, as the topmost valance band is split into three bands due to the spin-orbit coupling and the crystal-field splitting, the exciton states can be denoted as free-exciton A (FXA), B (FXB), and C (FXC); the splitting energies of FXC-FXB and FXB-FXA are 89 and 57 meV, respectively.²³ The observed energy splitting of 55 meV indicates that the deconvoluted UV emission curves at 328.5 nm (3.774 eV) and 323.8 nm (3.829 eV) arise from the radiation of FXA and FXB, respectively. The visible defect luminescence band in Figure 3A-8 has been multiplied by a factor of 15 for clarity, and it can be deconvoluted into two curves at 407.8 nm (3.040 eV) and 440.8 nm (2.813 eV), which have been attributed to emission from sulfur vacancies to the valence band and surface states, respectively.²⁰ The very weak intensity of the visible emission band indicates that trap sites and surface states are highly suppressed due to the perfect-crystalline structure of our ZnS nanobelts as discussed with Figure 3A-1c, bringing about highly narrow and intense UV band-edge luminescence at room temperature. The measured peak-intensity ratio of the UV emission band to the visible emission band is 21.5, indicating that the band-edge transition of free excitons is the major radiational pathway of our ZnS nanobelts. The band-gap energy of 3.82 eV calculated using the extinction

spectrum of Figure 3A-7 is almost the same as the UV emission band energy of 3.80 eV within experimental errors. This supports that the direct band-to-band transition is the major radiation route of the photo-excitation energy of perfect-crystalline wurtzite ZnS nanobelts.

3A. 5. Conclusion

In summary, single-crystalline wurtzite ZnS nanobelts showing intense and narrow UV band-edge luminescence have been synthesized via a facile one-step hydrothermal process for the first time. As-prepared ZnS nanobelts exhibit two emission bands at room temperature: strong band-edge UV luminescence at 326 nm with HWHM of 6 nm and weak defect-related visible luminescence at 415 nm. The UV luminescence has been deconvoluted into the emission of FXA at 3.77 eV and the emission of FXB at 3.83 eV. The calculated absorption band-gap energy of 3.82 eV and the free-excitonic emission energy of 3.80 eV are very close to each other within our experimental errors, supporting that the direct band-to-band transition is the main radiational pathway of ZnS nanobelts due to their perfect crystallinity.

3A. 6. Acknowledgements

This work was supported by research grants by the National Research Foundation of Korea (2011-0028981 and 2007-0056095).

3A. 7. References

- (1) X. Fang, Y. Bando, U. K. Gautam, T. Zhai, H. Zeng, X. Xu, M. Liao and D. Golberg, *Crit. Rev. Solid State Mater. Sci.*, **2009**, *34*, 190.
- (2) D. F. Moore, Y. Ding and Z. L. Wang, *J. Am. Chem. Soc.*, **2004**, *126*, 14372.

- (3) Y.-Y. Zhang, J.-Y. Kim, Y. Kim and D.-J. Jang, *J. Nanopart. Res.*, **2012**, *14*, 1117.
- (4) J. H. Yu, J. Joo, H. M. Park, S.-I. Baik, Y. W. Kim, S. C. Kim and T. Hyeon, *J. Am. Chem. Soc.*, **2005**, *127*, 5662.
- (5) C. J. Barrelet, Y. Wu, D. C. Bell and C. M. Lieber, *J. Am. Chem. Soc.*, **2003**, *125*, 11498.
- (6) Y. Kim, J.-Y. Kim and D.-J. Jang, *J. Phys. Chem. C*, **2012**, *116*, 10296.
- (7) L. Zhang, H. Yang, L. Li, R. Zhang, R. Liu, J. Ma, X. Xie and F. Gao, *Inorg. Chem.*, **2008**, *47*, 11950.
- (8) G.-T. Zhou, X. Wang and J. C. Yu, *Cryst. Growth Des.*, **2005**, *5*, 1761.
- (9) G. Xi, C. Wang, X. Wang, Q. Zhang and H. Xiao, *J. Phys. Chem. C*, **2008**, *112*, 1946.
- (10) J. Joo, H. B. Na, T. Yu, J. H. Yu, Y. W. Kim, F. Wu, J. Z. Zhang and T. Hyeon, *J. Am. Chem. Soc.*, **2003**, *125*, 11100.
- (11) X. Chen, H. Xu, N. Xu, F. Zhao, W. Lin, G. Lin, Y. Fu, Z. Huang, H. Wang and M. Wu, *Inorg. Chem.*, **2003**, *42*, 3100.
- (12) Z. Wang, L. L. Daemen, Y. Zhao, C. S. Zha, R. T. Downs, X. Wang, Z. L. Wang and R. J. Hemley, *Nat. Mater.*, **2005**, *4*, 922.
- (13) R. J. Bandaranayake, G. W. Wen, J. Y. Lin, H. X. Jiang and C. M. Sorensen, *Appl. Phys. Lett.*, **1995**, *67*, 831.
- (14) H. Yang, Y. Song, L. Li, J. Ma, D. Chen, S. Mai and H. Zhao, *Cryst. Growth Des.*, **2008**, *8*, 1039.
- (15) D. Zhang, L. Luo, Q. Liao, H. Wang, H. Fu and J. Yao, *J. Phys. Chem. C*, **2011**, *115*, 2360.

- (16) J. F. Xu, W. Ji, J. Y. Lin, S. H. Tang and Y. W. Du, *Appl. Phys. A*, **1998**, 66, 639.
- (17) L. Chai, J. Du, S. Xiong, H. Li, Y. Zhu and Y. Qian, *J. Phys. Chem. C*, **2007**, 111, 12658.
- (18) L. Li, Y.-W. Yang, G.-H. Li and L.-D. Zhang, *Small*, **2006**, 2, 548.
- (19) L. E. Brus, *J. Chem. Phys.*, **1984**, 80, 4403.
- (20) S. I. Ahn, *Chem. Phys. Lett.*, **2012**, 528, 49.
- (21) Y.-C. Zhu, Y. Bando and D.-F. Xue, *Appl. Phys. Lett.*, **2003**, 82, 1769.
- (22) Nannan Jiang, R. Wu, J. Li, Y. F. Sun and J. K. Jian, *J. Alloys Comp.*, **2012**, 536, 85.
- (23) Q. Xiong, G. Chen, J. D. Acrod, X. Liu, J. J. Zengel, H. R. Gutierrez, J. M. Redwing, L. C. Lew Yan Voon, B. Lassen and P. C. Eklund, *Nano Lett.*, **2004**, 4, 1663.

Part 3B. Facile-Growth Mechanism of Wurtzite ZnS Nanostructures Showing Intense Ultraviolet Luminescence

3B. 1. Abstract

Despite recent achievements for the synthetic processes of wurtzite ZnS nanostructures via the post thermal decomposition of $\text{ZnS}\cdot(\text{en})_{0.5}$ (en = ethylenediamine) nanocomposites, investigation into the growth mechanism of wurtzite ZnS from $\text{ZnS}\cdot(\text{en})_{0.5}$ is still challenging. Diverse methods such as transmission electron microscopy, X-ray diffraction, thermal gravimetric analysis, X-ray photoelectron spectroscopy, and Fourier-transform infrared spectroscopy have been employed to understand the facile-growth mechanism of wurtzite ZnS nanobelts showing intense ultraviolet luminescence. Wurtzite ZnS nanobelts have been found to form as en molecules escape via hydration from the lamellar structures of $\text{ZnS}\cdot(\text{en})_{0.5}$ nanobelts, which are a reaction intermediate produced at the early stage of the reaction. The chemical composition, the morphology, and the optical properties of produced ZnS nanobelts have been controlled well by systematically varying time, temperature, and solvents. In particular, wurtzite ZnS nanobelts of 1.0 μm in length, 80 nm in width, and 16 nm in thickness, grown optimally in the 1:1:2 volume mixture of water:en: $\text{N}_2\text{H}_4\cdot\text{H}_2\text{O}$ at 180 °C for 6 h, have intense and narrow band-edge emission at room temperature, suggesting their potential applications in nano-optoelectronic devices.

[†]This is reproduced from Yeonho Kim and Du-Jeon Jang, *CrystEngComm* **2014**, 16, 6989. © 2014 Royal Society of Chemistry.

3B. 2. Introduction

The control of the sizes, shapes, and compositions of nanostructured materials with functional properties has been widely explored as nanomaterials can be employed potentially in a diverse range of technologies.¹⁻⁵ In particular, nanostructured semiconductors have drawn considerable attention owing to their unique structural, electronic, and optical properties originating from their large surface-to-volume ratios compared to their bulk counterparts.⁶⁻⁹ Among them, one-dimensional (1-D) nanostructures of ZnS are highly attractive building blocks for nanodevices due to their inherent efficient transport of electrons and excitons through their longitudinal direction.¹⁰⁻¹⁶ At ambient conditions, ZnS shows two structural polymorphs: hexagonal wurtzite and cubic zinc blende. Nanostructured systems can often have considerable electron-trapping vacancies such as Schottky and Frenkel defects. Schottky defects are more prevalent in cubic zinc blende ZnS nanostructures than in hexagonal wurtzite ZnS nanostructures. The defects may be responsible for bringing about trap states that lead to suppress the band-edge transition of excitons. Thus, in a view point of luminescence applications, the optical properties of wurtzite ZnS nanostructures are much more desirable than those of zinc blende ZnS nanostructures.¹⁷ However, it is difficult to synthesize pure wurtzite ZnS nanostructures at relatively low temperatures (below 200 °C); most ZnS nanocrystals synthesized via low-temperature

solution-phase methods have the zinc blende structure. In this manner, exploring the low-temperature synthesis of wurtzite ZnS nanoparticles has been a hot field in the current research of ZnS nanomaterials.

Commonly, high-temperature vapor-phase approaches such as chemical vapor deposition and thermal evaporation have been adopted to synthesize highly single-crystalline wurtzite ZnS nanostructures.^{18,19} However, these vapor-phase techniques usually suffer from high cost owing to the usage of expensive instruments and complicated processes. As an alternative, the fabrication of wurtzite ZnS nanostructures through a low-temperature solution route may have advantages of mild synthetic conditions and economic methods, as well as large scale in production. In addition, the formation mechanism of the nanostructures can also be understood in the solution route by controlling reaction parameters such as growth temperature, reaction time, and solvent compositions. Thus, many researchers have focused on the development of synthetic protocols for nanoscaled 1-D wurtzite ZnS with controlled morphologies and optical properties. For instance, a solvent coordinating molecular template of ethylenediamine (en) has been used generally for the synthesis of wurtzite ZnS nanocrystals. The hexagonal wurtzite structure has been reported to form preferentially and most stably when the surface atoms of ZnS are passivated with N atoms.²⁰ However, the molecular template of en often binds with Zn and S to form the inorganic-organic hybrid nanostructures of ZnS·(en)_{0.5}. Thus, wurtzite ZnS nanostructures have often been prepared

via post thermal treatment; the decomposition of $\text{ZnS}\cdot(\text{en})_{0.5}$ nanostructures has been reported to take place in a vacuum or solution at a relatively high temperature.²¹ Recently, we have reported a single-step mild hydrothermal approach for the synthesis of single-crystalline wurtzite ZnS nanobelts using ternary solvents of en, hydrazine, and water.²² However, the growth mechanism of wurtzite ZnS nanobelts via forming an intermediate material of $\text{ZnS}\cdot(\text{en})_{0.5}$ in a single-step solution process has not been understood adequately yet.

In this study, we report the facile-growth mechanism of wurtzite ZnS nanobelts in a solution process (Figure 3B-1), revealing that the reaction parameters such as temperature, time, and solvents play important roles in the determination of the morphologies, crystallinities, chemical compositions, and optical properties of the products. The molecular templates of en molecules escape from the lamellar structures of $\text{ZnS}\cdot(\text{en})_{0.5}$ nanostructures through interactions with water molecules; water, introduced as one of the mixed solvents, effectively eliminates en molecules intercalated in ZnS layers to make the entire synthetic route completed in a single step without requiring any post treatment for the fabrication of hexagonal wurtzite ZnS nanobelts. Consequently, we have found the optimal conditions of 180 °C and 6 h in the 1:1:2 volume mixture of water:en:N₂H₄·H₂O to synthesize well-defined wurtzite ZnS nanobelts having intense and narrow ultraviolet emission at room temperature.

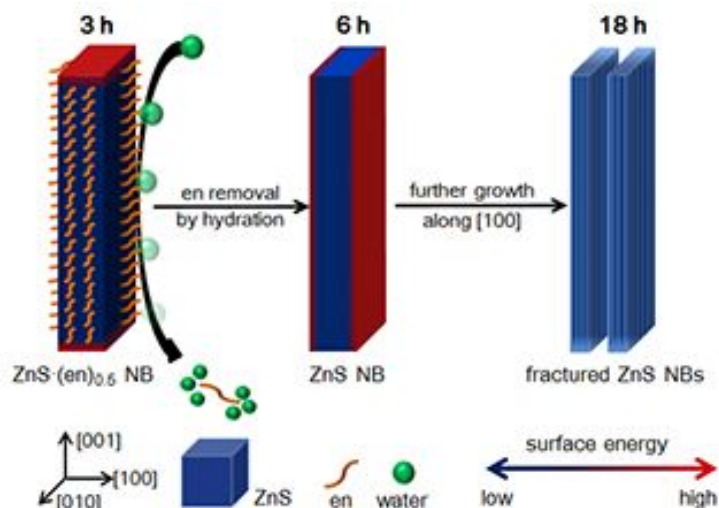


Figure 3B-1. Schematic illustration for the growth of wurtzite ZnS nanobelts (NBs).

3B. 3. Experimental Details

Materials. The analytical grade chemicals of $\text{N}_2\text{H}_4\cdot\text{H}_2\text{O}$ (l, >98%), ethylenediamine (en, l, >99%), ZnCl_2 (s, >98%), and S (s, >99.98%) were used as purchased from Sigma-Aldrich without further purification. Triply deionized water with a resistivity of greater than $18 \text{ M}\Omega \text{ cm}$, from a Millipore Milli-Q system, was used throughout the experiments.

Synthesis of wurtzite ZnS nanobelts. Single-crystalline wurtzite ZnS nanobelts were prepared via a hydrothermal process according to reported method²² with some modification. A stock solution of Zn^{2+} was prepared by adding 1.0 mmol of ZnCl_2 into 7.5 mL of water and 7.5 mL of en slowly with mild stirring and the stock solution was stirred further for 40

min to make a clear solution. A stock solution of S^{2-} was prepared by adding of 1.0 mmol of S into 15 mL of $N_2H_4 \cdot H_2O$ with vigorous stirring for 40 min. The stock solutions of Zn^{2+} and S^{2-} were mixed together and stirred vigorously for 20 min. The mixture solution was then loaded into a Teflon-lined stainless-steel autoclave of 50 mL capacity, placed in a preheated oven at 180 °C for 6 h, and cooled to room temperature. A white precipitate produced in the reaction mixture was washed three times with water and three times with ethanol, vacuum-dried, and kept in a vial for further characterization.

Characterization. Transmission electron microscopy (TEM) images were obtained with a JEOL JEM-2100 microscope, and high-angle annular dark-field scanning TEM (HAADF-STEM) images were measured using an FEI Tecnai F20 microscope. While high-resolution X-ray diffraction (HRXRD) patterns were obtained with a Bruker D8 DISCOVER diffractometer using Cu $K\alpha$ radiation (0.15418 nm), X-ray photoelectron spectroscopy (XPS) spectra were monitored using a Kratos AXIS-HSi spectrometer with an excitation source of Mg $K\alpha$ (1253.60 eV). Fourier- transform infrared (FTIR) spectra were obtained with a Thermo Scientific Nicolet 6700 spectrometer. Thermo gravimetric analysis (TGA) was carried out at a heating rate of 10 °C min^{-1} under a constant N_2 -flow rate of 25 mL min^{-1} using a TA instruments Q-5000 system. Extinction spectra were obtained with a Scinco S3100 UV/vis spectrophotometer, and photoluminescence spectra were measured employing a Princeton Instruments ICCD576G CCD detector attached to a 0.5 m Acton

Research Spectrapro-500 spectrometer with excitation using 266 nm pulses of 6 ns from a Q-switched Quantel Brilliant Nd:YAG laser.

3B. 4. Results and Discussion

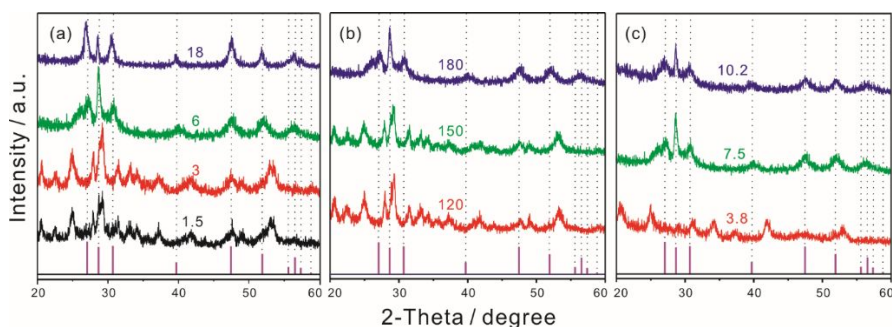


Figure 3B-2. HRXRD patterns of ZnS nanobelts grown with 7.5 mL of water at 180 °C for reaction times indicated in the units of h (a), grown with 7.5 mL of water for 6 h at reaction temperatures indicated in the units of °C (b), and grown for 6 h at 180 °C with water amounts indicated in the units of mL. Each bottom pattern is from the reference wurtzite ZnS (JCPDS Card No. 36-1450).

The HRXRD patterns of Figure 3B-2 reveal that the structures of as-synthesized ZnS nanobelts change with reaction time, temperature, and solvent composition. Figure 3B-2a indicates that the diffraction patterns of nanostructures grown for 1.5 and 3 h can be correlated well with the reported pattern of the orthorhombic $\text{ZnS} \cdot (\text{en})_{0.5}$, whereas the diffraction pattern of nanobelts grown for 6 h agrees well with the standard pattern of the reference wurtzite ZnS.²³ The diffraction peak at 2θ of 28.5° , indexed as the (002) plane, for ZnS nanobelts grown for 6 h surpasses diffraction peaks arising from any

other planes, supporting that our ZnS nanobelts have grown preferentially to the direction of [001]. HRTEM images and FFT pattern in our previous report²² also indicate that the ZnS nanobelts have grown to the direction of [001]. The nanocrystals grown for 18 h can also be assigned to the wurtzite ZnS although the intensity of the peak at 2θ of 28.5° is now comparable to the intensities of other peaks. In other words, the diffraction pattern of nanostructures grown for 18 h is very similar to the standard pattern of the randomly oriented bulk ZnS. The mean crystallite diameters of wurtzite ZnS nanobelts grown for 6 and 18 h, estimated with the line widths of the peak at 2θ of 28.5° using the Scherrer's formula,²³ are 21 and 34 nm, respectively, revealing that the average crystallite size of ZnS nanobelts increases with the increment of the reaction time. The relative intensity of the diffraction peak at 2θ of 28.5° , indexed as the (002) plane, decreases whereas the relative intensities of the peaks at 2θ of 26.9° and 47.6° , indexed as the (100) and the (110) planes, respectively, increase as the reaction time changes into 18 h from 6 h. I have measured the intensity of the (100) diffraction peak relatively to that of the (002) diffraction peak for ZnS nanobelts. The measured values of ZnS nanobelts grown for 6 and 18 h are 0.58 and 1.53, respectively, suggesting that the additional crystal growth of our ZnS nanobelts has occurred preferentially along the [100] direction during the reaction time of > 6 h as the (100) planes become unstable energetically²⁴ with the removal of en molecules by hydration. The XRD patterns of the nanostructures prepared at different reaction temperatures are shown in Figure 3B-2b, designating that

wurtzite ZnS nanobelts have been produced preferentially at 180 °C whereas ZnS·(en)_{0.5} nanostructures have been formed at 120 and 150 °C. It is suggested that the ZnS nanobelts can be generated at a high temperatures of 180 °C as water molecules extract en ligands intercalated in ZnS·(en)_{0.5} nanostructures via forming hydrogen bonds. Furthermore, Figure 3B-2c also suggests that an enough amount (≥ 7.5 mL) of water is essential to extract en ligands from ZnS·(en)_{0.5} nanostructures via forming hydrated solvation shells to produce wurtzite ZnS nanobelts.

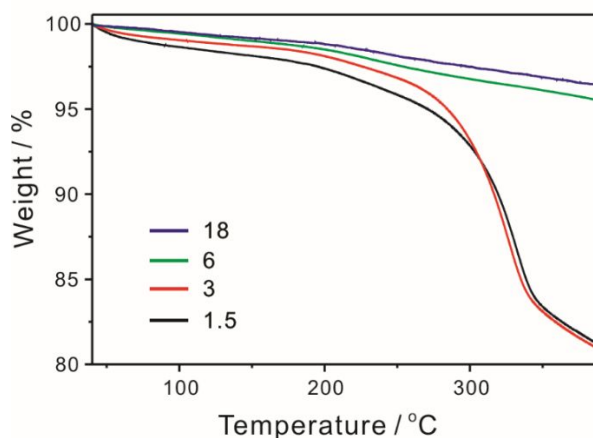


Figure 3B-3. TGA curves of ZnS nanobelts grown at 180 °C for reaction times indicated in the units of h.

In order to ascertain the chemical compositions of as-prepared products further, TGA curves have been measured (Figure 3B); the decomposition of nanostructures grown for 1.5 and 3 h begins at 240 °C with showing its maximum slope at 330 °C whereas the decomposition of nanostructures grown for 6 and 18 h occurs hardly with the increment of temperature. Thus,

Figure 3B-3 also supports that the nanostructures grown for 1.5 and 3 h consist of $\text{ZnS}\cdot(\text{en})_{0.5}$; their sharp weight decrease at 330 °C is due to the thermal loss of intercalated en molecules.²⁵ However, the composition of the nanostructures grown for 6 and 18 h is ZnS without having intercalated en molecules. The TGA curves of temperature-dependent nanostructures in Figure 3B-4 also imply that nanostructures of pure ZnS can be synthesized at a high reaction temperature of 180 °C. Overall, all the observations made with Figs. 3 and S1 agree well with the results discussed with the HRXRD patterns of Figure 3B-2, indicating that $\text{ZnS}\cdot(\text{en})_{0.5}$ nanostructures produced at an early stage transform into wurtzite ZnS nanobelts as the reaction proceeds over 6 h at 180 °C.

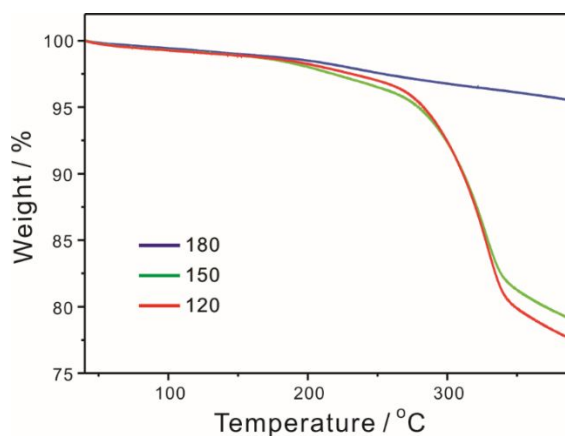


Figure 3B-4. TGA curves of ZnS nanobelts grown for 6 h at reaction temperatures indicated in the units of °C.

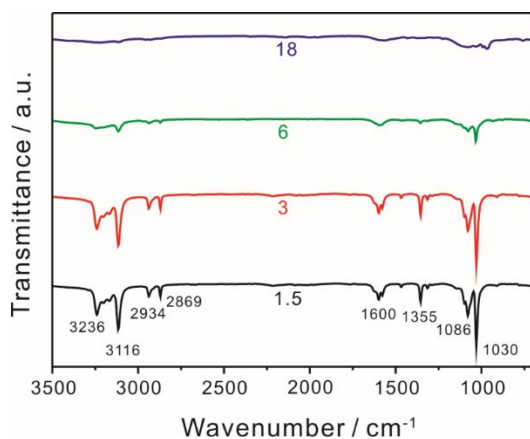


Figure 3B-5. FTIR spectra of ZnS nanobelts grown at 180 °C for reaction times indicated in the units of h.

The FTIR spectra of Figure 3B-5 reveal that ZnS nanobelts grown for 6 and 18 h hardly contain en molecules although nanostructures grown for 1.5 and 3 h do. The FTIR vibrational peaks of en molecules in $\text{ZnS} \cdot (\text{en})_{0.5}$ are much sharper and stronger than the respective ones of free liquid-state en molecules.²⁶ The two sharp peaks at 3236 and 3116 cm^{-1} in Figure 3B-5 are assigned to the asymmetric and the symmetric stretching vibrations of $-\text{NH}_2$, respectively, while the lines at 1600 and 1030 cm^{-1} are attributed to the scissoring and the wagging vibrations of $-\text{NH}_2$, respectively.²⁷ The absorption peaks at 2934, 2869, and 1355 cm^{-1} correspond to the asymmetric-, the symmetric-stretching, and the wagging vibrations of $-\text{CH}_2$, respectively, and the absorption peaks at 1086 cm^{-1} can be assigned to the C–N stretching vibration.²⁷ The FTIR spectra of nanostructures grown at various temperatures in Figure 3B-6 reveal that en-free pure ZnS nanostructures can be synthesized at a reaction temperature of 180 °C.

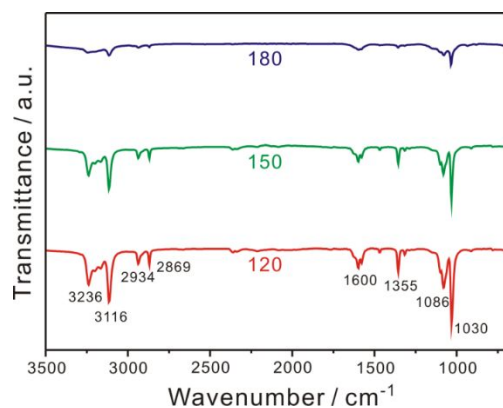


Figure 3B-6. FTIR spectra of ZnS nanobelts grown for 6 h at reaction temperatures indicated in the units of °C.

Thus, the FTIR spectra of Figure 3B-5 as well as the TGA curves of Figure 3B-3 suggest that all the en ligands in ZnS·(en)_{0.5} nanostructures grown for 1.5 and 3 h disappear completely to produce ZnS nanobelts as the reaction proceeds for ≥ 6 h at 180 °C.

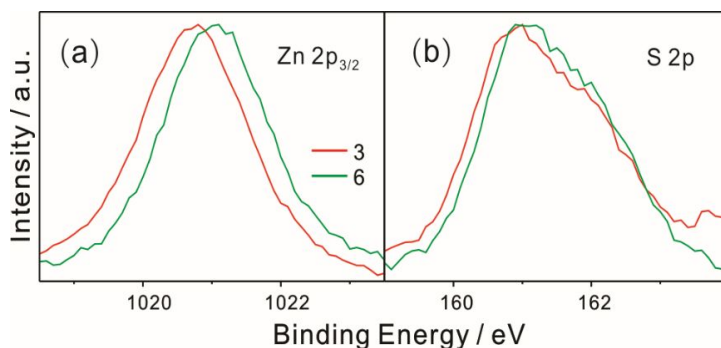


Figure 3B-7. Maximum-normalized Zn 2p_{3/2} (a) and S 2p (b) XPS spectra of ZnS nanobelts grown at 180 °C for reaction times indicated in the units of h.

The XPS spectra of Figure 3B-7 can provide further significant information about the surface composition of nanostructures. The binding energies obtained in the XPS analysis have been corrected for specimen charging through referencing the C 1s to 284.5 eV. Figure 3B-6 shows that the binding energies of both Zn 2p_{3/2} and S 2p increase with the increment of the reaction time, suggesting that the surface composition of the product changes substantially as the reaction time increases from 3 h to 6 h. While the observed binding energies of Zn 2p_{3/2} and S 2p for nanostructures grown for 3 h are 1020.8 and 160.8 eV, which correspond respectively to the reported values (1020.8 and 160.9 eV) of ZnS·(en)_{0.5} nanobelts,²³ those for nanostructures grown for 6 h are 1021.1 and 161.1 eV, which agree well respectively to the reported values (1021.15 eV and 161.15 eV) of ZnS nanostructures.²⁸ Thus, as discussed with Figure 3B of 2-6, and 3B-7 suggests that the chemical composition of ZnS·(en)_{0.5} nanostructures has been changed into ZnS as the growth time increases from 3 h to 6 h. It is considered that the respective binding energies of Zn 2p_{3/2} and S 2p increase by 0.3 eV as the electron-donating en molecules are removed from the intercalated layers of ZnS during the transformation of ZnS·(en)_{0.5} nanobelts into ZnS nanobelts.

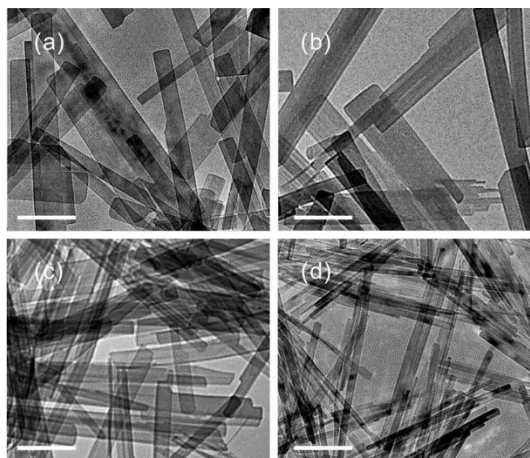


Figure 3B-8. TEM images of ZnS nanobelts grown at 180 °C for 1.5 (a), 3 (b), 6 (c), and 18 h (d), where each scale bar indicates 200 nm.

The TEM images of Figure 3B-8 show that ZnS nanostructures undergo morphology evolution as the reaction time increases; the average length-to-width ratio of the nanostructures increases with the increment of the reaction time. The mean width of the nanostructures decreases from 110 nm to 40 nm with the increase of the reaction time from 1.5 to 18 h, whereas the average length of 1.0 μm and the typical thickness of 16 nm remain almost invariant regardless of the reaction time. The close examination of Figure 3B-8 reveals that the mean width of nanostructures remains to be the same as 110 nm with the increase of the reaction time from 1.5 h to 3 h, whereas the average width decreases from 80 nm to 40 nm with the increment of the reaction time from 6 h to 18 h. Considering Figure 3B of 2-7, we suggest that the average width of nanostructures decreases during the reaction time from 3 h to 6 h as en molecules intercalated in $\text{ZnS}\cdot(\text{en})_{0.5}$ nanobelts are removed via interacting

with water molecules to produce pure ZnS nanobelts. The further decrease of the average width during the reaction time from 6 h to 18 h is considered to arise from fracture between (100) planes, which have been unstable energetically by the removal of en molecules. The HAADF-STEM images of Figure 3B-9 display that fissures between (100) planes exist already in ZnS nanobelts grown for 6 h and that they are cleaved in the reaction time of 18 h to yield ZnS nanobelts with a smaller average width.

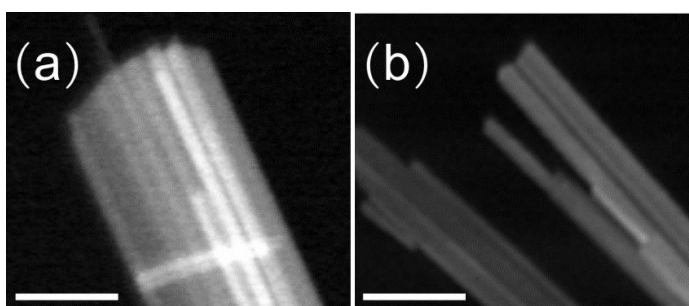


Figure 3B-9. HAADF-STEM images of ZnS nanobelts grown at 180 °C for 6 (a) and 18 h (b), where each scale bar indicates 50 nm.

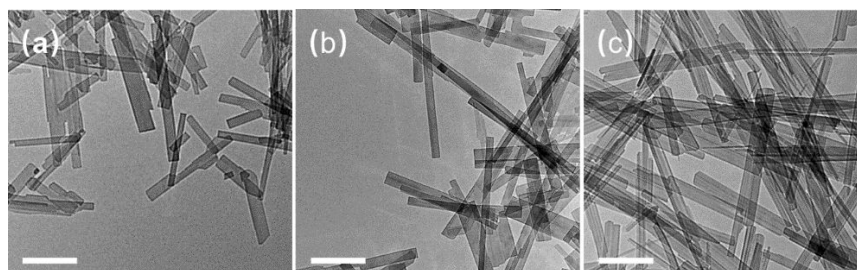


Figure 3B-10. TEM images of ZnS nanobelts grown for 6 h at 120 (a), 150 (b), and 180 °C (c), where each scale bar indicates 200 nm.

The TEM images of nanostructures grown at various temperatures in Figure 3B-10 show that ZnS nanostructures grown at 180 °C, in particular, have well-defined nanobelt structures with uniform widths. Thus, Figures 3B-8 and 3B-10, together with Figure 3B-2, have suggested that the best structures of wurtzite ZnS nanobelts can be grown in the 1:1:2 volume mixture of water:en:N₂H₄·H₂O at 180 °C for 6 h.

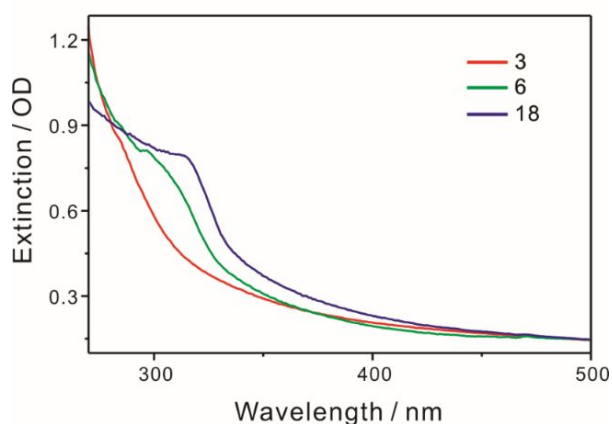


Figure 3B-11. Extinction spectra of ZnS nanobelts grown at 180 °C for reaction times indicated in the units of h. The nanobelts were suspended in ethanol.

The extinction spectra of Figure 3B-11 show that the discernible absorption band of ZnS nanobelts grown for 6 h appears around 310 nm, indicating that the nanostructure have relatively narrow size distribution.²⁹ The ZnS nanobelts grown for 18 h show the absorption band near 320 nm, which is shifted to the red by 10 nm from the above mentioned absorption band. This suggests that the residual en molecules present in ZnS nanobelts

have been removed completely with the increment of the reaction time. Furthermore, ZnS(en)_{0.5} nanobelts grown for 3 h do not show any absorption band at wavelengths longer than 300 nm as the band-gap energy (4.7 eV) of ZnS(en)_{0.5} corresponds to the photon energy of 265 nm.

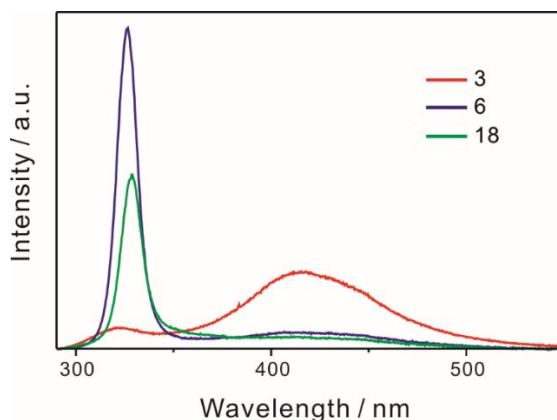


Figure 3B-12. Photoluminescence spectra of ZnS nanobelts grown at 180 °C for reaction times indicated in the units of h. The nanobelts were suspended in ethanol and excited with 266 nm laser pulses of 6 ns.

Each room-temperature photoluminescence (PL) spectrum of ZnS nanobelts in Figure 3B-12 shows two characteristic emission bands of band-edge emission in the ultraviolet (UV) region and defects-related emission in the visible region;^{22,30-35} the luminescent intensities of these two emission bands vary very widely with the reaction time. Whereas nanostructures grown for 3 h show a prevailing visible-emission band at 415±24 nm with a UV-emission band at 322.0±14.6 nm, nanobelts grown for 6 h display a dominant UV-emission band at 326.4±6.4 nm with an extremely weak visible-emission

band at 415 ± 24 nm. The red shift of the UV emission by 6.4 nm with the increment

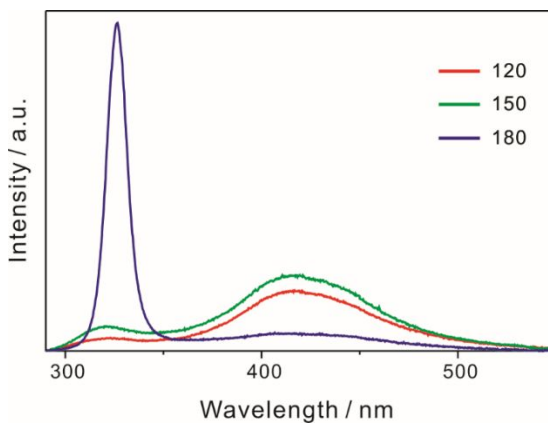


Figure 3B-13. Photoluminescence spectra of ZnS nanobelts grown for 6 h at reaction temperatures indicated in the units of °C. The nanobelts were suspended in ethanol and excited with 266 nm laser pulses of 6 ns.

of the reaction time from 3 h to 6 h also supports the previous suggestion that en molecules intercalated in ZnS layers have been removed via interactions with water molecules. The maximum value of the UV emission relative to that of the visible emission increases from 0.27 to 21.5 as the reaction time increases from 3 h to 6 h, suggesting that sulfur vacancies, responsible for the visible-emission band at 415 nm and present abundantly in $\text{ZnS} \cdot (\text{en})_{0.5}$ nanobelts, have been removed mostly by the removal of en molecules to yield perfectly crystalline ZnS nanobelts. In the meantime, ZnS nanobelts grown for 18 h have the UV-emission band at 328.8 ± 6.8 nm, which is shifted to the red by 2.4 nm from that of ZnS nanobelts grown for 6 h. This shift is considered to result from the complete removal of the residual en molecules present in

ZnS nanobelts with the increase of the reaction of the UV-emission band decreases by 46% as the reaction time increases from 6 h to 18 h. This has been attributed to increased surface states, probably present abundantly at cleavages between (100) planes as discussed with Figures. 3B-8 and 3B-9, which work as electron-trapping sites by blocking the recombination of electrons in the conduction band with holes in the valence band. The XRD patterns of Figure 3B-2 show obviously that the diffraction peak of the (100) plane is stronger than any other peaks in ZnS nanobelts grown for 18 h. The PL spectra of nanostructures grown at various temperatures in Figure 3B-13 indicate that ZnS nanobelts grown particularly at 180 °C have outstanding UV-emitting properties. Thus, Figures 3B-12 and 3B-13, together with Figure 3B-2, have suggested that the best synthetic conditions for the growth of wurtzite ZnS nanobelts having intense UV emission are the reaction temperature of 180 °C and the growth time of 6 h in the 1:1:2 volume mixture of water:en:N₂H₄·H₂O.

3B. 5. Conclusion

Hexagonal wurtzite ZnS nanobelts showing intense and narrow UV emission at room temperature have been synthesized via a single-step hydrothermal process and their facile-growth mechanism has been investigated by varying reaction conditions systematically. A ligand of en binds to two Zn^{2+} ions to form $2\text{Zn}\cdot(\text{en})_{0.5}^{2+}$ and S^{2-} , produced by the reduction of S by $\text{N}_2\text{H}_4\cdot\text{H}_2\text{O}$, binds with $\text{Zn}\cdot(\text{en})_{0.5}^{2+}$ to generate $\text{ZnS}\cdot(\text{en})_{0.5}$ nanobelts as a reaction intermediate at the early stage, which then transform into ZnS nanobelts in a solution having an enough amount of water at 180 °C. During the transformation, the average width of nanostructures decreases as intercalated en molecules are removed via interacting with water molecules to yield perfectly crystalline ZnS nanobelts having outstanding UV-emitting properties; the UV emission of ZnS nanobelts increases by 15 times and the binding energies of Zn $2p_{3/2}$ and S 2p increase by 0.3 eV as electron-donating en molecules are removed. The average width decreases further during the reaction time from 6 h to 18 h due to cleavages between (100) planes; the UV emission decreases by 46% due to increased surface states. Consequently, we suggest that the best structures of wurtzite ZnS nanobelts with excellent UV-emitting properties can be grown optimally in the 1:1:2 volume mixture of water:en: $\text{N}_2\text{H}_4\cdot\text{H}_2\text{O}$ at 180 °C for 6 h. Well-known two-step routes, especially the second elimination step of amine derivatives, for the fabrication of wurtzite ZnS nanostructures could induce surface and non-stoichiometric

defects to exist, enhancing defects-related emission. However, wurtzite ZnS nanobelts synthesized via a single-step process hardly have defects or surface states, showing intense, narrow, and band-edge UV luminescence with negligible defects-related visible emission at room temperature.

3B. 6. Acknowledgements

This work was supported by a research grant from the National Research Foundation (NRF) of Korea (2011-0028981). D.J.J. is also thankful to the SRC program of NRF (2007-0056331).

3B. 7. References

- (1) J. M. Caruge, J. E. Halpert, V. Wood, V. Bulovic and M. G. Bawendi, *Nat. Photon.*, **2008**, *2*, 247.
- (2) S. J. Kim, C. S. Ah and D.-J. Jang, *Adv. Mater.*, **2007**, *19*, 1064.
- (3) M. R. Kim, D. K. Lee and D.-J. Jang, *Appl. Catal. B: Environ.*, **2011**, *103*, 253.
- (4) M. Stefan, S. V. Nistor, D. Ghica, C. D. Mateescu, M. Nikl and R. Kucerkova, *Phys. Rev. B*, **2011**, *83*, 045301.
- (5) J.-A. Kwak, D. Lee and D.-J. Jang, *Appl. Catal. B: Environ.*, **2013**, *142-143*, 323.
- (6) T. J. Kempa, R. W. Day, S.-K. Kim, H.-G. Park and C. M. Lieber, *Energy Environ. Sci.*, **2013**, *6*, 719.

- (7) H. Zheng, J. B. Rivest, T. A. Miller, B. Sadtler, A. Lindenberg, M. F. Toney, L.-W. Wang, C. Kisielowski and A. P. Alivisatos, *Science*, **2011**, 333, 206.
- (8) Y. Kim and D.-J. Jang, *Chem. Commun.*, **2013**, 49, 8940.
- (9) F. Dawood and R. E. Schaak, *J. Am. Chem. Soc.*, **2009**, 131, 424.
- (10) D. Moore and Z. L. Wang, *J. Mater. Chem.*, **2006**, 16, 3898.
- (11) U. K. Gautam, X. Fang, Y. Bando, J. Zhan and D. Golberg, *ACS Nano*, **2008**, 2, 1015.
- (12) L. Hu, J. Yan, M. Liao, H. Xiang, X. Gong, L. Zhang and X. Fang, *Adv. Mater.*, **2012**, 24, 2305.
- (13) X. Fang, Y. Bando, M. Liao, U. K. Guatam, C. Zhi, B. Dierre, B. Liu, T. Zhai, T. Sekiguchi, Y. Koide and D. Golberg, *Adv. Mater.*, **2009**, 21, 2034.
- (14) M.-Z. Wang, W.-J. Xie, H. Hu, Y.-Q. Yu, C.-Y. Wu, L. Wang and L.-B. Luo, *Appl. Phys. Lett.*, **2013**, 103, 213111.
- (15) H. He, Y. Y. Zhang, J. Liu, D. Moore, G. Bao and Z. L. Wang, *J. Phys. Chem. C*, **2007**, 111, 12152.
- (16) Y.-Q. Yu, L.-B. Luo, Z.-F. Zhu, B. Nie, Y.-G. Zhang, L.-H. Zeng, Y. Zhang, C.-Y. Wu, L. Wang and Y. Jiang, *CrystEngComm*, **2013**, 15, 1635.
- (17) S. B. Qadri, E. F. Skelton, A. D. Dinsmore, J. Z. Hu, W. J. Kim, C. Nelson and B. R. Ratna, *J. Appl. Phys.*, **2001**, 89, 115.
- (18) R. Chen, D. Li, B. Liu, Z. Peng, G. G. Gurzadyan, Q. Xiong and H. Sun, *Nano. Lett.*, **2010**, 10, 4956.

- (19) S. Chen, L. Li, X. Wang, W. Tian, X. Wang, D.-M. Tang, Y. Bando, and D. Golberg, *Nanoscale*, **2012**, *4*, 2658.
- (20) S. A. Acharya, N. Maheshwari, L. Tatikondewar, A. Kshirsagar and S. K. Kulkarni, *Cryst. Growth Des.*, **2013**, *13*, 1369.
- (21) L. Nasi, D. Calestani, T. Besagni, P. Ferro, F. Fabbri, F. Licci and R. Mosca, *J. Phys. Chem. C*, **2012**, *116*, 6960.
- (22) Y. Kim and D.-J. Jang, *RSC Adv.*, **2013**, *3*, 16945.
- (23) Y. Kim, J.-Y. Kim and D.-J. Jang, *J. Phys. Chem. C*, **2012**, *116*, 10296.
- (24) Z. Wang, L. L. Daemen, Y. Zhao, C. S. Zha, R. T. Downs, X. Wang, Z. L. Wang and R. J. Hemley, *Nat. Mater.*, **2005**, *4*, 922.
- (25) J. Zhao, J. Yin and M. Yang, *J. Alloys. Comp.*, **2013**, *579*, 45.
- (26) Z.-X. Deng, C. Wang, X.-M. Sun and Y.-D. Li, *Inorg. Chem.*, **2002**, *41*, 869.
- (27) L. Zhang, H. Yang, L. Li, R. Zhang, R. Liu, J. Ma, X. Xie and F. Gao, *Inorg. Chem.*, **2008**, *47*, 11950.
- (28) D. H. Lee, J. Y. Jung, E. J. Bae, T. J. Lee, S. O. Ryu and C. H. Chang, *J. Korean Phys. Soc.*, **2008**, *53*, 102.
- (29) J. Nanda, S. Sapra, D. D. Sarma, N. Chandrasekharan and G. Hodes, *Chem. Mater.*, **2000**, *12*, 1018.
- (30) J. Zhang, Y. Yang, F. Jiang, J. Li, B. Xu, X. Wang and S. Wang, *Nanotechnology*, **2006**, *17*, 2695.
- (31) S. Park, C. Jin, H. Kim, C. Hong, C. Lee, *J. Lumin.*, **2012**, *132*, 231.
- (32) W. G. Becker and A. J. Bard, *J. Phys. Chem.*, **1983**, *87*, 4888.

- (33) J. S. McCloy and B. G. Potter, *Opt. Mater. Express*, **2013**, *3*, 1273.
- (34) L.-J. Tang, G.-F. Huang, Y. Tian, W.-Q. Huang, M.-G. Xia, C. Jiao, J.-P. Long and S.-Q. Zhan, *Mater. Lett.*, **2013**, *100*, 237.
- (35) W.-T. Yao, S.-H. Yu and Q.-S. Wu, *Adv. Funct. Mater.*, **2007**, *17*, 623.

**Chapter 4. Applications of Graphene-ZnS Nanobelts Hybrid
Nanostructures**

Part 4A. High-Performance Ultraviolet Photodetectors Based on Solution-Grown ZnS Nanobelts Sandwiched Between Graphene Layers

4A. 1. Abstract

Ultraviolet (UV) light photodetectors constructed from solely inorganic semiconductors still remain unsatisfactory because of their low electrical performances. To overcome this limitation, the hybridization is one of the key approaches that have been recently adopted to enhance the photocurrent. High-performance UV photodetectors showing stable on-off switching and excellent spectral selectivity have been fabricated based on the hybrid structure of solution-grown ZnS nanobelts and CVD-grown graphene. Sandwiched structures and multilayer stacking strategies have been applied to expand effective junction between graphene and photoactive ZnS nanobelts. A multiply sandwich-structured photodetector of graphene/ZnS has shown a photocurrent of 0.115 mA under illumination of 1.2 mWcm^{-2} in air at a bias of 1.0 V, which is higher 10^7 times than literature values. The multiple-sandwich structure of UV-light sensors with graphene having high conductivity, flexibility, and impermeability is suggested to be beneficial for the facile fabrication of UV photodetectors with extremely efficient performances.

[†]This is reproduced from Yeonho Kim, Sang Jin Kim, Sung-Pyo Cho, Byung Hee Hong, and Du-Jeon Jang, *Sci. Rep.* **2015**, *5*, 12345. © 2015 Nature Publishing Group.

4A. 2. Introduction

Photodetectors are a type of electronic devices for sensing light, and they have been found to have broad applications including flame monitoring, missile-plume detection, and space communication.¹⁻⁴ Wide bandgap semiconductor nanostructures such as ZnS, ZnO, and GaN as well as graphene quantum dots have been utilized as photoactive materials of photodetectors.³⁻¹⁰ In particular, ZnS is a well-known semiconductor having a direct band gap of 3.67 eV, and it has been studied as functional parts in visible-blind ultraviolet (UV) photodetectors owing to its excellent optoelectronic properties.^{11,12} Among ZnS nanomaterials, one-dimensional (1-D) nanostructures of ZnS have been known to be highly attractive building blocks for high-performance photodetectors.^{5,11} The large surface-to-volume ratios and the deep-level surface trap states of 1-D nanostructures greatly prolong the lifetime of photocarriers and the reduced dimensionality of the active area in low-dimensional devices shortens the carrier transit time.^{13,14} However, UV-light photodetectors constructed with 1-D ZnS nanostructures still display a weak photocurrent and unsatisfactory stability.¹⁵⁻¹⁸ In order to overcome these limitations, hybridized structures have been attracted great attention owing to their superior optoelectronic properties compared to corresponding individual materials.¹⁹⁻²³ Graphene is a single atomic layer consisting of carbon atoms arranged in a hexagonal honeycomb lattice, and it has been reported as one of the fascinating two-dimensional materials due to

its outstanding physical properties including high mechanical flexibility,^{24,25} electrical conductivity,²⁶⁻²⁹ and transparency.³⁰ In addition, graphene has an excellent stability under ambient conditions due to its outstanding impermeability.³¹⁻³³ The incorporation of transparent and conductive graphene into photoactive semiconductors can be considered to provide synergistic effects in light absorption and carrier transportation. In recent studies, the hybridization of graphene and semiconductors has demonstrated enhanced performances for UV-light photodetection, although their heterostructures still suffer from the small area of the effective-junction region contributing to the photocurrent.³⁴⁻³⁶

In this present study, we present that high-performance UV photodetectors showing stable on-off switching and spectral selectivity have been fabricated via a facile process based on the hybrid structure of solution-grown ZnS nanobelts and CVD-grown graphene. Sandwich structures and multi-layer stacking strategies have been applied to the photodetectors for the increment of the effective-junction region between graphene and ZnS. Three kinds of UV photodetectors, ZnS spin-coated on the surface of double-layer graphene (D-G/ZnS), ZnS sandwiched between two graphene layers (S-G/ZnS), and multiply sandwiched graphene and ZnS (MS-G/ZnS), have been demonstrated in ambient conditions at a low bias voltage. The photo-response behavior of a photodetector has been found to depend considerably on the stacking sequence of graphene and ZnS, as well as on the number of layers. An optimized photodetector based on S-G/ZnS shows a high photocurrent of 37

μA , which is higher 10^6 times than the reported values of graphene-free UV photodetectors based on ZnS nanobelts¹⁶ and ZnS-ZnO nanowires.¹¹

4A. 3. Experimental Details

Graphene synthesis and transfer. Graphene was synthesized on a copper foil (Alpha Aecer, 99.999%) via a chemical vapor deposition (CVD) method at $1,000\text{ }^\circ\text{C}$ using a mixed gas of CH_4 (30 SCCM) and H_2 (3 SCCM) as the reaction source. After coating a poly(methylmethacrylate) (PMMA) polymer layer on the as-grown graphene of one side of the Cu foil, the graphene on the other side of the Cu foil was removed by oxygen plasma. After the Cu foil was etched with an ammonium persulfate (APS) solution and rinsed with distilled water several times, the graphene was transferred on a target substrate. The sample was soaked in acetone to remove the PMMA layer.

ZnS nanobelts synthesis. Single-crystalline wurtzite ZnS nanobelts were prepared via a hydrothermal process according to the reported method⁴¹ with some modification. A stock solution of Zn^{2+} was prepared by adding 1.0 mmol of $\text{ZnCl}_2(\text{s})$ into 7.5 mL of water and 7.5 mL of $\text{C}_2\text{H}_4(\text{NH}_2)_2(\text{l})$ slowly with mild stirring; the stock solution was stirred further for 20 min to make a clear solution. A stock solution of S^{2-} was prepared by adding 1.0 mmol of $\text{S}(\text{s})$ into 15 mL of $\text{N}_2\text{H}_4\cdot\text{H}_2\text{O}(\text{l})$ with vigorous stirring for 20 min. The stock solutions

of Zn^{2+} and S^{2-} were mixed together and stirred vigorously for 5 min. The mixture solution was then loaded into a Teflon-lined stainless-steel autoclave of 50 mL capacity, placed in a preheated oven at 180 °C for 9 h, and cooled to room temperature. A white precipitate produced in the reaction mixture was washed three times with water and two times with ethanol, vacuum-dried, and kept in a vial for further characterization.

Device fabrication. Titanium (3 nm) and gold (30 nm) electrodes were deposited on a Si/SiO₂ (300 nm) wafer by thermal evaporation, and graphene was transferred on the top of the electrodes. After spin coating of ZnS nanobelts dispersed ethanol on graphene for 20 s at 500 rpm, additional graphene was transferred on the top of the as-prepared sample.

Characterization. Raman spectra and their mapping profiles were obtained by a Raman spectrometer (RM 1000-Invia, Renishaw, 514 nm), and AFM images were measured at a noncontact mode using an atomic force microscope (Park System, XE-100). TEM images and their SAED and FFT patterns were obtained with an electron microscope (JEOL, JEM- 3010) operating at 300 kV, and FE-SEM images were measured with another electron microscope (SUPRA, 55vp-zeiss). While optical microscopy images were obtained with a microscope (NIKON, Eclipse LV100ND), HRXRD patterns were obtained with a diffractometer (Bruker, D8 DISCOVER) using Cu K α radiation (0.15418 nm). Extinction spectra were obtained with a UV-vis spectrophotometer (Scinco, S3100). The current-voltage behaviors of

photodetectors were measured using a probe nanovoltmeter (Agilent, B2912A) with a Xe lamp (Schoeffel, LPS255HR) as the light source.

4A. 4. Results and Discussion

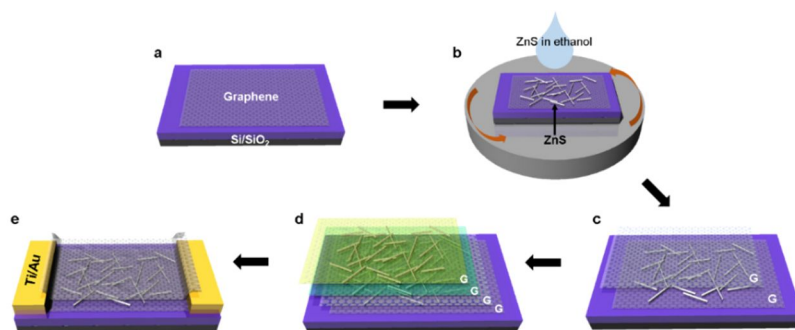


Figure 4A-1. Schematic for the fabrication of a G/ZnS device. (a) graphene transfer, (b) ZnS spin coating, (c) graphene stacking, (d) repeated b and c steps for multiple coating and stacking, and (e) device fabrication with metal electrodes.

Figure 4A-1 shows the fabrication schematics of a graphene and ZnS (G/ZnS) sandwich-structured device. Following graphene transfer on a Si/SiO₂ wafer (Figure 4A-1a), a ZnS-dispersed ethanol solution was spin-coated on the graphene to fabricate the hybrid structure of G/ZnS (Figure 4A-1b). While Figure 4A-1c shows the stacking of graphene on the G/ZnS surface, Figure 4A-1d designates repeated steps to stack G/ZnS layers multiply. An additional graphene layer was well-stacked on a G/ZnS surface owing to the highly mechanical and flexible properties of graphene. The

multiply stacked structure of G/ZnS is suggested to increase the effective-junction region of ZnS nanobelts and graphene as well as the absorbance of UV light. In addition, the overlying layer of impermeable graphene protects ZnS nanobelts from reactive environments. Figure 4A-1e shows the device fabrication of a UV-sensitive photodetector based on the prepared G/ZnS hybrid structure and metal electrodes (Ti/Au).

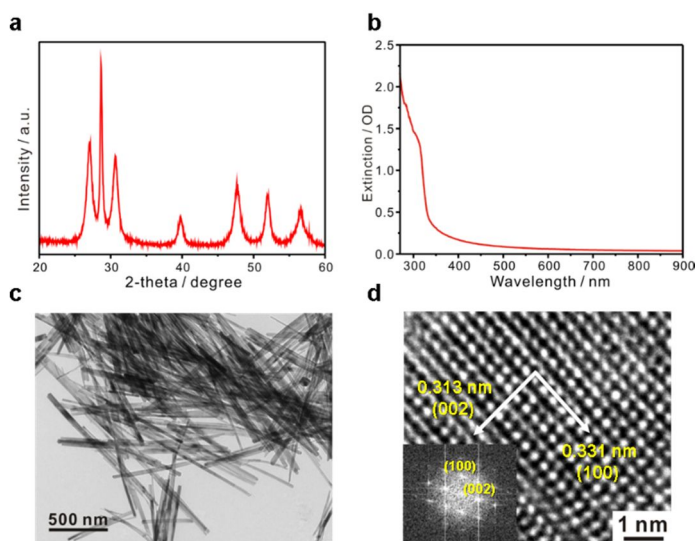


Figure 4A-2. (a) XRD pattern, (b) extinction spectrum (in ethanol), (c) TEM image, and (d) HRTEM image with an inserted FFT pattern of solution-grown ZnS nanobelts.

Figure 4A-2a shows that the X-ray diffraction (XRD) pattern of solution-grown ZnS nanobelts can be indexed to the standard pattern of the reference wurtzite ZnS without having obvious impurity peaks (JCPDS Card No. 36-1450). However, the diffraction peak at 2-theta of 28.5° , indexed as the (002)

planes, surpasses diffraction peaks arising from any other planes, supporting that ZnS nanobelts have grown preferentially to the direction of [001]. The extinction spectrum of Figure 4A-2b indicates characteristic absorption at 310 nm, which is one of the typical intrinsic optical features of ZnS nanomaterials giving rise to practical applications for photodetectors having spectral selectivity in the ultraviolet region. The transmission electron microscopy (TEM) image of Figure 4A-2c and the high resolution TEM (HRTEM) image of Figure 4A-2d display that as-prepared ZnS nanobelts have well-defined geometry with clear lattice fringes. The marked spacings of 0.313 nm and 0.331 nm in Figure 4A-2d agree well with the expected separations of the (002) and the (100) planes in the reference wurtzite ZnS, respectively. The inserted Fast Fourier Transform (FFT) pattern of the HRTEM image indicates the single-crystalline characteristics of our ZnS nanobelts with preferred growth along the [001] orientation.

The TEM image of Figure 4A-3a shows that ZnS nanobelts having a mean length of 2 μm , an average width of 80 nm, and a typical thickness of 16 nm lie closely each other on a graphene layer; ZnS nanobelts are fractured and aggregated during the sonication process of ZnS nanobelts-dispersed ethanol before spin coating onto the graphene-transferred substrate. Figure 4A-4 shows the digital image of an as-fabricated device with a channel length of 80 μm . The HRTEM image of Figure 4A-3b indicates that a highly single-crystalline ZnS nanobelt covers a graphene sheet without having any stacking faults at the atomic level.

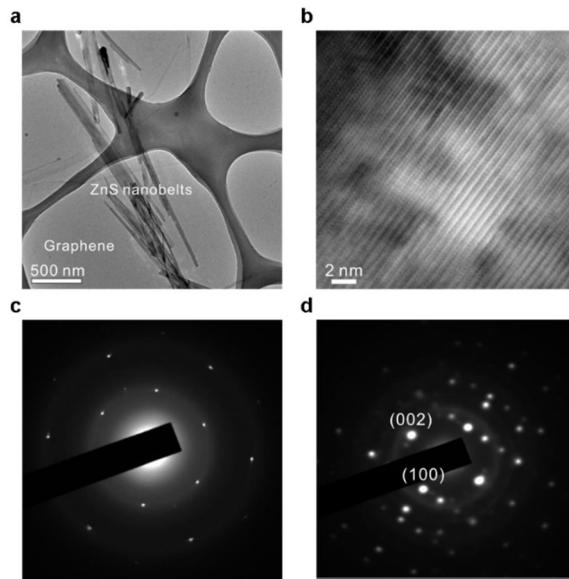


Figure 4A-3. (a) TEM and (b) HRTEM images of S-G/ZnS and SAED patterns of (c) graphene and (d) S-G/ZnS.

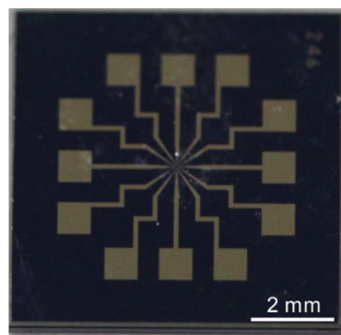


Figure 4A-4. Digital image of an as-fabricated device with a channel length of 80 μm .

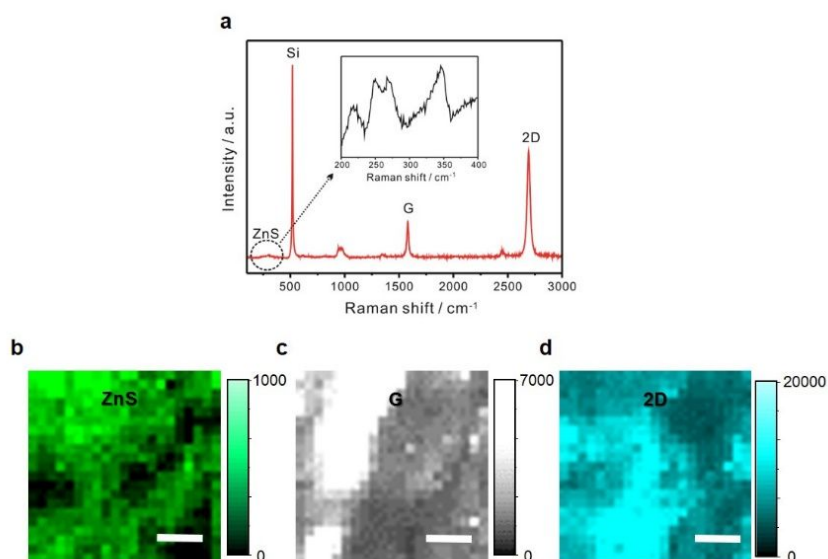


Figure 4A-5. (a) Raman spectrum of a G/ZnS sandwich-structured device and mapping profiles (scale bar = 5 μm) of (b) the ZnS, (c) the G band, and (d) the 2D band.

The Raman spectrum of S-G/ZnS in Figure 4A-5a shows two noticeable peaks of the G-band (at 1580 cm⁻¹) and the 2D-band (at 2692 cm⁻¹)³⁷ of graphene with weak peaks of ZnS (at 250 and 350 cm⁻¹).³⁸ The mapping profiles in Figure 4A-5 of b-d indicate that graphene sheets are well covered with the photo-responsive nanobelts of ZnS. The selected-area electron diffraction (SAED) pattern of Figure 4A-3c taken in a graphene-only region displays the presence of the hexagonal symmetry of graphene indeed. The SAED pattern taken in a G/ZnS hybrid region (Figure 4A-3d) shows that ZnS is single-crystalline and well-aligned along the [001] direction of the wurtzite phase. The diffraction intensity of graphene is too weak compared to that of

ZnS, so that it is rather difficult to observe the electron diffraction patterns of ZnS and graphene simultaneously in the experimental conditions.

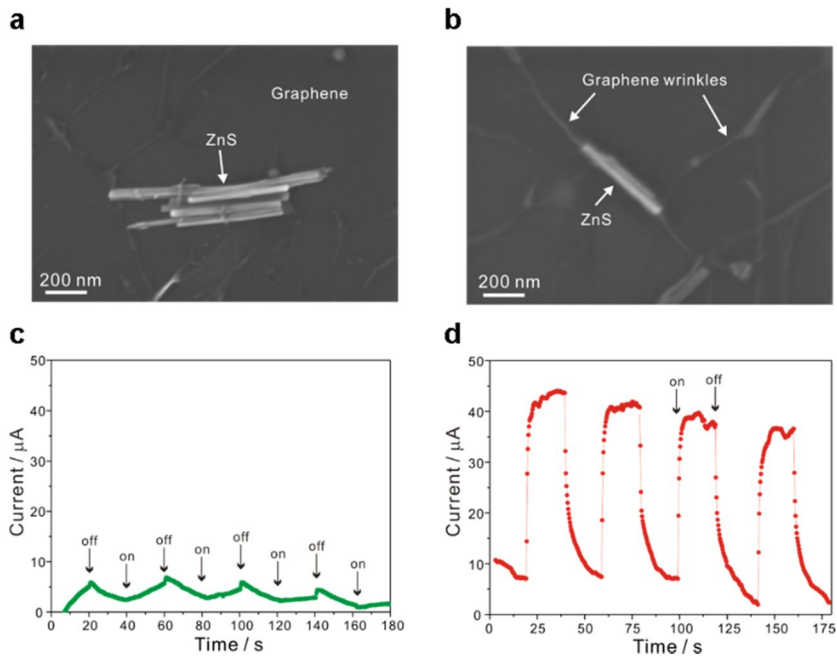


Figure 4A-6. SEM images of (a) D-G/ZnS and (b) S-G/ZnS and response behaviors of photodetectors measured in air at a bias of 1.0 V based on (c) D-G/ZnS and (d) S-G/ZnS under 300 nm light illumination.

Figures 4A-6a and 6b indicate the scanning electron microscopy (SEM) images of D-G/ZnS and S-G/ZnS, respectively; Figure 4A-6b shows the existence of large graphene wrinkles along ZnS nanobelts due to the flexible nature of graphene lying on a G/ZnS-coated substrate. Atomic force microscopy (AFM) images and their corresponding height profiles in Figure 4A-7 also display that large graphene wrinkles are present abundantly in S-G/ZnS composites. These results imply that intermolecular interactions

between graphene and ZnS has led graphene sheets to cover ZnS nanobelts tightly to form tent-like structures, as indicated in Figure 4A-7b, which expand the effective-junction region of G/ZnS hybrid structures extensively. The current-voltage characteristic curves of graphene and a G/ZnS hybrid structure (Figure 4A-8) are very similar to each other to have almost the same Dirac voltage, implying that the coating process of ZnS hardly brings any doping effect in graphene.

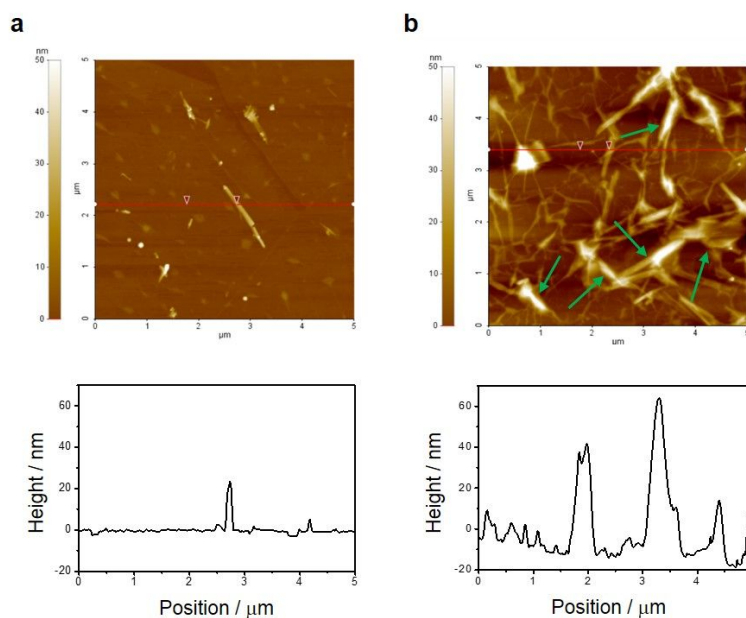


Figure 4A-7. AFM images (top) and their corresponding height profiles (bottom) of (a) D-G/ZnS and (b) composite S-G/ZnS. The height profiles were scanned along the red lines, and the green arrows indicate tent-like structures of graphene.

Figures 4A-6c and 6d present the time-dependent photoresponse behaviors of our devices measured with turning 300 nm light of 1.2 mW cm^{-2} on and off

periodically in ambient conditions. The net photocurrent can be obtained by subtracting the dark current from the light current. For a S-G/ZnS photodetector (Figure 4A-6d), a high net photocurrent of 37 μA was recorded at a low bias of 1.0 V, while a low photocurrent of 4 μA was measured for a D-G/ZnS device (Figure 4A-6c). These results imply that compared with the D-G/ZnS structure, the sandwich structure of S-G/ZnS is of great advantage to charge transfer from ZnS to graphene due to the increase of the effective-junction region between photoactive ZnS nanobelts and graphene channels.

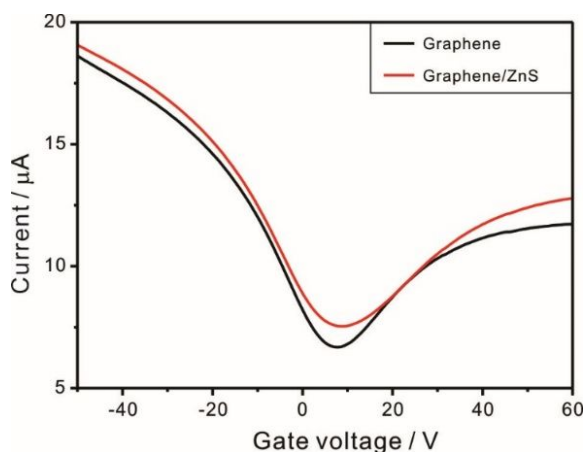


Figure 4A-8. Current-voltage characteristic curves of (black) graphene and (red) composite G/ZnS.

The detector current photoresponsivity (R_i), defined as the photocurrent generated per unit power of the incident light on the active area of the device, and the external quantum efficiency (EQE), defined as the number of electrons detected per incident photon, are crucial parameters for

photodetectors.³⁹ R_λ and EQE can be expressed as $I_\lambda/(P_\lambda S)$ and $hcR_\lambda/(e\lambda)$, respectively, where I_λ is the difference between the photocurrent and the dark current, P_λ is the light power, S is the active area of the device, h is the Planck's constant, c is the velocity of light, λ is the excitation wavelength, and e is the electronic charge. As-fabricated device has a channel length of 80 μm and a channel width of 20 μm . Therefore, the active area of the device is $1.6 \times 10^{-5} \text{ cm}^2$. According to our experimental results, R_λ and EQE for a S-G/ZnS photodetector have been calculated as $1.9 \times 10^3 \text{ AW}^{-1}$ and $8.0 \times 10^5\%$, respectively, under an applied bias voltage of 1 V with 300 nm illumination of 1.2 mWcm^{-2} . The response time is another important parameter of a photodetector. The rise and decay times (defined as times required for the peak photocurrent to increase from 10% to 90% and to drop from 90% to 10%, respectively) of a S-G/ZnS photodetector have been measured as 2.8 and 7.5 s, respectively.

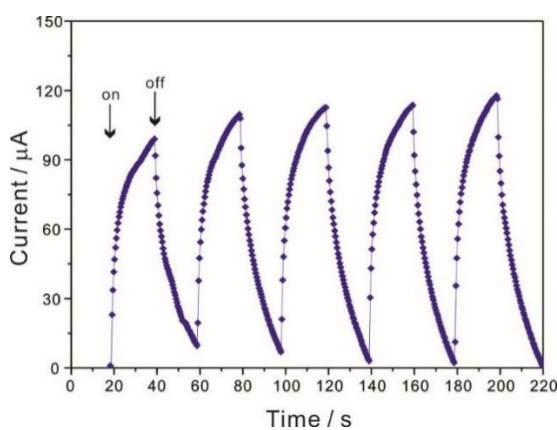


Figure 4A-9. Response behavior of a MS-G/ZnS photodetector measured in air at a bias of 1.0 V under 300 nm light illumination of 1.2 mWcm^{-2} .

The multiple stacking of graphene and ZnS (MS-G/ZnS) has facilitated the photocurrent enhancement up to 115 μA (Figure 4A-9). In order to confirm the visible blindness of a photodetector, I have also measured the response behaviors of a S-G/ZnS photodetector under visible-light illumination of 1.2 mW cm^{-2} at three different wavelengths of 400, 500, and 600 nm (Figure 4A-10); no obvious response has been observed under visible-light illumination. To confirm the repeatability and stability of our photodevice, we have also measured the photocurrent of a S-G/ZnS photodetector kept under ambient conditions for six months. Figure 4A-11 indicates that the photocurrent generation of a S-G/ZnS photodetector has remained almost invariant for six months, demonstrating the outstanding repeatability and stability of as-prepared photodevice.

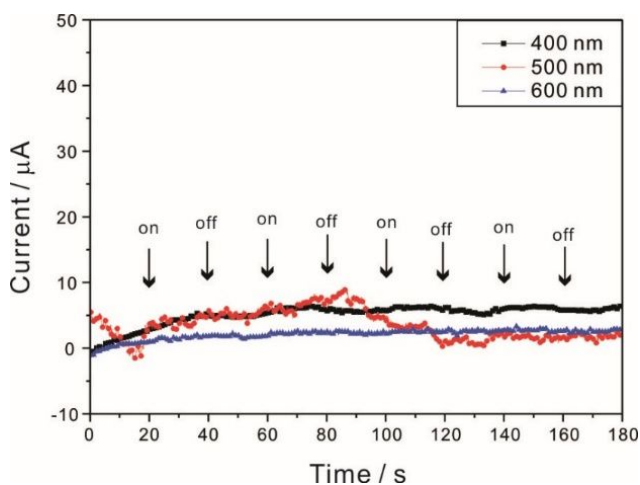


Figure 4A-10. Response behaviors of a S-G/ZnS photodetector measured in air at a bias of 1.0 V under 400 (black), 500 (red), and 600 nm (blue) light illumination of 1.2 mW cm^{-2} .

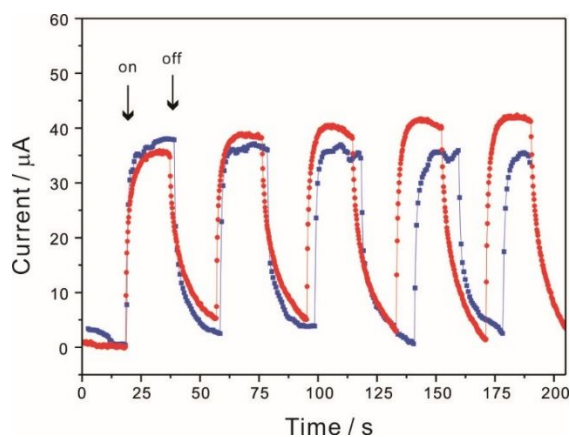


Figure 4A-11. Response behaviors of as-prepared (blue) and six months-old (red) S-G/ZnS photodetectors under 300 nm light illumination.

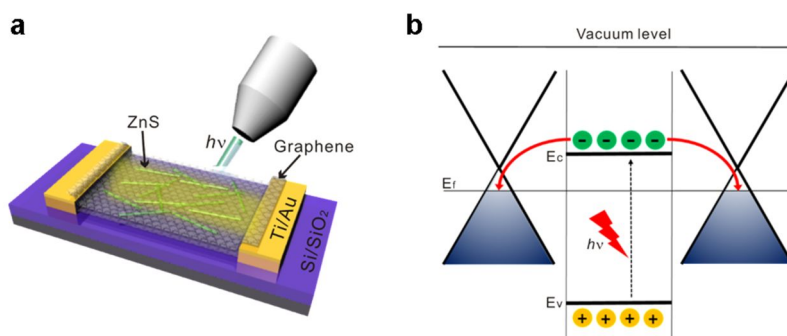


Figure 4A-12. (a) Schematic diagram of a S-G/ZnS photodetector under light illumination and (b) energy level diagram of S-G/ZnS heterojunctions showing the charge-transfer process under UV-light illumination.

Figures 4A-12a and 12b show the schematic diagram and the charge-transfer mechanism of a S-G/ZnS photodetector under light illumination, respectively. Upon absorption of light over the band-gap energy of 3.82 eV (324 nm), electron-hole pairs are generated in photoactive ZnS nanobelts.

Because the conduction-band level of ZnS is higher than the Fermi level of graphene, photoexcited electrons in the conduction band of ZnS nanobelts spontaneously undergo a charge-transfer process to graphene channels. In addition, the high charge-carrier mobility of graphene reduces the recombination process of electron-hole pairs drastically, increasing the generation of the photocurrent extremely.⁴⁰ This is the UV-selective photo-detection mechanism of S-G/ZnS nanocomposites that makes sandwich-structured photodevices show high performances at a low bias in ambient conditions for UV-light detection.

4A. 5. Conclusion

In summary, we have developed high-performance UV photodetectors based on solution-grown ZnS nanobelts sandwiched between CVD-grown graphene sheets. The formation of tent-like graphene structures in S-G/ZnS has made ZnS nanobelts completely enclosed in graphene sheets with maintaining their original shapes and properties. The increment of the effective-junction region between graphene and photoactive ZnS nanobelts by the sandwiched structure has been attributed to bring about a considerably enhanced photocurrent under UV-light illumination. A photodetector composed of S-G/ZnS exhibits a photocurrent of 37 μA under 300 nm light illumination of 1.2 mW cm^{-2} in air at a bias of 1.0 V, which is higher 9.3 times than the photocurrent of a D-G/ZnS device, with stable on-off switching and excellent spectral selectivity. A photodetector based on MS-G/ZnS shows the high photocurrent of 0.115 mA at a bias of 1.0 V, which is greater by a factor of 10^7 than the photocurrent of a graphene-free UV photodetector based on ZnS nanobelts operated at 20 V.¹⁶ The photoexcited electrons in the conduction band of ZnS spontaneously undergo a charge-transfer process to graphene channels, which is the UV-selective photo-detection mechanism of our highly efficient device. Further studies on the development of UV photodetectors with high transparency and flexibilities are under way.

4A. 6. Acknowledgements

This work was supported by the Basic Science Research Program (2014-057382) and the GRL Program (2011-0021972) through the National Research Foundation (NRF) of Korea funded by the Korea government. D.-J.J. and B.H.H. are also thankful the SRC Program (2007-0056331) and the Global Frontier Research Program (2011-0031629) of NRF, respectively.

4A. 7. References

- (1) T. Mueller, F. Xia and P. Avouris, *Nat. Photon.*, **2010**, *4*, 297.
- (2) J. Wang, M. S. Gudiksen, X. Duan, Y. Cui and C. M. Lieber, *Science*, **2001**, *293*, 1455.
- (3) X. Wang, W. Tian, M. Liao, Y. Bando and D. Golberg, *Chem. Soc. Rev.*, **2014**, *43*, 1400.
- (4) F. Guo, B. Yang, Y. Yuan, Z. Xiao, Q. Dong, Y. Bi and J. Huang, *Nature Nanotechnol.*, **2012**, *7*, 798.
- (5) Y. Liang, H. Liang, X. Xiao and S. Hark, *J. Mater. Chem.*, **2012**, *22*, 1199.
- (6) S. Yang, J. Gong and Y. Deng, *J. Mater. Chem.*, **2012**, *22*, 24522.
- (7) S. Yang, J. Gong and Y. Deng, *J. Mater. Chem.*, **2012**, *22*, 13899.
- (8) Q. Zhang, J. Jie, S. Diao, Z. Shao, Q. Zhang, L. Wang, W. Deng, W. Hu, H. Xia and X. Yuan, *ACS Nano*, **2015**, *9*, 1561.

- (9) G. Konstantatos, M. Badioli, L. Gaudreau, J. Osmond, M. Bernechea, F. P. G. de Arquer, F. Gatti and F. H. Koppens, *Nature Nanotechnol.*, **2012**, 7, 363.
- (10) S. Yang, S. Tongay, S.-S. Li, J.-B. Xia, J. Wu and J. Li, *Appl. Phys. Lett.*, **2013**, 103, 143503.
- (11) W. Tian, C. Zhang, T. Zhai, S. L. Li, X. Wang, J. Liu, X. Jie, D. Liu, M. Liao and Y. Koide, *Adv. Mater.*, **2014**, 26, 3088.
- (12) L. Hu, M. Chen, W. Shan, T. Zhan, M. Liao, X. Fang, X. Hu and L. Wu, *Adv. Mater.*, **2012**, 24, 5872.
- (13) J. Jie, W. Zhang, Y. Jiang, X. Meng, Y. Li and S. Lee, *Nano Lett.*, **2006**, 6, 1887.
- (14) C. Soci, A. Zhang, B. Xiang, S. A. Dayeh, D. Aplin, J. Park, X. Bao, Y.-H. Lo and D. Wang, *Nano Lett.*, **2007**, 7, 1003.
- (15) X. Wang, Z. Xie, H. Huang, Z. Liu, D. Chen and G. Shen, *J. Mater. Chem.*, **2012**, 22, 6845.
- (16) X. Fang, Y. Bando, M. Liao, U. K. Gautam, C. Zhi, B. Dierre, B. Liu, T. Zhai, T. Sekiguchi and Y. Koide, *Adv. Mater.*, **2009**, 21, 2034.
- (17) X. Fang, Y. Bando, M. Liao, T. Zhai, U. K. Gautam, L. Li, Y. Koide and D. Golberg, *Adv. Funct. Mater.*, **2010**, 20, 500.
- (18) Y. Yu, J. Jie, P. Jiang, L. Wang, C. Wu, Q. Peng, X. Zhang, Z. Wang, C. Xie and D. Wu, *J. Mater. Chem.*, **2011**, 21, 12632.
- (19) Y.-Y. Lin, C.-W. Chen, W.-C. Yen, W.-F. Su, C.-H. Ku and J.-J. Wu, *Appl. Phys. Lett.*, **2008**, 92, 233301.
- (20) H. Zhu, C. Shan, L. Wang, J. Zheng, J. Zhang, B. Yao and D. Shen, *J. Phys. Chem. C*, **2010**, 114, 7169.

- (21) H.-G. Li, G. Wu, M.-M. Shi, L.-G. Yang, H.-Z. Chen and M. Wang, *Appl. Phys. Lett.*, **2008**, *93*, 153309.
- (22) F. Zhang, Y. Ding, Y. Zhang, X. Zhang and Z. L. Wang, *ACS Nano*, **2012**, *6*, 9229.
- (23) L. Rigutti, M. Tchernycheva, A. De Luna Bugallo, G. Jacopin, F. Julien, L. Zagonel, K. March, O. Stephan, M. Kociak and R. Songmuang, *Nano Lett.*, **2010**, *10*, 2939.
- (24) C. Lee, X. Wei, J. W. Kysar and J. Hone, *Science*, **2008**, *321*, 385.
- (25) K. S. Kim, Y. Zhao, H. Jang, S. Y. Lee, J. M. Kim, K. S. Kim, J.-H. Ahn, P. Kim, J.-Y. Choi and B. H. Hong, *Nature*, **2009**, *457*, 706.
- (26) Y.-W. Tan, Y. Zhang, K. Bolotin, Y. Zhao, S. Adam, E. Hwang, S. D. Sarma, H. Stormer and P. Kim, *Phys. Rev. Lett.*, **2007**, *99*, 246803.
- (27) S. Morozov, K. Novoselov, M. Katsnelson, F. Schedin, D. Elias, J. Jaszczak and A. Geim, *Phys. Rev. Lett.*, **2008**, *100*, 016602.
- (28) A. C. Neto, F. Guinea, N. Peres, K. S. Novoselov and A. K. Geim, *Rev. Mod. Phys.*, **2009**, *81*, 109.
- (29) S. Adam, E. Hwang, V. Galitski and S. D. Sarma, *Proc. Natl. Acad. Sci. U.S.A.*, **2007**, *104*, 18392.
- (30) R. Nair, P. Blake, A. Grigorenko, K. Novoselov, T. Booth, T. Stauber, N. Peres and A. Geim, *Science*, **2008**, *320*, 1308.
- (31) J. S. Bunch, S. S. Verbridge, J. S. Alden, A. M. van der Zande, J. M. Parpia, H. G. Craighead and P. L. McEuen, *Nano Lett.* **2008**, *8*, 2458.
- (32) S. Chen, L. Brown, M. Levendorf, W. Cai, S.-Y. Ju, J. Edgeworth, X. Li, C. W. Magnuson, A. Velamakanni and R. D. Piner, *ACS Nano*, **2011**, *5*, 1321.

- (33) S. J. Kim, J. Ryu, S. Son, J. M. Yoo, J. B. Park, D. Won, E.-K. Lee, S.-P. Cho, S. Bae, S. Cho, and B. H. Hong, *Chem. Mater.*, **2014**, *26*, 2332.
- (34) D. I. Son, H. Y. Yang, T. W. Kim and W. I. Park, *Appl. Phys. Lett.*, **2013**, *102*, 021105.
- (35) A. Babichev, H. Zhang, P. Lavenus, F. Julien, A. Y. Egorov, Y. Lin, L. Tu and M. Tchernycheva, *Appl. Phys. Lett.*, **2013**, *103*, 201103.
- (36) Z. Zhan, L. Zheng, Y. Pan, G. Sun and L. Li, *J. Mater. Chem.*, **2012**, *22*, 2589.
- (37) A. Ferrari, J. Meyer, V. Scardaci, C. Casiraghi, M. Lazzeri, F. Mauri, S. Piscanec, D. Jiang, K. Novoselov and S. Roth, *Phys. Rev. Lett.*, **2006**, *97*, 187401.
- (38) Q. Xiong, J. Wang, O. Reese, L. Lew Yan Voon and P. Eklund, *Nano Lett.*, **2004**, *4*, 1991.
- (39) L. Li, X. Fang, T. Zhai, M. Liao, U. K. Gautam, X. Wu, Y. Koide, Y. Bando and D. Golberg, *Adv. Mater.*, **2010**, *22*, 4151.
- (40) A. K. Geim and K. S. Novoselov, *Nat. Mater.*, **2007**, *6*, 183.
- (41) Y. Kim and D.-J. Jang, *RSC Adv.*, **2013**, *3*, 16945.

Part 4B. Graphene Quantum Dots-embedded ZnS Nanobelts with Highly Efficient Photocatalytic Performances

4B. 1. Abstract

Hybrid nanostructures combining inorganic materials and graphene have shown great potential for effluent treatment as an environmentally friendly method. Herein, graphene quantum dots (GQDs)-embedded ZnS nanobelts have been synthesized via a facile hydrothermal method. Electrostatic interaction of those two materials and thermal reduction process of graphene is main driving force to fabricate well-defined heterostructures. As-prepared GQDs-ZnS (G/ZnS) nanocomposites have smaller band-gap energies by 0.29 eV compared to that of pristine ZnS. The optimized photocatalysts of G/ZnS nanocomposites (the added amount of GQDs with a GQD/ZnS mass ratio of 8×10^{-4}) have been presented a significantly enhanced photocatalytic activity for the degradation of rhodamine B with recording apparent rate constant of $4.6 \times 10^{-2} \text{ min}^{-1}$, which is 14 and 1.9 times higher than that of the commercially available ZnS powder and pristine ZnS nanobelts, respectively. The enhanced performance of G/ZnS photocatalysts in comparison with individual constituents suggest the effective separation of photoinduced electron-hole pairs and narrowing the band gaps of G/ZnS nanocomposites.

4B. 2. Introduction

The design and controlled fabrication of nanostructured materials having functional properties have been extensively studied.¹⁻⁵ With growing concern over environmental remediation and energy conversion, nanoscaled semiconductors have gained considerable interest in photocatalysis,⁶⁻¹⁰ especially in decomposition of organic water pollutants such as colored dyes into CO₂ and H₂O using solar light.¹¹⁻¹⁵ In particular, metal sulfides have attracted significant attention in photocatalysis due to their suitable band gap and catalytic function.^{14, 15} Among them, zinc sulfide (ZnS), a kind of nontoxic and abundant chalcogenide materials, with direct band gaps (3.72 eV and 3.77 eV for cubic zinc blende and hexagonal wurtzite, respectively) is a promising candidate for photocatalysts in environmental remediation,¹⁵⁻¹⁸ owing to its unique properties: the rapid generation of electron-hole pairs by photo-excitation and the highly negative reduction potential of its conduction band.¹⁹ However, the fast recombination rate of photogenerated electron-hole pairs and the narrow absorption bands of its nanostructures restrict its practical applications as photocatalysis.²⁰ To overcome these issues, ZnS photocatalysts have been modified chemically in combination with noble metals, different semiconductors, or carbonaceous materials.²¹⁻²³ It has been demonstrated that heterostructures often exhibit superior properties or new features compared with their individual constituents, due to coupling effects

that can induce significant enhancement in the generation, transportation, and prolonged lifetime of charge carriers.²⁴⁻²⁶

Graphene quantum dots (GQDs) have received much attention because they are non-toxic, inexpensive, free of heavy metals, and environmentally friendly compared with traditional quantum dots based on toxic heavy metals, which can cause serious health and environmental issues. GQDs are useful for photocatalysis applications owing to their photo-induced electron-transfer properties.²⁸⁻³⁰ Moreover, the good dispersity of GQDs in common solvents is expected to enable various solution-processable applications.³¹ Thus, the combination of ZnS and GQDs seems to be an ideal means of improving charge separation by hindering charge recombination, thus enhancing the photocatalytic efficiency.

Herein, we present the fabrication of GQDs-embedded ZnS (G/ZnS) nanobelts with varied mass ratios of GQD/ZnS from 1×10^{-4} to 2×10^{-3} via a facile hydrothermal process. ZnS nanobelts have been decorated with GQDs via a spontaneous close-contact process through electrostatic attraction to the surface of ZnS nanobelts and a subsequent tight-binding process through the thermal reduction of GQDs onto ZnS nanobelts. The band-gap energies of G/ZnS nanocomposites have been estimated to be smaller than those of pristine ZnS nanobelts. As-prepared G/ZnS photocatalysts have been found to photocatalyze the degradation of rhodamine B with remarkably enhanced efficiency in comparison with individual constituents due to the effective separation of photoinduced electron-hole pairs (Figure 4B-1).

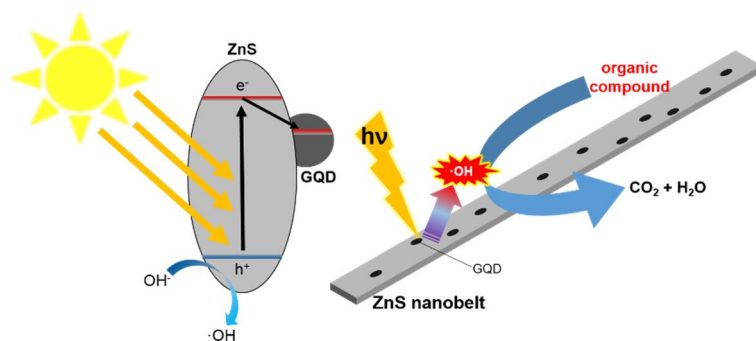


Figure 4B-1. Schematic for a plausible decomposition mechanism of an organic dye over a G/ZnS nanocomposite under light irradiation.

4B. 3. Experimental Details

Synthesis of ZnS nanobelts. Single-crystalline wurtzite ZnS nanobelts were prepared via a reported wet-chemical solution process.²⁵

Fabrication of GQDs. Carbon fibers (300 mg, purchased from Fibre Glast Development Corporation) were added into a mixture containing 60 mL of 18 M H₂SO₄(aq) and 20 mL of 16 M HNO₃(aq). The mixed solution was stirred at 800 °C for 24 h, cooled down to room temperature, and diluted with water (800 mL). The diluted solution was dialyzed in a dialysis bag, retaining molecular weight of 1000 Da for 3 days to remove the acids.

Fabrication of GQDs-ZnS nanocomposites. 20 mg of as-prepared ZnS nanobelts were dispersed in 30 mL water and ultrasonicated for 10 min. Subsequently, a calculated specific volume of 0.1 mg mL⁻¹ GQD in water was dropped slowly into the ZnS containing solution. GQD/ZnS mass ratios were varied from 1×10^{-4} to 2×10^{-3} ; if the 10^3 -multiplied weight ratio of GQDs to

ZnS nanobelts was x , the nanocomposite sample of GQDs-embedded ZnS nanobelts was designated as x G/ZnS. The mixture solution was then loaded into a Teflon-lined stainless-steel autoclave of 50 mL capacity, placed in a preheated oven at 180 °C for 6 h, and cooled to room temperature. The color of produced G/ZnS nanocomposites was found to be grayish-white. The precipitated product was repeatedly centrifuged and washed with ethanol and water, and dried in a vacuum at 60 °C for 6 h to yield the final powder product of G/ZnS nanocomposites.

Characterization. High-resolution transmission electron microscopic (HRTEM) images and energy-dispersive X-ray (EDX) elemental mappings were recorded using a JEOL JSM-2100F high-resolution microscope. X-ray diffraction (XRD) patterns were obtained with a Bruker D8 DISCOVER diffractometer using Cu K_{α} radiation (0.15418 nm), and X-ray photoelectron spectroscopy (XPS) spectra were collected with a Thermo Scientific Sigma Probe ESCA spectrometer using an X-ray source of Al K_{α} and the measured binding energies were calibrated with the C 1s peak at 284.5 eV of contaminated carbon. While Fourier transform infrared (FTIR) spectra were obtained using a Thermo Scientific Nicolet 6700 spectrometer, extinction spectra were measured using a Scinco S3100 UV-vis spectrophotometer.

Photocatalytic experiments. The evaluation of the photocatalytic performances of as-prepared samples was performed at ambient conditions with rhodamine B (RhB) as the representative dye. In a typical procedure, 5

mg of a G/ZnS catalyst was added to 40 mL of 10 μ M RhB(aq) and stirred in the dark for 30 min to ensure the adsorption-desorption equilibrium of RhB on the nanocatalyst surface. The reaction mixture was placed 30 cm away from a 300 W Schoeffel, LPS 255 HR Xe arc lamp, and its aliquots were taken at scheduled intervals during irradiation and centrifuged to separate the supernatant, whose UV/vis absorption spectrum was then recorded to monitor the concentration of remnant RhB.

4B. 4. Results and Discussion

All the diffraction peaks of both 0.8 G/ZnS nanocomposites and ZnS nanobelts in Figure 4B-2 can be indexed as the reference peaks of wurtzite ZnS (JCPDS Card No. 36-1450). The absence of the typical stacking peak at 26° indicates that the added amount of GQDs (a GQD/ZnS mass ratio of 8×10^{-4}) was too small to show any new diffraction peaks and that GQDs did not undergo stacking or conglomeration during thermal reduction. None of the XRD peaks have been attributed to impurity, suggesting that our as-prepared G/ZnS nanocomposites maintain the high structural purity of wurtzite ZnS. Figure 4B-2 also shows that the crystallinity of 0.8 G/ZnS nanocomposites is substantially higher than that of pristine ZnS nanobelts. However, the inset of Figure 4B-2 displays that the diffraction peaks of 0.8 G/ZnS nanocomposites are broader to some extent than the respective ones of pristine ZnS nanobelts, indicating that the mean crystal diameter of ZnS nanobelts has been decreased

slightly during hybridization with GQDs; the mean crystallite diameters of ZnS nanobelts and 0.8 G/ZnS nanocomposites, estimated from the line widths of the peaks at the 2θ value of 27° using the Scherrer's formula,²⁵ have been found to be 12.5 and 11.5 nm, respectively.

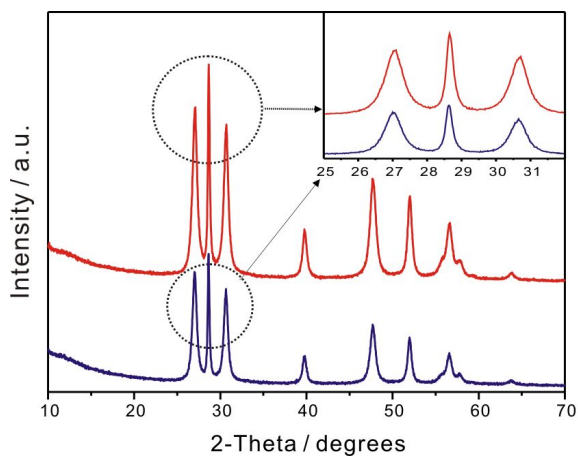


Figure 4B-2. XRD patterns of 0.8 G/ZnS nanocomposites (red) and ZnS nanobelts (blue).

The HRTEM image of Figure 4B-3A clearly shows that GQDs with an average diameter of 15 nm have been decorated successfully onto ZnS nanobelts via a hydrothermal process. Although the morphology and structure of ZnS nanobelts have been maintained during the hybridization process, the average size of GQDs has been increased due to aggregation. The HRTEM image of Figure 4B-3B reveals that interplanar spacings of 0.29, 0.31, and 0.33 nm agree very well with the respective standard separations of the (101), the (002), and the (100) planes of wurtzite ZnS. Hexagonal atomic lattice with uniform contrast, originating from monolayer graphene, can be also clearly

discerned in the enlarged HRTEM view of Figure 4B-3B. The distribution maps of the constituting elements, Zn, S, and C in the panels D, E, and F of Figure 4B-3, respectively, demonstrate that ZnS have been decorated with GQDs. Furthermore, Figure 4B-3F indicates that GQDs in 0.8 G/ZnS nanocomposites with a GQD/ZnS mass ratio of 8×10^{-4} exist discretely and uniformly on the surfaces of ZnS nanobelts.

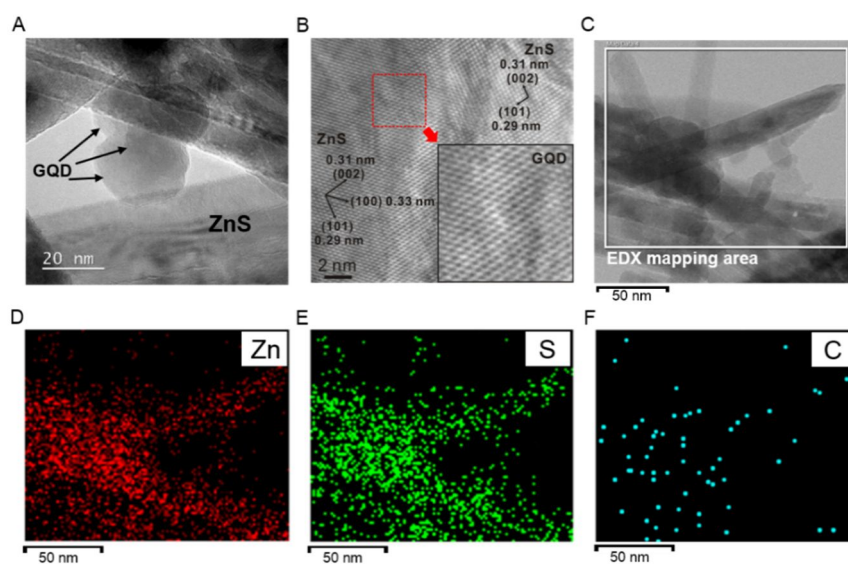


Figure 4B-3. HRTEM images (A-C) and the elemental maps of Zn, S, and C (D-F) of 0.8 G/ZnS nanocomposites.

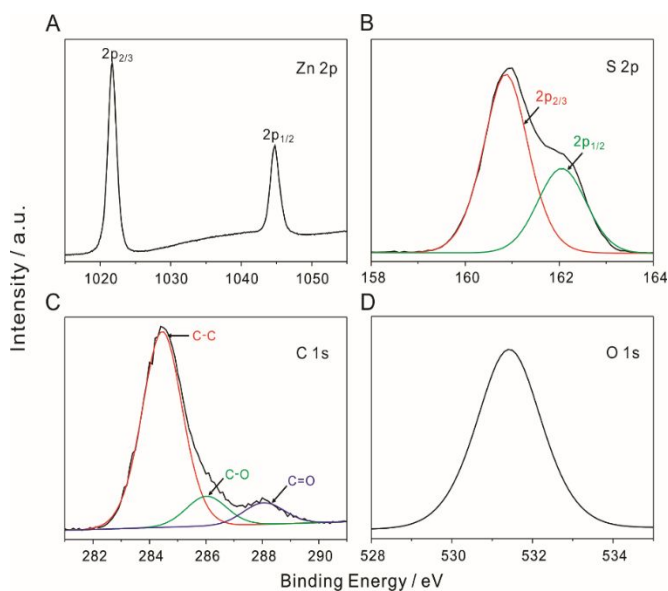


Figure 4B-4. Zn 2p (A), S 2p (B), C 1s (C), and O 1s (D) XPS spectra of 0.8 G/ZnS nanocomposites. The S 2p and C 1s spectra have been deconvoluted into two and three Gaussian curves, respectively.

To understand the binding states of the constituent elements of GQDs-embedded ZnS nanobelts, we have measured the XPS spectra of 0.8 G/ZnS nanocomposites (Figure 4B-4). The peak energies of 1021.6 and 1044.7 eV in Figure 4B-4A have been identified as the binding energies of the Zn $2p_{3/2}$ and $2p_{1/2}$ of ZnS, respectively. The XPS spectrum of Figure 4B-4B has been deconvoluted into two Gaussian bands, whose peak energies of 160.9 and 162.1 eV have been assigned to the binding energies of the S $2p_{3/2}$ and $2p_{1/2}$ of ZnS, respectively.³² The XPS spectrum of C 1s (Figure 4B-4C) has been deconvoluted into three Gaussian bands located at 284.5, 286.0, and 288.1 eV, which can be ascribed to C-C bonds, C-O bonds, and C=O bonds, respectively. However, Figure 4B-4D shows that only one XPS peak at 531.4 eV can be

attributed to O 1s, probably because of the binding energy of O 1s in the surface hydroxyl bonds of graphene³³⁻³⁶ is similar to that of O 1s in C=O bonds (see below); note that the band widths (1.95 eV) of O 1s in Figure 4B-4D is substantially broader than that (1.68 eV) of the C 1s of C-C bonds in Figure 4B-4C. Nevertheless, our XPS results also support that GQDs have been successfully incorporated with ZnS nanobelts to form G/ZnS nanocomposites.

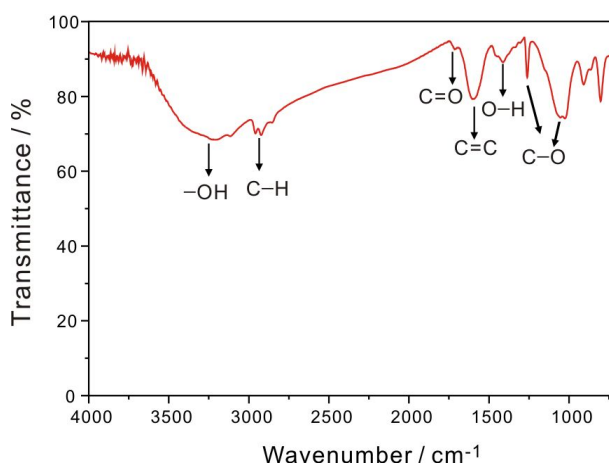


Figure 4B-5. FTIR spectrum of 0.8 G/ZnS nanocomposites.

Based on the discussion of the XPS analysis, there are different carbon functional groups on the surface of 0.8 G/ZnS nanocomposites, which can also be seen in the FTIR spectrum of Figure 4B-5. The broad absorption band located around 3250 cm⁻¹ can be assigned to the stretching vibration of O-H, while the characteristic lines at 2940 and 1718 cm⁻¹ correspond to the asymmetric stretching of -CH₂ and the stretching vibration of C=O,

respectively.^{35,37} The absorption peaks at 1601 and 1413 cm^{-1} have been attributed to the stretching vibration of C=C and the O-H deformation of C-OH, respectively, and the absorption peaks at 1261 and 1060 cm^{-1} have been assigned to the stretching vibrational modes of C-OH and C-OC, respectively.³⁸ Consequently, not only the XPS spectra of Figure 4B-4 but also the FTIR spectrum of Figure 4B-5 support that GQDs have been decorated to ZnS nanobelts with maintaining the inherent characteristics of graphene oxide and graphene.

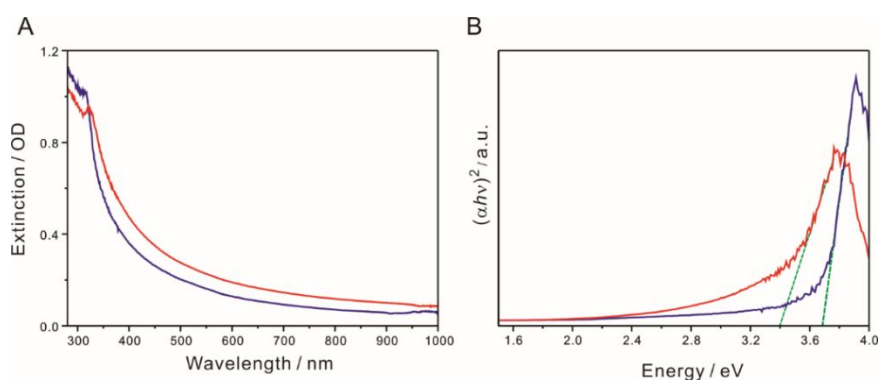


Figure 4B-6. Extinction spectra (A) and Kubelka-Munk plots (B) of 0.8 G/ZnS nanocomposites (red) and 0.0 G/ZnS nanobelts (blue) suspended in ethanol. The green solid lines in panel B show the best linear fits to estimate the band-gap energy.

The extinction spectra of Figure 4B-6A show that both samples of 0.8 G/ZnS nanocomposites and 0.0 G/ZnS nanobelts have the representative band-gap absorption of ZnS nanobelts in the ultraviolet region. The enhanced

absorption of 0.8 G/ZnS nanocomposites in the entire visible region can be attributed to the presence of graphene. However, in comparison with the extinction spectrum of 0.0 G/ZnS nanobelts, that of G/ZnS nanocomposites shows the obvious red shift of the absorption edge by 14 nm due to the chemical interactions of ZnS with graphene. It is well known that ZnS is a direct semiconductor, whose band gap can be estimated by extrapolating the linear portion of the modified Kubelka-Munk function²⁵ versus the energy of light (Figure 4B-6B). The derived band gaps of 0.0 G/ZnS and 0.8 G/ZnS nanocomposites have been estimated as 3.69 and 3.40 eV, respectively, indicating that coupling with graphene narrows the band gap of semiconductor ZnS in G/ZnS nanocomposites. We suggest that band-gap narrowing as well as increased visible-light absorption due to graphene decoration enhances the photocatalytic performances of G/ZnS nanocomposites (see below).

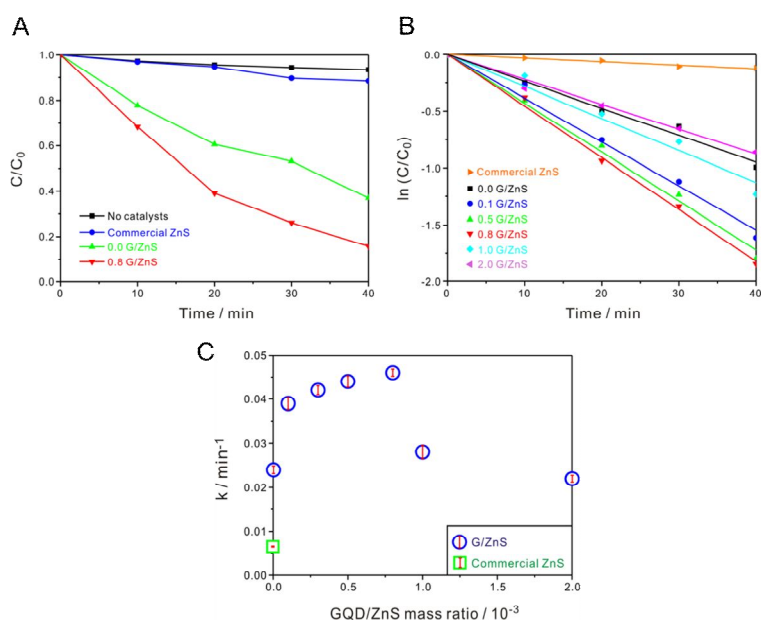


Figure 4B-7. Concentration changes (A), first-order kinetic profiles (B), and decay rate constants (C) of RhB via indicated photocatalysts.

The photocatalytic degradation of RhB under light irradiation at ambient conditions has been monitored to evaluate the photocatalytic activities of G/ZnS nanocatalysts. Figure 4B-7A indicates that while the concentration of RhB was hardly reduced in the absence of the photocatalyst, and that was decreased most rapidly under the photocatalysis of 0.8 G/ZnS nanocomposites. The $\ln(C/C_0)$ -vs- t kinetic plots of the photocatalytic degradation of RhB under light irradiation in the presence of G/ZnS nanocomposites were also investigated in Figure 4B-7B; the photodegradation profiles of RhB via G/ZnS nanocomposites follow pseudo first-order kinetics. Figure 4B-7C shows that the photocatalytic activity of G/ZnS nanocomposites in the photodegradation reaction of RhB was increased with the increase of the GQD/ZnS mass ratio until the ratio became 8×10^{-4} . This indicates indeed that hybridization with graphene enhances the photocatalytic activity of ZnS nanoparticles immensely. However, the photocatalytic activity decreases with the concentration increase of GQDs above the GQD/ZnS mass ratio of 8×10^{-4} . We consider that excessive GQDs can act as charge-recombination centers instead of electron pathways. Table 4B-1 reveals that the observed photocatalytic rate constant of 0.8

G/ZnS nanocomposites (0.046 min^{-1}) is 14 times higher than that of the commercially available ZnS powder and 1.9 times higher than that of 0.0 G/ZnS. The extensively enhanced photocatalytic performances of G/ZnS nanocomposites can be suggested as follows: photo-generated electrons from ZnS nanobelts can transport along GQDs and then react with absorbed O_2 molecules to form $\cdot\text{OH}$ radicals for the further photocatalytic degradation of RhB (Figure 4B-1). During this process, GQDs serve as electron collectors and transporters to block electron-hole recombination efficiently, generating long-lived holes on the surfaces of ZnS nanobelts. Longer-lived holes then account for the largely enhanced photocatalytic activity of G/ZnS nanocomposites. The thermal reduction of GQDs onto the ZnS nanobelts directly without having any linker molecules can provide new absorption bands to our G/ZnS nanocomposites. Newly generated electrons in the Fermi level of graphene with leaving holes to the valence-band level of ZnS introduce visible-light absorption and induce band-gap narrowing to G/ZnS nanocomposites. Because the Fermi level of ZnS is lower than that of graphene and GQDs are attached to ZnS nanobelts, the energy band of G/ZnS nanocomposites will curve up to form a metal-semiconductor Schottky junction under equilibrium. The excited electrons of graphene are not allowed to transfer to the conduction band

of ZnS due to the energy barrier between graphene and ZnS. This energy barrier also facilitates charge-separation processes and effectively reduces recombination chances of newly generated electrons and holes, significantly increasing the lifetime of charges in G/ZnS nanocomposites. Long-lived charges are then suggested to enhance the photocatalytic performances of G/ZnS nanocomposites efficiently.

Table 4B-1. Catalytic degradation rate constant of 10^{-5} M RhB(aq) via nanocatalysts under irradiation of a 300 W Xe lamp.

Nanocatalyst	GQD/ZnS mass ratio (10^{-3})	k (min^{-1})
No catalysts	–	0.002
Commercial ZnS	0.0	0.003
0.0 G/ZnS	0.0	0.024
0.1 G/ZnS	0.1	0.039
0.2 G/ZnS	0.2	0.042
0.5 G/ZnS	0.5	0.043
0.8 G/ZnS	0.8	0.046
1.0 G/ZnS	1.0	0.028
2.0 G/ZnS	2.0	0.022

4B. 5. Conclusion

Highly efficient photocatalysts of GQDs-embedded ZnS nanobelts have been developed via a facile hydrothermal process. The decoration of ZnS nanobelts has been carried out via two synthetic steps: the spontaneous attachment of GQDs on the surface of ZnS nanobelts through electrostatic attraction, followed by partial thermal reduction of GQDs constructing well-defined heterostructures. The additional visible light response was generated and the photo-induced charges might be effectively separated due to GQDs-embedding, enhancing the photocatalytic efficiency. The optimized 0.8 G/ZnS showed highest photocatalytic activity for the degradation of rhodamine B with recording apparent rate constant of $4.6 \times 10^{-2} \text{ min}^{-1}$, which is 14 and 1.9 times higher than that of commercially available ZnS powder and 0.0 G/ZnS nanobelts, respectively.

4B. 6. Acknowledgements

This work was supported by a research grant through the National Research Foundation (NRF) of Korea funded by the Korean government (2014-057382). D.J.J. is also thankful to the SRC program of NRF (2007-0056331).

4B. 7. References

- (1) D. Choi, J.-Y. Pyo, Y. Kim and D.-J. Jang, *J. Mater. Chem. C*, **2015**, 3, 3286.
- (2) H. Lee, J.-A. Kwak and D.-J. Jang, *J. Phys. Chem. C*, **2014**, 118, 22792
- (3) M. Son, S. Jeong and D.-J. Jang, *J. Phys. Chem. C*, **2014**, 118, 5961
- (4) Y. Kim and D.-J. Jang, *Chem. Commun.*, **2013**, 49, 8940
- (5) Y. Kim, S. J. Kim, S.-P. Cho, B. H. Hong and D.-J. Jang, *Sci. Rep.*, **2015**, 5, 12345
- (6) X. Xu, C. Randorn, P. Efstathiou and J. T. Irvine, *Nat. Mater.*, **2012**, 11, 595.
- (7) A. Kudo and Y. Miseki, *Chem. Soc. Rev.*, **2009**, 38, 253.
- (8) H.-B. Kim, H. Kim, W. I. Lee and D.-J. Jang, *J. Mater. Chem. A*, **2015**, 3, 9714.
- (9) J.-Y. Kim, D. Lee, H. J. Kim, I. Lim, W. I. Lee and D.-J. Jang, *J. Mater. Chem. A*, **2013**, 1, 5982.
- (10) S. J. Moniz, S. A. Shevlin, D. J. Martin, Z.-X. Guo and J. Tang, *Energy Environ. Sci.*, **2015**, 8, 731.
- (11) R. Asahi, T. Morikawa, T. Ohwaki, K. Aoki and Y. Taga, *Science*, **2001**, 293, 269.
- (12) L. Zhang, L. Du, X. Yu, S. Tan, X. Cai, P. Yang, Y. Gu and W. Mai, *ACS Appl. Mater. Interfaces*, **2014**, 6, 3623.

- (13) A. Gupta, K. Mondal, A. Sharma and S. Bhattacharya, *RSC Adv.*, **2015**, *5*, 45897.
- (14) Y. Kim, H.-B. Kim and D.-J. Jang, *J. Mater. Chem. A*, **2014**, *2*, 5791.
- (15) D. Chen, F. Huang, G. Ren, D. Li, M. Zheng, Y. Wang and Z. Lin, *Nanoscale*, **2010**, *2*, 2062.
- (16) M. Muruganandham and Y. Kusumoto, *J. Phys. Chem. C*, **2009**, *113*, 16144.
- (17) M. Sharma, T. Jain, S. Singh and O. Pandey, *Solar Energy*, **2012**, *86*, 626.
- (18) S. Xiong, B. Xi, C. Wang, D. Xu, X. Feng, Z. Zhu and Y. Qian, *Adv. Funct. Mater.*, **2007**, *17*, 2728.
- (19) H. Yin, Y. Wada, T. Kitamura and S. Yanagida, *Environ. Sci. Technol.*, **2001**, *35*, 227.
- (20) D. F. Moore, Y. Ding and Z. L. Wang, *J. Am. Chem. Soc.*, **2004**, *126*, 14372.
- (21) J. Zhnag, Y. Wang, J. Zhang, Z. Lin, F. Huang, and J. Yu, *ACS Appl. Mater. Interfaces*, **2013**, *5*, 1031
- (22) E. Hong, D. Kim, and J. H. Kim, *J. Ind. Eng. Chem.*, **2014**, *20*, 3869
- (23) Y. Zhang, N. Zhang, Z.-R. Tang, and Y.-J. Xu, *ACS Nano*, **2012**, *11*, 9777
- (24) Y. Tang, X. Liu, C. Ma, M. Zhou, P. Hou, L. Yu, J. Pan, W. Shi, and Y. Yan, *New J. Chem.*, **2015**, *39*, 5150
- (25) Y. Kim and D.-J. Jang, *RSC Adv.*, **2013**, *3*, 16945.

- (26) J.-Y. Kim, M. R. Kim, S.-Y. Park and D.-J. Jang, *CrystEngComm*, **2010**, *12*, 1803
- (27) Y. Zheng, L. Zheng, Y. Zhan, X. Lin, Q. Zheng, and K. Wei, *Inorg. Chem.*, **2007**, *46*, 6980.
- (28) J. Wang, Y. Li, J. Ge, B.-P. Zhang, and W. Wan, *Phys. Chem. Chem. Phys.*, **2015**, *17*, 18645.
- (29) D. Qu, M. Zheng, P. Du, Y. Zhou, L. Zhang, D. Li, H. Tan, Z. Zhao, Z. Xie, and Z. Sun, *Nanoscale*, **2013**, *5*, 12272.
- (30) S. Zhou, M. Shao, and S.-T. Lee, *ACS Nano*, **2012**, *6*, 1059.
- (31) X. Wang, W. Tian, M. Liao, Y. Bando and D. Golberg, *Chem. Soc. Rev.*, **2014**, *43*, 1400.
- (32) G. Wang, B. Huang, Z. Li, Z. Lou, Z. Wang, Y. Dai and M.-H. Whangbo, *Sci. Rep.*, **2015**, *5*, 8544
- (33) A. C. Neto, F. Guinea, N. Peres, K. S. Novoselov and A. K. Geim, *Rev. Mod. Phys.*, **2009**, *81*, 109.
- (34) S. Adam, E. Hwang, V. Galitski and S. D. Sarma, *Proc. Natl. Acad. Sci. U.S.A.*, **2007**, *104*, 18392.
- (35) R. Nair, P. Blake, A. Grigorenko, K. Novoselov, T. Booth, T. Stauber, N. Peres and A. Geim, *Science*, **2008**, *320*, 1308.
- (36) L. Wang, Y. Wang, T. Xu, H. Liao, C. Yao, Y. Liu, Z. Li, Z. Chen, D. Pan, L. Sun and M. Wu, *Nat. Commun.*, **2014**, *5*, 5357
- (37) J. S. Bunch, S. S. Verbridge, J. S. Alden, A. M. van der Zande, J. M. Parpia, H. G. Craighead and P. L. McEuen, *Nano Lett.* **2008**, *8*, 2458.

(38) Sudesh, N. Kumar, S. Das, C. Bernhard, and G. D. Varma, *Supercond. Sci. Technol.*, **2013**, 26, 095008

Appendices

A. 1. List of Publications

1. **Yeonho Kim**, Jong-Yeob Kim, and Du-Jeon Jang "One-pot and template-free fabrication of ZnS (ethylenediamine)_{0.5} hybrid nanobelts" *J. Phys. Chem. C* **2012**, *116*, 10296.
2. Sun-Young Park, **Yeonho Kim**, Jin Yong Lee, and Du-Jeon Jang "Ground-state proton transport along a blended-alcohol chain: accelerated by accumulated proton-donating ability" *J. Phys. Chem. B* **2012**, *116*, 10915.
3. Yu-Yang Zhang, Jong-Yeob Kim, **Yeonho Kim**, and Du-Jeon Jang "Controlled optical properties of water-soluble CdTe/CdS/ZnS quantum dots" *J. Nanopart. Res.* **2012**, *14*, 1117.
4. **Yeonho Kim** and Du-Jeon Jang "Facile one-step hydrothermal fabrication of single-crystalline ZnS nanobelts with narrow band-edge luminescence" *RSC Adv.* **2013**, *3*, 16945.
5. **Yeonho Kim** and Du-Jeon Jang "Facile-growth mechanism of wurtzite ZnS nanostructures showing intense ultraviolet luminescence" *CrystEngComm* **2014**, *16*, 6989.
6. Dayeon Choi, Ji-Young Pyo, **Yeonho Kim**, and Du-Jeon Jang "Facile synthesis of composition-gradient Cd_{1-x}Zn_xS quantum dots by cation exchange for controlled optical properties" *J. Mater. Chem. C* **2015**, *3*, 3286.
7. Yeonho Kim, Sang Jin Kim, Sung-Pyo Cho, Byung Hee Hong, and Du-Jeon Jang "High-performance ultraviolet photodetectors based on solution-grown ZnS nanobelts sandwiched between graphene layers" *Sci. Rep.* **2015**, *5*, 12345.

A. 2. List of Presentations

A. 2. 1. International Presentations

1. Yeonho Kim, Jong-Yeob Kim, and Du-Jeon Jang “Synthesis, Characterization, and Formation Mechanism of ZnS-Based Inorganic-Organic Hybrid Nanobelts” Gordon Research Conference on Colloidal Macromolecular & Polyelectrolyte Solutions, Ventura, CA, USA (2012).

2. **Yeonho Kim** and Du-Jeon Jang “Facile Shape Control of ZnS(ethylenediamine)_{0.5} Hybrid Nanostructures” Material Research Society Spring Meeting & Exhibit, San Francisco, CA, USA (2013).

3. Jong-Yeob Kim, **Yeonho Kim**, Daeki Lee, Wan In Lee, and Du-Jeon Jang “Annealing-free fabrication of anatase TiO₂ nanopopcorns on Ti foil for photovoltaic and photocatalytic applications” 44th World Chemistry Congress, Istanbul, Turkey (2013).

A. 2. 2. Domestic Presentations

1. Yeonho Kim, Jong-Yeob Kim, and Du-Jeon Jang “Facile Hydrothermal Growth Control of Highly Luminescent ZnS Nanobelts” The 107th National Meeting of the Korean Chemical Society, Jeju, Korea (2011).

2. **Yeonho Kim**, Jong-Yeob Kim, and Du-Jeon Jang “Fabrication of ZnS·(EN)_{0.5} Nanobelts via a Solvothermal Route and Their Characterization” The 108th National Meeting of the Korean Chemical Society, Daejeon, Korea (2011).

3. **Ji-Young Pyo**, **Yeonho Kim**, and Du-Jeon Jang “Synthesis and Optical Properties of CdS@ZnS Core-Shell Quantum Dots Stabilized with 3-Mercaptopropionic Acid” The 108th National Meeting of the Korean Chemical Society, Daejeon, Korea (2011).

4. **Yeonho Kim** and Du-Jeon Jang “Facile Synthesis of Single-Crystalline ZnS·(en)_{0.5} Hybrid Nanobelts” The 109th National Meeting of the Korean Chemical Society, Goyang, Korea (2012).

5. **Ji-Young Pyo**, **Yeonho Kim**, and Du-Jeon Jang “Synthesis and Characterization of Mn-doped CdSe@ZnSe Semiconductor Nanocrystals” The 109th National Meeting of the Korean Chemical Society, Goyang, Korea (2012).

6. **Yeonho Kim**, Jong-Yeob Kim, and Du-Jeon Jang “Single-Step Hydrothermal Synthesis of ZnS Nanorods Exhibiting Enhanced Band-Edge Emission” The 110th National Meeting of the Korean Chemical Society, Busan, Korea (2012).

7. **Jong-Yeob Kim**, **Yeonho Kim**, and Du-Jeon Jang “Fabrication and Characterization of Water-Soluble CdTe/CdS/ZnS Core-Shell-Shell Quantum

Dots” The 110th National Meeting of the Korean Chemical Society, Busan, Korea (2012).

8. Ji-Young Pyo, **Yeonho Kim**, and Du-Jeon Jang “Aqueous Synthesis of CdS@Cd_xZn_{1-x}S Core@Shell Quantum Dots to Have Controlled Optical Properties” The 110th National Meeting of the Korean Chemical Society, Busan, Korea (2012).

9. **Yeonho Kim** and Du-Jeon Jang “Hydrothermal Synthesis of Wurtzite ZnS Nanoblades in Ternary Mixed Solvent Systems” The 111st National Meeting of the Korean Chemical Society, Goyang, Korea (2012).

10. **Yeonho Kim** and Du-Jeon Jang “Morphology-Controlled Fabrication of ZnS Nanostructures with Enhanced UV Emission” The 44th Winter Annual Conference of the Korean Vacuum Society, Pyeongchang, Korea (2013).

11. **Yeonho Kim** and Du-Jeon Jang “Facile-Growth Mechanism of Wurtzite ZnS Nanobelts” The 113rd National Meeting of the Korean Chemical Society, Goyang, Korea (2014).

12. Dayeon Choi, **Yeonho Kim**, and Du-Jeon Jang “Synthesis of Composition-Gradient Cd_{1-x}Zn_xS Quantum Dots by Facile Cation Exchange to Controlled Their Optical Properties” The 113rd National Meeting of the Korean Chemical Society, Goyang, Korea (2014).

13. SooHo Ham, **Yeonho Kim**, and Du-Jeon Jang “Photo-Deposition of Noble Metals (Au, Pt) on Wurtzite ZnS Nanobelts” The 115th National Meeting of the Korean Chemical Society, Goyang, Korea (**2015**).

14. Dayeon Choi, **Yeonho Kim**, and Du-Jeon Jang “Cation Exchange of CdS Quantum Dots to Control Optical Properties” The 115th National Meeting of the Korean Chemical Society, Goyang, Korea (**2015**).

Abstract (Korean)

상온에서 강한 자외선 발광을 보이며 좁은 반치폭을 가진 단결정 ZnS 나노벨트를 수열 방법으로 용액상에서 합성하였다. 이를 위해 3 중 용매 시스템을 구성하였으며, 각각의 용매는 한번의 반응으로 단결정 ZnS 나노벨트를 합성됨에 있어서 중요한 역할을 하였다. 만들어진 나노벨트는 화학적 조성이 균일하며 결정의 결함을 나타내지 않는 물질임을 다양한 분석을 통해 밝혀냈다. 이러한 특성들은 나노벨트가 상온에서 강하고 좁은 반치폭을 지닌 자외선 발광을 나타내는데 기인을 하였다. 또한 만들어진 일차원 ZnS 나노벨트를 그래핀과의 혼합구조로 제조하였고 이를 자외선 감지 센서 및 고효율 광촉매제로 응용 하였다.

1 장에서는 2-6 족으로 구성된 화합물 반도체가 나노크기로 제한되었을 경우 나타낼 수 있는 특성에 대한 간략한 소개로 구성 되어있다. 특히 나노크기에서 물질이 나타내는 화학적, 물리적 특성을 마이크로 또는 벌크 크기일 때와 비교하여 분석하고 기술하였다. 1 장의 끝부분은 일차원 ZnS 나노물질을 합성하는 방법과 이 물질의 광학적 특성 및 결정학적 특성에 대해 기술 되어 있다.

2 장에서는 ethylenediamine(en)을 구조유도 물질로 사용하여 만든 ZnS-en 유무기 하이브리드 나노벨트에 대한 광학적 특성과 구조적 성질에 대해 기술 되어 있다. 일차원 나노구조체를 용액상에서 제조할 때 이용되어 왔던 hard template 를 사용하지 않았으며, 일차원 구조로 물질의 성장을 용이케 하는 en 을

사용하고 황 이온을 공급하기 위해 이용한 hydrazine 과 구조유도 용매인 en 간의 혼합 비율을 조절하여 유무기 하이브리드 나노벨트의 중량비를 조절하였다. 용매간의 혼합비율은 만들어지는 물질의 결정성 및 광학적 성질에도 영향을 미쳤다. 나노벨트의 광학적 특성을 파악하기 위해 레이저의 빛 여기에서 나타내는 물질의 발광을 측정하였으며, 이를 Gasussian fitting 을 통해 세부적인 분석을 하였다. 하이브리드 나노벨트는 세 영역에서 발광 현상을 보였으며 이를 밴드갭 발광, 트랩에 기인된 발광, 이온 결합에 의한 발광으로 분석하고 정의하였다. 또한 들뜬 상태에서의 발광 평균 수명분석을 통해 여기된 전자의 이동 경로의 추적 및 발광체로 최적화된 ZnS-en 하이브리드 나노벨트의 제조 조건을 제시하였다.

3 장에서는 상온에서 강한 자외선 발광을 보이는 ZnS 나노벨트를 오토클레이브를 이용하여 한 번의 반응으로 제조하는 방법을 기술하였다. 이전까지는 두 단계 반응을 통해 수용액에서 일차원 ZnS 를 제조하였는데, 본 합성법으로 한 번의 반응으로 일차원 ZnS 를 제조할 수 있었다. 만들어진 물질의 밴드갭 발광 특성 분석을 위해 Lorentzian fitting 을 적용하였으며, 이를 알려진 이론값과 비교 및 분석하였다. 이를 통해 valence band 의 갈라짐에 의한 2 개의 밴드갭 발광을 확인할 수 있었으며, 이론값과 실험적 오차범위 내에서 일치함을 확인하였다. 또한 단결정 ZnS 나노벨트가 형성되는 메커니즘에 대한 분자수준의 규명과 자외선에서 강한 밴드갭을 나타내는 이유를 전자현미경, 엑스선 회절, 열분해와 다양한 분광학적 분석을 통해 제시하였다.

4 장에서는 그래핀과 단결정 ZnS 나노벨트의 혼합구조를 이용한 응용이 기술 되어 있다. 용액 공정을 통해 성장한 단결정 ZnS 나노벨트와 화학증착법으로 합성된 그래핀의 하이브리드 구조를 이용하여 고성능 자외선 감지 센서로의 응용을 하였다. 샌드위치 구조를 이용하여 광감응성 물질인 ZnS 와 전자 수송 채널로 작동하는 그래핀과의 접촉 면적의 최대화를 유도하였고, 효율적인 전하분리를 일으켜 센서의 광전류 생성을 극대화 하였다. 빛에 의해서 여기된 전자는 ZnS 의 conduction band 에서 전하이동 과정을 거쳐 전자수송 채널인 그래핀으로 이동을 하는데 이것이 본 연구에서 만들어진 광센서가 자외선 영역의 빛만 감지하는 원리이며 작동하는 메커니즘이다. 또한 분리된 전자와 정공은 그래핀의 빠른 전하수송 능력에 의해 전극으로 빠져나가기 때문에 낮은 구동전압에서 mA 수준의 광전류를 나타내는 광센서 소자의 작동을 가능하게 하였다.

또한 양자점 그래핀과 일차원 ZnS 의 혼합구조물을 이용한 고효율 광촉매에 대한 연구도 기술 되어 있다. 반대되는 표면 전하를 가진 두 물질의 정전기적 인력을 이용하여 물질을 가까이 접근시키고, 열을 이용하여 양자점 그래핀을 ZnS 표면에 환원된 양자점 그래핀 형태로 도핑 시킨다. 이는 물질간의 계면전하이동을 극대화 시키며 반도체 물질인 ZnS 의 밴드구조에 영향을 주기에 좁아진 밴드갭 특성과 가시광 영역의 부분적으로 증대된 흡광 특성을 보이게 된다. 만들어진 그래핀-ZnS 하이브리드 혼합구조는 일차원으로 성장된 ZnS 의 특성을 유지하기에 높은 광촉매 효율을 보이게 된다. 또한 두 물질간의 극대화된 계면전하이동에 의한

광응답범위의 확장 및 전하분리현상에 의해 광촉매 성능이 향상되었으며, 양자점 그래핀의 도핑 양을 조절하여 최적화된 양자점 그래핀-ZnS 혼합구조물의 합성조건을 제시하였다.

주요어: 반도체, 트랜지스터, 광검출기, 광촉매, 하이브리드

학번: 2010-20267